

PRODUCTIVITY INCREASE AND PROCESS INNOVATION FOR SCALING-  
UP ZEOLITIC IMIDAZOLATE FRAMEWORKS (ZIFS) POLYCRYSTALLINE  
MEMBRANES

A Dissertation

by

JINGZE SUN

Submitted to the Office of Graduate and Professional Studies of  
Texas A&M University  
in partial fulfillment of the requirements for the degree of

DOCTOR OF PHILOSOPHY

Chair of Committee,	Hae-Kwon Jeong
Co-Chair of Committee,	Benjamin Wilhite
Committee Members,	Hongcai Joe Zhou
	Mustafa Akbulut

Head of Department,	Arul Jayaraman
---------------------	----------------

December 2019

Major Subject: Chemical Engineering

Copyright 2019 Jingze Sun

## ABSTRACT

Propylene/propane separation by cryogenic distillation is energy-intensive and therefore non-thermal driven alternatives like membrane separations or adsorption processes can provide a significant cut in energy consumption. However, due to their similarities in sizes and molecular properties, separating propylene (4.0 Å) from propane (4.2 Å) still remains challenging. Traditional membrane materials, e.g. polymers, cannot provide commercially attractive selectivity and permeance at the same time and the need for novel membrane materials are imminent. Metal organic frameworks (MOFs), comprising of metal nodes and organic linkers connected by coordination bounds, have been regarded as one of the promising candidates, mainly because of their versatility for structural design. Among MOFs, Zeolitic imidazolate frameworks, made primarily by Zn, Co, Cd metal nodes and imidazolate-derived linkers, showed reliable chemical, thermal and mechanical stabilities, offering ZIF-8 (Zn and 2-methylimidazolate), ZIF-67 (Co and 2-methylimidazolate), ZIF-90 (Zn and benzimidazolate) and several other materials that possess effective aperture sizes lying between the size of propylene and propane.

Further applications of ZIF membranes are mainly hindered by their expensive manufacturing costs. Some of the possible solutions are reducing the required membrane areas by 1) reducing the membrane thickness 2) slightly enlarging the effective aperture sizes 3) use better supports to provide high packing

densities. This thesis tends to provide a comprehensive exploration of all these aspects to further the scaling-up of this green alternative route for paraffin olefin separations.

## ACKNOWLEDGMENTS

I would greatly thank Dr. Hae-Kwon Jeong's help and guidance during my 4 years here at TAMU as well as the rest of my committee members. Thanks to my labmates for being so nice all the time. I really appreciate the high-standard education provided by the Engineering School of TAMU. I would also like to give thanks for all the funding agencies, who enable these great scientific research projects for these next-generation separation techniques.

Above all, I deeply appreciate the help from my parents, who fully supported my adventure here across half of the globe. And especially my beloved little one, who encouraged me, inspired me and accompanied me through countless sleepless nights. We shared this great journey together to inner maturity, which built a life-time bond between us. Best wishes to everyone mentioned above as well as to my great motherland.

## CONTRIBUTORS AND FUNDING SOURCES

This work was supported by a dissertation committee consisting of Professor Hae-Kwon Jeong, Professor Benjamin Wilhite and Professor Mustafa Akbulut of the Department of Chemical Engineering Department and Professor Hongcai Joe Zhou of the Department of Chemistry Department.

I acknowledge the financial support from the National Science Foundation (CMMI-1561897 and CBET-150530) and in part from the Qatar National Research Fund (NPRP 7-042-2-021 and NPRP 8-001-2-001). The FE-SEM acquisition was supported by the National Science Foundation under Grant DBI-0116835. I also would like to thank the VP for Research Office, and the Texas A&M Engineering Experiment Station.

## TABLE OF CONTENTS

	Page
ABSTRACT .....	ii
ACKNOWLEDGMENTS.....	iv
CONTRIBUTORS AND FUNDING SOURCES.....	v
TABLE OF CONTENTS .....	vi
LIST OF FIGURES.....	ix
LIST OF TABLES .....	xiv
1. INTRODUCTION .....	1
2. BACKGROUND AND LITERATURE REVIEW.....	7
2.1. Light olefins.....	7
2.1.1. Production and purification process of light olefins .....	7
2.1.2. General introduction to polyolefin production.....	9
2.2. Light olefin/paraffin separations .....	10
2.2.1. Drawbacks of traditional cryogenic distillations .....	10
2.2.2. Membrane methods and different membrane materials.....	10
2.3. Metal organic framework (MOFs) and Zeolitic Imidazolate framework.....	12
2.4. The chemistry nature of ZIF-8 and its common recipes.....	16
2.4.1. Gas transportation in ZIF-8.....	16
2.4.2. ZIF-8 and related membranes on ceramic planar supports .....	17
2.4.3. In-situ methods.....	19
2.4.4. Seeding and secondary growth method .....	20
2.5. Improvement of ZIF membranes for propylene propane separation.....	21
3. FACILE SYNTHESIS OF CD-SUBSTITUTED ZEOLITIC-IMIDAZOLATE FRAMEWORK CD-ZIF-8 AND MIXED-METAL CDZN-ZIF-8 .....	24
3.1 Introduction .....	24
3.2 Experimental.....	26
3.2.1 Chemicals.....	26
3.2.2 Synthesis of Cd-ZIF-8.....	27
3.2.3 Synthesis of Zn-ZIF-8 and Co-ZIF-8.....	27
3.2.4 Synthesis of mixed-metal Cd-Zn-ZIF-8.....	28

3.2.5 Single crystal synthesis of Zn-ZIF-8, Co-ZIF-8, and Cd-ZIF-8 .....	28
3.2.6 Single-crystal X-ray structures .....	29
3.2.7 Characterizations.....	29
3.3 Results and discussion .....	30
3.4 Conclusion .....	48
<b>4. PROPYLENE-SELECTIVE THIN ZEOLITIC IMIDAZOLATE FRAMEWORK MEMBRANES ON CERAMIC TUBES BY MICROWAVE SEEDING AND SOLVOTHERMAL SECONDARY GROWTH .....</b>	<b>50</b>
4.1 Introduction .....	50
4.2 Materials and methods.....	55
4.2.1 Chemicals.....	55
4.2.2 Tubular supports .....	55
4.2.3 Microwave (MW) seeding procedures.....	55
4.2.4 Secondary growth procedures .....	56
4.2.5 Acid treatment and the reuse of tubes .....	56
4.2.6 Characterizations and permeation tests.....	57
4.3 Results and discussion .....	57
4.4 Conclusions .....	67
<b>5. SYNTHESSES OF ULTRA-THIN ZEOLITIC IMIDAZOLATE FRAMEWORK (ZIF) MEMBRANE EXHIBITING HIGH EXCEPTIONAL PROPYLENE/PROPANE SEPARATION PERFORMANCES USING THE COMBINED SEEDING METHOD .....</b>	<b>68</b>
5.1 Introduction .....	68
5.2 Materials and methods.....	71
5.2.1 Chemicals.....	71
5.2.2 Preparation of $\alpha$ -Al <sub>2</sub> O <sub>3</sub> substrate.....	72
5.2.3 Preparation of ZIF-67 seed layer using microwave-assisted seeding .....	72
5.2.4 ENACT seeding process upon microwave-seeded substrate .....	73
5.2.5 Secondary growth (SG.hereafter) .....	73
5.2.6 Tertiary growth (TG, hereafter) .....	74
5.2.7 Characterizations and permeation tests.....	74
5.3 Results and discussion .....	75
<b>6. ADDITIONAL WORKS: CONTINUOUS SYNTHESIS OF HIGH-QUALITY METAL-ORGANIC FRAMEWORK HKUST-1 CRYSTALS AND COMPOSITES VIA AEROSOL-ASSISTED SYNTHESIS .....</b>	<b>86</b>
6.1 Introduction .....	86

6.2 Materials and methods.....	88
6.2.1 Chemicals.....	88
6.2.2 Aerosol-assisted synthesis setup.....	89
6.2.3 Aerosol-assisted Synthesis of HKUST-1.....	89
6.2.4 Solvothermal Synthesis of HKUST-1.....	90
6.2.5 Synthesis of Al <sub>2</sub> O <sub>3</sub> /HKUST-1 composite.....	90
6.2.6 Synthesis of PES/HKUST-1 composite.....	90
6.2.7 Characterizations.....	91
6.3 Results and discussion.....	92
6.4 Conclusions.....	107
7. FUTURE WORK: SYNTHESIS OF HIGH-ASPECT RATIO ZIF-8 CRYSTALS FOR MEMBRANE APPLICATIONS.....	109
7.1 Introduction.....	109
7.2 Initial results.....	111
7.3 Objectives.....	116
7.3.1 Task 1, Further characterization of the powder sample.....	116
7.3.2 Task 2, Exfoliation and the formation of ultrathin membranes.....	117
8. CONCLUSION.....	118
REFERENCES.....	119



## LIST OF FIGURES

	Page
Figure 1-1 Energy saving potential of membrane separations..	2
Figure 1-2 Structure of ZIF-8.....	3
Figure 2-1 Typical cryogenic distillation procedures .....	8
Figure 2-2 Schematic illustrations of common ZIFs.....	14
Figure 2-3 Typical imidazole-based linkers for ZIF syntheses.....	15
Figure 2-4 Additional ZIF structures. ....	15
Figure 3-1 Cd-ZIF-8 powder samples with different TEA ratios after reactions at 60 °C for 6 hrs: (a) PXRD patterns and SEM images of Cd-ZIF-8 samples with TEA/L = (b) 1, (c) 0.5 and (d) 0.25 .....	32
Figure 3-2 (a) PXRD patterns for Cd-ZIF-8 with different reaction times and (b) SEM image of powder sample with a reaction time of 2 days. The samples prepared with a molar ratio of Cd:mIm:TEA:MeOH = 1:8:8:500 at 60 °C.....	34
Figure 3-3 (a) PXRD patterns and (b-d) optical microscopy images of the product of Cd-ZIF-8 single-crystal recipe reported by Tian et al. ....	34
Figure 3-4 PXRD patterns of Cd-ZIF powder samples synthesized at different reaction temperatures .....	35
Figure 3-5 Cd-ZIF-8 powder samples synthesized with various TEA/L ratios at 60 °C for 2 days: (a) PXRD patterns and (b) SEM image of the sample with TEA/L = 0.5. Large crystals in rhombic prism shapes are CdIF-3. The inset image shows Cd-ZIF-8 crystals. ....	37
Figure 3-6 SEM images of (a) CdIF-3, (b) UIP-2, and (c) UIP-1.....	37
Figure 3-7 Nitrogen isotherms of Zn-ZIF-8, Co-ZIF-8 and Cd-ZIF-8 at 77 K.....	38
Figure 3-8 SEM images of Cd-ZIF-8 with a reaction time of (a) 6 h, (b) 1 d, (c) 4 d, and (d) 7 d with the molar ratio of Cd:mIm:TEA:methanol = 1:8:8:500.....	38

Figure 3-9 ORTEP diagram of (a) Zn-ZIF-8, (b) Co-ZIF-8 and (c) Cd-ZIF-8 guest molecules, in which hydrogen atoms have been removed for clarity.....	39
Figure 3-10 FT-IR spectra and enlarged spectra (right) of Zn-ZIF-8, Co-ZIF-8, and Cd-ZIF-8. ....	41
Figure 3-11 TGA curves of Zn-ZIF-8, Co-ZIF-8 and Cd-ZIF-8 in N <sub>2</sub> . ....	41
Figure 3-12 PXRD patterns (a) and FTIR spectra (b) of CdZn-ZIF-8 with various Cd/Zn ratios in comparison with Cd-ZIF-8 and Zn-ZIF-8. Cd and Zn represent Cd-ZIF-8 and Zn-ZIF-8 while Cd <sub>x</sub> Zn <sub>1-x</sub> represents ZIF-8 with x fraction of Cd and (1-x) fraction of Zn in the synthesis solution. ....	42
Figure 4-1 A schematic illustration of (a) microwave seeding, (b) seeded tube, and (c) polycrystalline membrane after secondary growth. ZIF-8 .....	58
Figure 4-2 Scanning electron micrographs (SEMs) of ZIF-8 seed layers on the (a) bore side and (b) shell side of alumina tubes after microwave seeding.....	59
Figure 4-3. Schematic illustrations on common reasons for a low-quality seeding layer .....	59
Figure 4-4. PXRD pattern of powder sample scratched from the inner surface of the tubular membrane and the simulated pattern. ....	60
Figure 4-6 Binary propylene/propane separation factors and propylene permeances of ZIF-8 tubular membranes with increasing secondary growth time. Additional samples (five membranes from three batches) were synthesized to generate the standard error bar. ....	63
Figure 4-7. Propylene/propane separation performance of our ZIF-8 tubular ZIF-8 membranes in comparison with (a) all other membranes and (b) other ZIF-8 membranes supported on ceramic tubes. HF—hollow fiber. ....	63
Figure 4-8 Optical images of (a) loading tubular membranes into the test module and (b) a schematic illustration of its gas connections (b).....	65
Figure 4-9. Permeance and separation factors of propylene/propane separation for ZIF-8 membrane on ceramic tubular supports.....	65
Figure 4-10. Top-view and cross-section (inserted) SEM micrographs of ZIF-8 membranes on the shell side of tubular supports. The secondary growth was performed at 30°C for 6 h. ....	66

Figure 5-1. Microwave seeded support with (a) and without (b) TEA. After microwave seeding (with TEA) and ENACT seeding process (c) and their corresponding XRD patterns (d).	77
Figure 5-2. Optimization of TEA content during microwave seeding. Top-view SEM images of microwave seeded support with different TEA content (a-c) and their corresponding XRD patterns (d).	78
Figure 5-3. Schematic illustration of combined seeding process: (a) microwave-assisted seeding step, (b) ENACT seeding step, and (c) secondary growth.	79
Figure 5-4. Optimization of ENACT content during microwave seeding. Top-view SEM images of microwave seeded support with different metal and ligand concentration (a-c).	80
Figure 5-5. Comparison of SEM images for ZIF-67 membranes after secondary growth with different seeding methods: (a) only microwave seeding, (b) only ENACT seeding, (c) combined seeding, and (d) their corresponding XRD patterns. MW stands for microwave seeding here.	80
Figure 5-6. Impurity under different secondary growth conditions: (a) 120°C for 6 h (top view), (b) 90°C for 6 h, (c) 80°C for 6 h, and (d) 70°C for 2 d.	82
Figure 5-7. SEM images of ZIF-67 membrane going through same secondary growth procedure at (a) 90°C, (b) 80°C and (c) 70°C and their corresponding XRD patterns (d).	82
Figure 5-8. SEM images for ZIF-67 membranes after secondary growth at 70°C with time of (a) 6 h, (b) 1 day, and (c) 2 days as well as (d) their corresponding XRD patterns.	84
Figure 5-9. SEM images(a) and XRD(b) pattern of the ZIF-67 membrane after tertiary growth.	85
Figure 5-10. SEM images of ZIF-8 after microwave seeding (a), ENACT (b) and secondary growth (c).	85
Figure 6-1. Pictures of the AAS setup (a) and the nebulization part (b).	92
Figure 6-2. Schematic illustration for comparing our AAS process with previously reported AAS or spray-drying processes	93
Figure 6-3. Pictures of as-mixed metal solutions with methanol, ethanol, DMF, and DMSO. The molar ratio of metal: solvent = 1: 177.	95

Figure 6-4. SEM images of AAS-HKUST-1 synthesized in DMF (a) and mixed solvents with 95% (c), 75% (d), and 50% (e) of DMSO with DMF at 180 °C and PXRD (b) of sample (a). Optical images of their as-prepared (AP) solutions and residual solutions (AAS). .....	97
Figure 6-5. SEM images of AAS HKUST-1 synthesized using 50/50 DMSO/DMF at different oven temperatures: 110°C (a), 90°C (b), and 70°C (c) and the PXRD pattern of the sample at 110°C (d).....	98
Figure 6-6. N <sub>2</sub> adsorption/desorption isotherms of AAS-HKUST-1 and ST-HKUST-1.....	100
Figure 6-8. SEM images of Al <sub>2</sub> O <sub>3</sub> /HKUST-1 composite without priming, showing little incorporation of alumina nanoparticles in HKUST-1 .....	105
Figure 6-9. SEM images of PES/HKUST-1 composite structure as-synthesized (a) and as broken mechanically (b). .....	105
Figure 6-10. FTIR spectra of PES/HKUST-1 composites in comparison with those of PES and HKUST-1 (a) and the magnified view of the finger-print region (b). The stretching motion of carboxylate groups of HKUST-1 and sulfone group of PES were marked in red arrows .....	106
Figure 6-11. N <sub>2</sub> adsorption and desorption isotherms at 77K of AAS-HKUST-1, Al <sub>2</sub> O <sub>3</sub> /HKUST-1, and PES/HKUST-1. Solid and hollow circles indicate adsorption branch desorption branch, respectively.....	106
Figure 7-1. (a-c) SEM images of powder sample synthesized at 4 °C for 2 d with different concentration and (d) their corresponding PXRD pattern.....	111
Figure 7-2. Microwave seeded support covered with nanosized ZIF-8 particles ....	112
Figure 7-3. Top view of the alumina support after secondary growth of 1 day under different concentrations: (a) 40% concentration (metal:ligand:water=1:75:6750), (b) 50% (1:75:5400), (c) 65% (1:75:4150), (d) 75% (1:75:3600), (e) 85% (1:75:3176) and (f) 100% (1:75:2700).....	113
Figure 7-4. XRD pattern of the alumina supports after secondary growth of 1 day under different concentrations: 40% concentration (metal:ligand:water=1:75:6750), 50% (1:75:5400), 65% (1:75:4150), 75% (1:75:3600), 85% (1:75:3176) and 100% (1:75:2700). .....	114
Figure 7-5. SEM micrographs of alumina supports after secondary growth under 25% concentrations (metal:ligand:water=1:75:10800) of different growth time: (a) 1 day, (b) 2 days, (c) 3 days, and their corresponding XRD patterns.....	115

Figure 7-6. XRD pattern of the alumina supports after secondary growth under 50% concentrations (metal:ligand:water=1:73:5280) with a growth time of 1 d at 4°C.....116

## LIST OF TABLES

	Page
Table 2-1 Concentrations of products of FCC .....	7
Table 2-2 Operation conditions of cryogenic distillations for light hydrocarbon separations .....	8
Table 2-3 Cryogenic distillation energy cost .....	9
Table 3-1 Surface areas and pore volumes of Cd-ZIF-8, Zn-ZIF-8 and Co-ZIF-8....	39
Table 3-2 Topologies, metal-to-nitrogen bond distances and unit cell parameters of Zn-ZIF-8, Co-ZIF-8 and Cd-ZIF-8, solved from single crystal analysis at 100K.....	39
Table 3-3 Summary of experimental and crystallographic data.....	44
Table 3-4 Positional, thermal, and occupancy parameters.....	45
Table 3-4 Positional, thermal, and occupancy parameters <sup>a</sup> continued.....	46
Table 3-5 Selected interatomic distances (Å) and angles (deg) <sup>a</sup> .....	47
Table 3-6 Elemental analysis of CdZn-ZIF-8 .....	48
Table 4-1. Typical ZIF-8 tubular membranes targeting propylene/propane separation .....	54
Table 4-2. Propylene-selective zeolitic imidazolate framework (ZIF-8) membranes on polymeric hollow fibers and ceramic tubes. SF—separation factor. ....	64
Table 5-1. Summary of separation performances for different secondary growth time and temperature .....	83
Table 6-1. Donor numbers and boiling points of various solvents and the stability of corresponding precursor solutions upon stirring. ....	96
Table 6-2. Surface areas and pore volumes of AAS-HKUST-1 in comparison with those reported earlier. ST and SD represent solvothermal and spray-drying, respectively.....	100

Table 6-3. Summary of spray-drying and AAS processes applied for MOF synthesis.....	104
Table 6-4. Surface areas and pore volumes of AAS-HKUST-1, Al <sub>2</sub> O <sub>3</sub> /HKUST-1 and PES/HKUST-1 .....	107

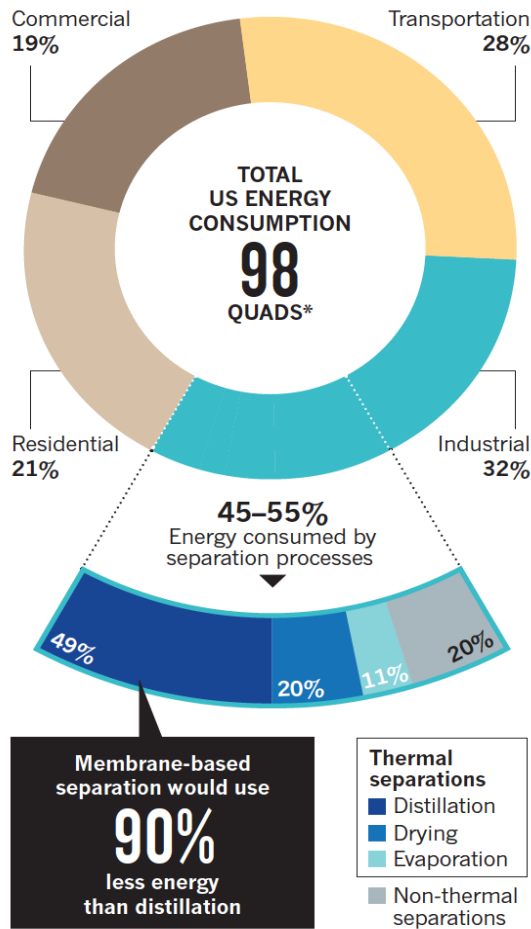
## 1. INTRODUCTION

Propylene and ethylene are of critical importance because of their production scale and their role as fundamental materials for further synthesis.[1] However, separating light olefins from their corresponding paraffins heavily relies on energy-intensive cryogenic distillations, because of their similarities in thermal properties. For example, the boiling point of propylene (225 K at 1 atm) is only 6°C higher than that of propane, resulting in relative volatility of only 1.05 to 1.1.[2] The C3-splitter column for separating propylene from propane can reach 200 feet tall with over 150 trays as well as a reflux ratio > 10,[3] which makes them extremely energy-intensive.



# CUTTING COSTS

Chemical separations account for about half of US industrial energy use and 10–15% of the nation's total energy consumption. Developing alternatives that don't use heat could make 80% of these separations 10 times more energy efficient.

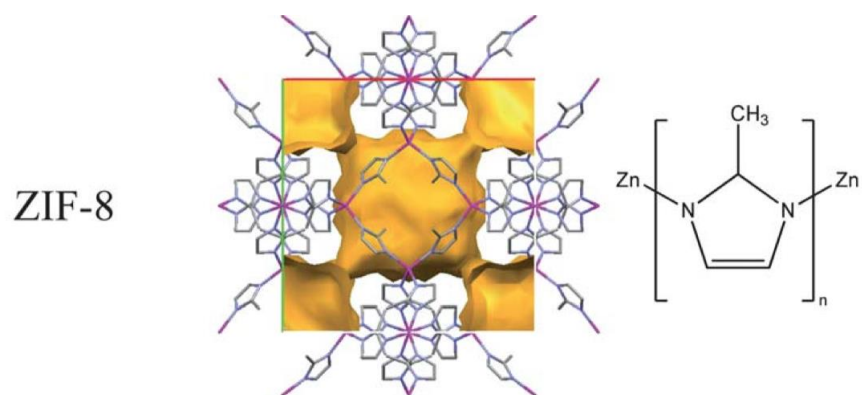


\*A quad is a unit of energy equal to  $10^{15}$  British Thermal Units (1 BTU is about 0.0003 kilowatt-hours).

**Figure 1-1 Energy saving potential of membrane separations. Reproduced with permission from [4].**

Comparing to thermal-driven separation process like distillation, membrane separations can be carried out at relatively mild conditions without phase changes

and the consequential loss of latent heat, therefore, energy-saving and environmental friendly (see Fig.1-1).[5, 6] Gas separation via membrane relies on differences of the adsorption and diffusion properties of the gas mixtures through the membrane material and generally based on three mechanisms: Knudsen diffusion, molecular sieving effect, solution-diffusion mechanism.[7] Knudsen diffusion relies on the difference of molecular weight,[8] while that of propylene and propane is less than 5%. Due to the fact that propylene/propane are similar in size (4.0/4.2 Å) as well as in intermolecular interaction with other species, numerous attempts for separating them with polymeric membranes based on solution-diffusion mechanism mostly failed to reach the commercially attractive zone.[9] There is also interesting result utilizing facilitated transportation targeting the double bond of propylene using metal nanoparticles.[10] As a member of metal organic frameworks, ZIF-8 with molecular sieving effect towards propylene/propane has been regarded as one of the most promising membrane materials.



**Figure 1-2 Structure of ZIF-8. Reprinted from [11].**

Metal-organic frameworks (MOFs) are an emerging class of crystalline nanoporous materials, comprised of inorganic nodes and organic ligands, exhibiting well-defined pores/channels/cavities as well as high porosities.[12, 13] With a judicious choice of organic linkers, the structure and properties of MOFs showed impressing adjustability and designability, thereby leading to many potential applications including gas separations,[14-17] gas storage,[18, 19] catalysis,[20, 21] drug delivery,[22, 23] and others.[24-28] In particular, zeolitic-imidazolate frameworks (ZIFs),[29-34] a subclass of MOFs, are of great practical interest due to their relatively high thermal/chemical stabilities and ultra-microporosities (i.e., pore sizes < 0.5 nm).[31] ZIFs are composed of tetrahedrally coordinated transition-metals (i.e., Zn,[31] Co,[35] Cd[36-38]) and bridged by imidazolate-derived linkers. Among many ZIFs, ZIF-8 (see Fig. 1-2)[31] has been most extensively studied for its use in gas separation applications,[39-45] mainly due to its robust synthesis protocols, thermal/chemical stability, and well-defined aperture size in the scale of small gas molecules. ZIF-8 is constituted of zinc and 2-methylimidazole (hereafter mIm) forming sodalite (SOD) topology, showing to be extremely effective for the kinetic separation of propylene (~ 4.0 Å) from propane (~ 4.3 Å)[9, 39, 40, 42, 46-53] because of its effective aperture size of ~ 4.0 Å.[40]

The first polycrystalline ZIF-8 membranes were prepared on titania disks by Bux et al.,[47] showing molecular sieving behavior. Pan and Lai et al.[42] were, however, the first to report polycrystalline ZIF-8 membranes on alumina disks showing high C2 and C3 separation performances. Following the work by Pan and

Lai et al., several groups reported polycrystalline ZIF-8 membranes supported on alumina disks exhibiting propylene/propane separation factors as high as ~ 200.[39, 54-56] ZIF-8 membranes have been prepared on various supports as well, including by planar ceramic (alumina) substrates.[39, 43, 47, 52, 54-62] include ceramic tubes,[49, 63-69] ceramic hollow fibers,[69-71] and polymeric hollow fibers.[72-78]

Just as Micheal Tsapatsis pointed out for zeolite membranes,[79] high cost for membrane manufacturing hinders the implementation of MOF/ZIF membranes, with the majority of the cost coming from the underlying porous support. To avoid the consequential long pay-back time, the performance of current MOF/ZIF membrane has to be significantly improved to reduce the demanded membrane area. The productivity of membranes can be described in the following equation, in which also lies the solution to this challenge.

$$Q_i = -\varphi_i \cdot (\Delta p_i) \cdot A \cdot l^{-1} \quad \text{Eq. 1}$$

where  $\varphi_i$ ,  $\Delta p_i$ ,  $l$  and  $A$  are the permeability of gas  $i$ , partial pressure difference of gas  $i$  between feed and permeate sides, membrane thickness, and membrane area, respectively. With a certain pressure difference, the productivity can be improved by at least three different approaches. Firstly, improving the permeability by modifying the inherent property of the membrane material. In the case of MOFs/ZIFs, fine-tuning the effective aperture sizes can be a viable option. Secondly, improving the membrane area can also provide a possible solution, which may require the use of supports with higher surface to volume ratio, therefore higher packing densities. Finally, by reducing the effective thickness of the membrane,

therefore, the hindrance for gas molecules permeating the membrane can be effectively reduced. The toolkit for this approach may include novel membrane formation methods, post-synthetic ligand exchange. As demonstrated in zeolite membrane field, the most radical solution would be the use of ultra-thin crystal flakes or even 2-D crystals.[80]

## 2. BACKGROUND AND LITERATURE REVIEW

### 2.1. Light olefins

#### 2.1.1. Production and purification process of light olefins

Ethylene and propylene are the two of the major products and the traditional way of producing them is energy intensive. The market for both of them are estimated to exceed 100 million ton per year and the majority of them are used in the production of polypropylene/polyethylene, with the rest used as the fundamental materials in the chemical industry for further synthesis.[81]

**Table 2-1 Concentrations of products of FCC. Translated and adapted from [82].**

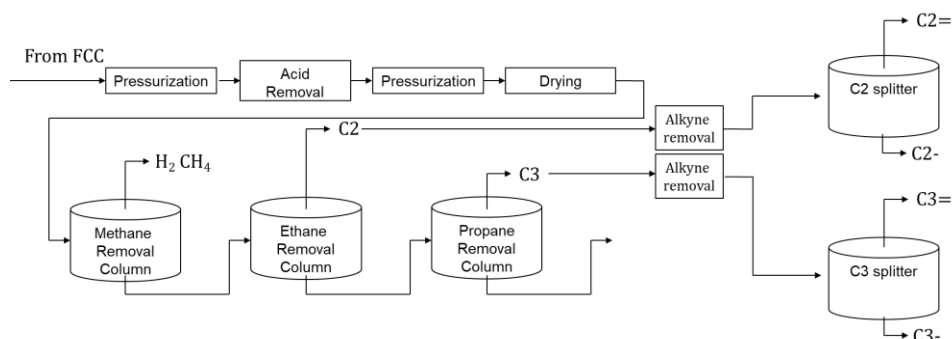
Raw material for FCC	Ethane	Light hydrocarbon	Naphtha	Light diesel	Vacuum gas oil
H <sub>2</sub>	34	18.20	14.09	13.18	12.75
Co+CO <sub>2</sub> +H <sub>2</sub> S	0.19	0.33	0.32	0.27	0.36
CH <sub>4</sub>	4.39	19.83	26.78	21.24	20.89
C <sub>2</sub> H <sub>2</sub>	0.19	0.46	0.41	0.37	0.46
C <sub>2</sub> H <sub>4</sub>	31.51	28.81	29.34	29.34	29.62
C <sub>2</sub> H <sub>6</sub>	24.35	9.27	7.58	7.58	7.03
C <sub>3</sub> H <sub>6</sub>	0.76	7.68	11.42	11.42	10.34
C <sub>3</sub> H <sub>8</sub>	-	1.55	0.36	0.36	0.22
...	...	...	...	...	...

The major source of both ethylene and propylene is the catalytic cracking process under severe conditions. However, the FCC process is inherently a free radical process and therefore, various hydrocarbons can be produced, as shown in Table 2-1 and Fig. 2-2. To obtain high-quality ethylene or propylene, the product vapor has to be compressed condensed and then fractionally distilled.[83]

**Table 2-2 Operation conditions of cryogenic distillations for light hydrocarbon separations. Translated and adapted from [82].**

Pressure/MPa	Temperature/°C
3.0~4.0	-96
0.6~1.0	-130
0.15~0.3	-140

Cryogenic distillation is generally required for separating these light gases. Two major technique routes are used in refinery plants, high-pressure ones or atm-pressure ones. As shown in Table 2-2, increasing the pressure can greatly increase the operating temperature of the methane removal column. Due to the fact that operating this rectification at ambient pressure may cause polymerization of olefins in the reboiler, most processes operate around 3.6 MPa. As shown in Fig. 2-1, a series of columns are used for such a separation. While the methane tower and the C2 splitter used most of the cold source, as can be seen from Table 2-3



**Figure 2-1 Typical cryogenic distillation procedures.**

**Table 2-3 Cryogenic distillation energy cost. Translated and adapted from [82].**

<b>Column</b>	<b>Cryogenic energy</b>
Demethanizer	52%
C2 splitter	36%
Dethanizer	9%
Others	3%

### **2.1.2. General introduction to polyolefin production**

Both propylene and ethylene has do reach different purities before being used for producing other petrochemical products. Ethylene and propylene are mainly used in the production of polyethylene/polypropylene, while ethylene can also be used in the production of ethylene oxide, ethylene dichloride, and ethylbenzene, vinyl acetate, ethanol, and acetaldehyde. More than half of propylene are used for the production of polypropylene and the rest for the following chemicals: acrylonitrile, isopropyl alcohol, n-butanol and iso-butanol, propylene oxide, cumene, and phenol.

Three grades of propylene are commercially available. They are the polymer grade (>99.5wt%), the chemical grade (93-94%), and the refinery grade (60%-70%). Polymer-grade propylene also includes additional limitations on ethylene/ethane, butane/butylene and other contaminations such as dienes, sulphur, and arsine. Reaching these purity requirments proposed a very important threshold for novel separation techniques.



The production of low-density polyethylene usually goes through a typical free-radical polymerization process. Because of the relative activity of carbon-free radical (methyl<primary<secondary<tertiary), a hydrogen transfer process will create a free radical on the polymer chain and therefore branches. However, because of the allylic group, polypropylene cannot be produced by such a process. Therefore, the production of high-density polyethylene and polypropylene heavily relies on Ziegler-Natta catalyst. However, Ziegler-Natta catalyst contains open metal site and it is extremely vulnerable for poisoning.

## **2.2. Light olefin/paraffin separations**

### **2.2.1. Drawbacks of traditional cryogenic distillations**

The separation of propylene from propane is commonly the last step in the production of polymer-grade propylene. Because of the similarity between propylene and propane, such a separation remains energy-intensive and challenging. The boiling points of propylene and propane only have a difference of 6 K (225K/213K) and their relative volatility ranges only from 1.05 to 1.1, merely above the minimum requirement for distillation. Due to the fact that the boiling points of both materials are below room temperature, precious cold source has to be provided. Or more commonly, pressurizing the distillation column. Both methods incur the energy-intensive, capital-intensive nature of propylene propane separation.[2]

### **2.2.2. Membrane methods and different membrane materials**

As mentioned above, the use of membrane instead of thermal-driven distillation can greatly reduce the energy cost. However, currently the membrane

materials are predominantly polymer-based. On one hand, operating polymeric membrane under high pressure with hydrocarbon impurities may cause problems like swelling and plasticization. On the other hand, polymeric membranes failed to satisfy the demand for propylene/propane separation. [84] Polymeric materials are not able to provide enough selectivity and permeability at the same time and there exists a significant trade-off effect. Such an effect can be explained by the fact that the propylene/propane separation in polymers is by solution-diffusion theory. The gas molecule moves through the free volume created by the flexible chains of polymer membrane. However, due to the small size difference of propylene and propane (4.0/4.2Å, respectively) and their similar affinity, such an upper bound is within expectation.

By thermally treating carbon-containing materials (mostly polymer) at an appropriate temperature, carbon molecule membrane can be formed, forming nanosized pores (even though not well-defined) and larger cavities. CMS membranes can be considered as molecular sieves and therefore have a much better separation performance than polymeric materials.[85] However, CMS membranes are currently considered hard for scaling-up.[40] In addition, there are also facilitated transport membranes for paraffin/olefin separations, utilizing the electron donor-acceptor between Ag(I) and the unsaturated C-C bonds.[86] Such a membrane has been reported of very impressive permeability and selectivity coexisting. However, it's notorious for the instability of its performance towards trace impurities (e.g. sulfur, methyl acetylene).[40]

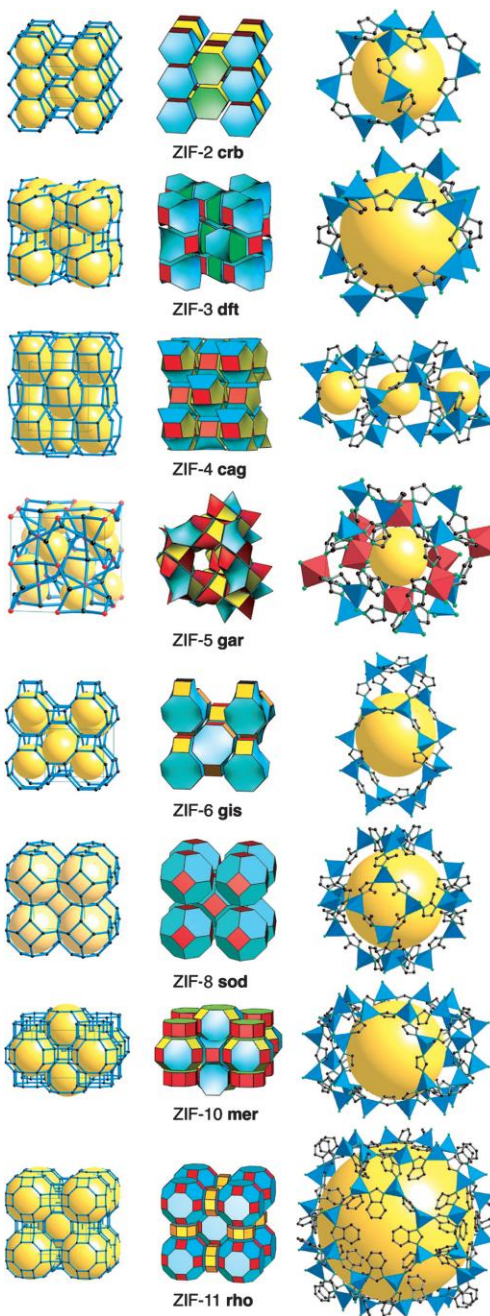
Rather than Knudsen diffusion or solution-diffusion, molecular sieves separate gas mixtures via their sieving effect. Uniform and well-defined pores exist throughout the molecular sieving materials. With the pore-size larger than the target gas yet smaller than other contents, only the target gas molecules can pass through this material. typical molecules include traditional zeolites as well as a novel material like metal organic frameworks (MOFs), covalent organic frameworks (COFs). It should be noted that zeolitic materials are generally not suitable for propylene/propane separations because of their pore sizes are usually larger than the kinetic diameter of both molecules. And several MOFs are now considered as most promising materials for C3 separation.

### **2.3. Metal organic framework (MOFs) and Zeolitic Imidazolate framework**

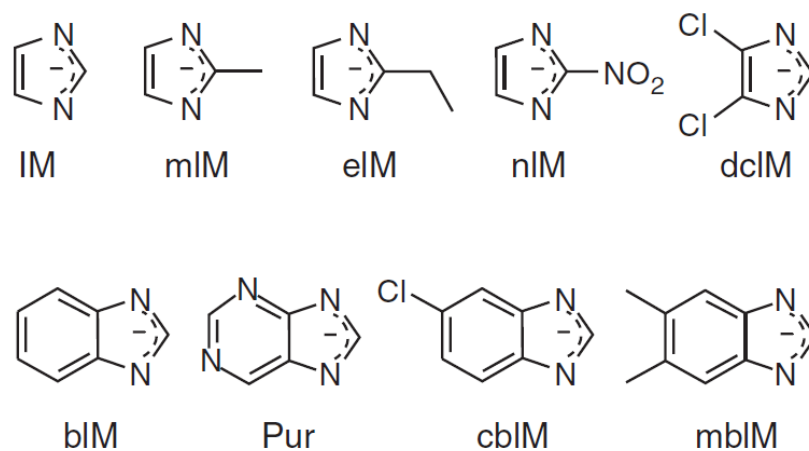
Zeolitic imidazolate framework is a subclass of MOFs and similar to other MOFs, its chemistry nature is a coordination polymer. ZIFs comprises of imidazole-derived linkers and metal centers. They interconnect with each other forming an infinite framework, whether 2-dimensional or 3-dimensional. Commonly, imidazole linkers are bidental, while the metal centers can coordinate with 4 linkers through metal-linker coordination bounds. The tetrahedral metal center resembles the Si atoms in zeolites while the ligand has the same bond angle (M-N to N-M bond angle) as oxygen atom (Si-O-Si) in zeolites (which is  $145^\circ$ )

Reported by Park, et al in 2006 alongside with various other ZIFs,[31] ZIF-8 has been draw considerate research interests because of its robust synthesis protocols, high surface area (BET surface area as high as  $1800 \text{ m}^2/\text{g}$ ) as well as

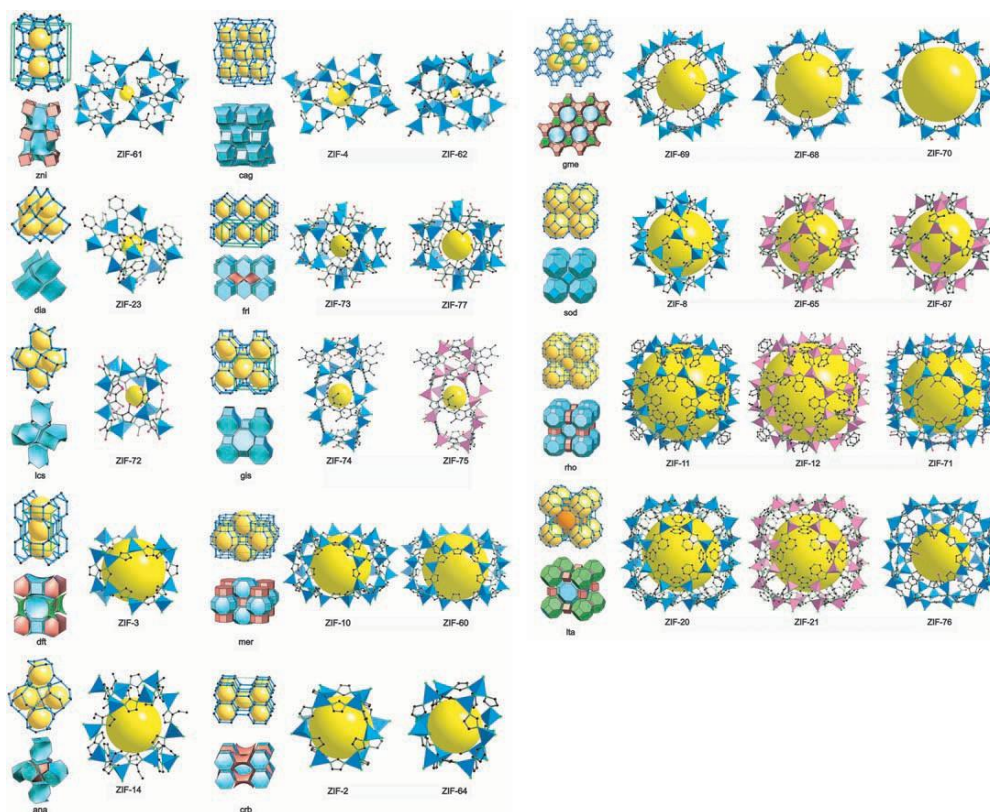
excellent chemical/thermal/water stabilities. ZIF-8 possess interconnected sodality cages with a cavity as large as 11.6 Å and these cages are separated by two kinds of apertures, 6-member rings, and 4-member rings. The 4-member rings are smaller than most of the kinetic diameter of most gases, therefore only the 6-member ring worth study for gas transport study. Several schematic illustration of MOFs/ZIFs has been included in Fig. 2-2, 2-3 and Fig. 2-4.



**Figure 2-2 Schematic illustrations of common ZIFs. Reprinted with permission from [31]. Copyright (2006) National Academy of Sciences.**



**Figure 2-3 Typical imidazole-based linkers for ZIF syntheses. Reprinted with permission from [31]. Copyright (2006) National Academy of Sciences.**



**Figure 2-4 Additional ZIF structures. Reprinted from [32] with permission from the American Association for the Advancement of Science.**

The crystallographically-defined aperture size of the six-member ring is calculated to be  $\sim 3.4 \text{ \AA}$ . However, both propylene ( $\sim 4.0 \text{ \AA}$ ) and propane ( $\sim 4.2 \text{ \AA}$ ) have shown significant gas transport through the framework, with an extremely effective preference propylene over propane, which was utilized for the kinetic separation for propylene from propane.[9, 39, 40, 42, 46-53] Such a phenomenon was due to the flipping motion of linkers,[87-91] and therefore the effective aperture size of ZIF-8 is estimated to be  $\sim 4.0 \text{ \AA}$ . [40] Based on this, ZIF-8 has been most extensively studied for its use in gas separation applications.[39, 41-45, 92]

## **2.4. The chemistry nature of ZIF-8 and its common recipes**

### **2.4.1. Gas transportation in ZIF-8**

Since the linker of ZIF-8 is bidental, there exist certain freedom of motion for the linker. Therefore, ZIF-8 (as well as similar SOD ZIFs, e.g. ZIF-67, ZIF-90) are regarded as soft framework materials. As observed by both experimental works and simulations, the pore size of ZIF-8 is a distribution instead of a set value, caused by the thermal-induced motion, which is quite different from more rigid molecular sieves like zeolites. For example, the effective aperture size of zeolite 5A matches well with its crystallographically-defined aperture size ( $4.2 \text{ \AA}$ ), consider that a complete exclusion of  $\text{CF}_2\text{Cl}_2$  was overserved.[93].

The flexibility of ZIF framework was gradually into attention because of several interesting gas adsorption behavior of ZIF-7 since 2010.[94, 95] ZIF-7 shares a very similar structure as ZIF-8. Both of them are SOD and the only difference is that in ZIF-7, benzimidazole took the place of 2-methylimidazole. In the case of ZIF-

8, there exists an interesting phenomenon. The N<sub>2</sub> adsorption (as well as other gases under certain pressure) in liquid nitrogen reveals a two-step adsorption pattern, in semi-log scale. Later it was explained by the flexibility of the framework and a structural change from ZIF-8-LP to ZIF-8-HP, which provide additional evidence for the flexibility of the framework.[46]

Even though ZIF-8 has been discovered and reported in 2006, its potential in propylene/propane separation was gradually discovered since the year of 2009. A kinetic uptake experiment was performed, in which Li et al.[53] observed the pressure change of certain gas in a sealed chamber with ZIF-8 sample. They reported a much faster absorption rate for propylene over propane inside the ZIF-8 framework despite the fact that their final adsorption amount is rather similar. In a followed-up study by Koros et al.[40] used a similar technique and examined various gases from He to iso-C<sub>4</sub>H<sub>10</sub> and further confirmed that there exists a “cut-off” region between 4.0 to 4.2 Å, which was later considered as the effective aperture size of ZIF-8. The calculated corrected diffusivity of propylene was more than 100 times that of propane. Considering the fact that the corrected diffusivity

#### **2.4.2. ZIF-8 and related membranes on ceramic planar supports**

Mixed-matrix membranes (MMM) mainly refer to membranes with a continuous phase of polymer while contains a certain percentage of a second phase distributed in the continuous phase. This concept has been widely studied for zeolites and has also been transferred into MOFs. One of the first MMM can date back to the ZIF-8/6FDA-DAM mixed matrix membranes reported by Koros et al.[40] However,



this topic is not within the scope of this work and our gist would be polycrystalline membranes.

By having ZIF crystals intergrown into each other and forming a continuous phase on the top of a porous support, a polycrystalline membrane can be formed. The first polycrystalline ZIF-8 membranes were prepared on titania disks by Bux et al.,[47] using an in-situ solvothermal synthesis. With a thickness of more than 30  $\mu\text{m}$ , their membrane was tested for gases from  $\text{H}_2$  only to  $\text{CH}_4$ . Pan and Lai et al.[43] were, however, the first to report polycrystalline ZIF-8 membranes on alumina disks showing high  $\text{C}_2$  and  $\text{C}_3$  separation performances. Instead of an in-situ method, they used slip-coating and secondary growth method. A layer of nano-sized ZIF-8 crystals was first deposited on top of their alumina disk, followed by secondary growth in an aqueous solution. The thickness of their membrane was only  $\sim 2 \mu\text{m}$  and the selectivity of 45.

Following the work by Pan and Lai et al., several groups reported polycrystalline ZIF-8 membranes supported on alumina disks exhibiting propylene/propane separation factors as high as  $\sim 200$ , [39, 54, 56, 96] and almost all works after these two used either in-situ methods or seeding-secondary growth method. So we'll look into detail by each category. In addition, polycrystalline ZIF membranes with high separation performances have been supported mostly by planar ceramic (alumina) substrates. [39, 43, 47, 52, 54, 56-62, 96, 97] ZIF membrane on other support will be introduced later.

### 2.4.3. In-situ methods

Comparing to zeolites, which can form strong covalent bonds with the ceramic support, the primary bond in ZIFs are M-N coordination bonds and is not compatible with the metal-oxygen bonds in ceramic supports. Therefore, not only heterogeneous nucleation on the support was not strongly preferred, the mechanical stability of the membrane can also be compromised. Hence, the primary of the target of the in-situ methods is to improve the affinity between ZIFs and their supports or limit the reaction to only the surface of the support. Primarily, in-situ methods consist of surface modification, counter-diffusion, and other methods.

In 2013, Shah et al.[97] reported thermal deposition technique for ZIF-8 membrane synthesis. The alumina support was slipped coated in a freshly-prepared precursor solution following by drying in an oven @ 200°C. The thickness of their membrane was estimated to be 5-20  $\mu\text{m}$  with a selectivity of  $\sim 30$  and permeance of 25 GPU $\text{s}$ .

Later this year, they reported the synthesis of ZIF-8 membrane on similar support by modifying the surface of the support with ZnO and do further growth.[60] The thickness of their membrane is 25  $\mu\text{m}$  and no selectivity was reported.

The thickness of in-situ ZIF-8 membranes was further reduced to  $\sim 1.5$  microns by using a counter diffusion method, reported by Kwon et al.[84] The growth was conducted by feeding the metal precursor solution and the ligand solution from a different side of the support. Their propylene permeance was greatly increased to  $\sim 70$  GPU $\text{s}$  and propylene/propane selectivity to 50.

The idea of modifying the surface chemistry of the ceramic supports so they can form bonds with ZIF crystals was first proposed by Caro et al.[98] in 2012 for ZIF-22 on TiO<sub>2</sub> supports. An organosilica material called 3-aminopropyl-triethoxysilane (APTES, hereafter) and they later used this technique for ZIF-90 membrane (which shares the same structure as ZIF-8).[99] And was used on ZIF-8 by Xie et al.[66] forming a 2- $\mu$ m-thick membrane on APTES-modified alumina support. However, no propylene/propane selectivity was reported.

#### **2.4.4. Seeding and secondary growth method**

Comparing to in-situ synthesis, which is typically one-step synthesis, seeding and growth method requires depositing a layer of seeds prior to the secondary growth. During the secondary step, further nucleation should be avoided therefore all the membrane crystals should primarily be grown from the seed crystals. Hence, the seeding step is of critical importance to the membrane quality. Theoretically, the seeding layer should be small, densely packed, fully covering the support surface and only monolayer coverage.

In 2013, Kwon et al.[39] reported a microwave-assisted seeding method. After having the porous alumina support soaked with the metal solution, microwave was shined right after transferring the soaked support into the ligand solution. While counter-diffusion is happening, microwave heating naturally concentrated heating on the interface of solid-liquid surface, i.e. the very surface of the support. Extensive heating promotes the nucleation of ZIF-8. Therefore, ZIF-8 seed crystals as small as 70 nm were deposited onto the support, followed by a secondary growth at 30°C.

Their membrane was reported showing and selectivity as high as 40 and permeance of 70 GPU.

Liu and Lin et al.[100] reported ZIF-8 membrane synthesized by dip-coating and secondary growth. ZIF-8 crystals of only 100 nm were first synthesized and dispersed in fresh methanol. The support was brought in contact with the suspension for twice before secondary growth in an aqueous solution for 7 h with different temperatures. The thickness of their membrane is 2.5  $\mu\text{m}$ , propylene/propane selectivity of 26 and propylene permeance of  $\sim 30$  GPU. Additional works in this category include precursor infiltration by Wang et al.[61]

## **2.5. Improvement of ZIF membranes for propylene propane separation**

Since the degree of the linker flipping motion depends largely on the nature of linkers, one straightforward way to vary the effective aperture sizes of ZIFs is by varying organic linkers, resulting in several iso-structures (i.e., the same SOD structures) of ZIF-8 such as ZIF-7 (benzimidazole, bIm),[31] ZIF-90 (imidazolate-2-carboxaldehyde, ICA),[30] and SIM-1 (4-methyl-imidazole-5-carbaldehyde).[101] Because the degree of the linker flipping also depends on the metal to linker bonds (i.e., metal-nitrogen bonds, M-N bonds), another strategy is to substitute zinc nodes with another one such as Co. Recently, Jeong and his co-workers[96] showed that Co-ZIF-8 (formerly known as ZIF-67)[32] membranes exhibit superior propylene/propane separation performances as compared to Zn-ZIF-8 membranes likely due to the fact that Co-N bonds are stiffer than Zn-N bonds, thereby smaller apertures in Co-ZIF-8.

However, accessible effective aperture sizes using the above-mentioned rather conventional approaches are still limited. By recognizing the fact that the carbon-carbon bond of the methyl group in the mIm of ZIF-8 is the weakest, Guo et al.[102] demonstrated that careful thermal treatment could lead to the systematic removal of the methyl groups, thereby potentially controlling the effective aperture of ZIF-8. Zhang et al.[103] adopted this strategy and showed that mixed-matrix membranes containing ZIF-8 particles thermally treated at different conditions exhibited a systematic difference in n-butane/iso-butane separation. Nevertheless, tuning the effective aperture of ZIF-8 by systematically removing methyl groups is quite difficult to control. Nair and his colleagues[46] were the first to show that the effective aperture of ZIF-8 could be also controlled by incorporating a mixture of linkers. They and other researchers demonstrated that the effective aperture sizes of hybrid ZIFs (mixed-linker ZIFs) could vary depending on the ratio of mIm (ZIF-8) and bIm (ZIF-7)[104] or ICA (ZIF-90).[105, 106] Since some of the organic linkers are prohibitively expensive, however, mixed-metal approach is economically more attractive.

Very recently, Jeong and his co-workers[107] demonstrated that the effective aperture size of ZIF-8 can be systematically tuned by introducing mixed metal centers (i.e., Zn and Co) with varying Co/Zn ratios. They showed that CoZn-ZIF-8 membranes exhibited enhanced propylene/propane selectivity as compared to Zn-ZIF-8 membranes prepared under similar conditions possibly due to their reduced effective apertures. It should be noted here that though hybrid MOFs (also called

multi-component MOFs) containing mixed linkers and/or mixed metal centers have been widely studied,[108-116] their applications in the separation processes are limited.

### 3. FACILE SYNTHESIS OF CD-SUBSTITUTED ZEOLITIC-IMIDAZOLATE FRAMEWORK CD-ZIF-8 AND MIXED-METAL CDZN-ZIF-8\*

#### 3.1 Introduction

As mentioned above, substituting ZIF-8 with other metal nodes, while keeping the SOD structure, can bring various merits and additional applications. For example, partial or complete substitutions of ZIF-8 can bring additional metal nodes for various catalysis applications. Bringing in substitutive metal nodes can also help to fine-tune the effective aperture sizes of ZIF-8.[107] However, this synthesis is rather difficult. Out of the few reported cases, Co-ZIF-8 (formally known as ZIF-67) seems to be the only complete success.[117] ZIF-8 was partially substituted (up to 25%) by  $\text{Cu}^{2+}$  and showed excellent catalytic activity in [3+2] cyclo-addition reactions, while higher doping percentage caused a complete collapse of ZIF-8 structure.[111] Ni-partially-substituted ZIF-8 was synthesized by mechanochemical methods and showed potentials for alcohol sensing and photocatalysis.[118] Mg-ZIF-8 was successfully synthesized with higher surface even than ZIF-8. However, the delicate synthesis condition (under argon) and the expensive reactant ( $\text{MgBH}_4$ ) reveals its extreme difficulty.[119]

Cd-ZIF-8 (formally known as CdIF-1) are also comprised of 2-methylimidazole and another Group 12 element, Cadmium. Due to the similar electron configurations and ion radius between  $\text{Zn}^{2+}$  and  $\text{Cd}^{2+}$ , Cd-ZIF-8 is expected

---

\*Reprinted with permission from “Facile synthesis of Cd-substituted zeolitic-imidazolate framework Cd-ZIF-8 and mixed-metal CdZn-ZIF-8” by Sun, Jingze, et al, 2018. Microporous and Mesoporous Materials, 264, 35-42, Copyright [2018] by Elsevier.

to be facilely synthesized under mild conditions and share similar excellent stabilities and robustness as ZIF-8. In addition, in gas separation and adsorption, the effective aperture size of ZIFs depends on the crystallographic aperture sizes as well as the flappy motions of organic linkers. By partially substitute Zn with Cd in ZIF-8, both factors might be altered and the effective aperture size of ZIF-8 might be changed. Such a method has been demonstrated in the case of CoZn-ZIF-8.[107]

Single crystals of Cd-ZIF-8 have been reported synthesized in n-butanol by Tian et al.[36] However, their Cd-ZIF-8 synthesis recipe seems not readily applicable for practical applications: large single crystals with impurities, the use of expensive n-butanol and no detailed description on varying the synthesis parameters. The synthesis protocols of ZIF-8 and its iso-structures are mostly based on methanol or water,[117, 120] n-butanol is less compatible with the synthesis of mixed-metal ZIF-8 with Cd centers.

Here we report a facile synthesis protocol for phase-pure Cd-ZIF-8 crystals in methanol. Systematic investigations led to synthesis conditions for high-quality Cd-ZIF-8 powder samples. Several crystal phases transformation from Cd-ZIF-8 was revealed and TEA was found essential in stabilizing Cd-ZIF-8 as well as in synthesizing it. With various characterizations, it was found that our Cd-ZIF-8 samples possess thermal stabilities and porosities comparable to those of Zn-ZIF-8 and Co-ZIF-8. The single-crystal structure of Cd-ZIF-8 was solved along with those of Zn-ZIF-8 and Co-ZIF-8 under similar conditions and compared the crystallographic structure. FTIR was explored to compare the flappy motion of the



linker. Cd-ZIF-8 is proved to have larger effective aperture sizes than Zn-ZIF-8. In addition, mixed-metal CdZn-ZIF-8 samples with various Cd/Zn ratios were solvothermal synthesized, showing that Cd substitution can potentially fine-tune the effective aperture size of ZIF-8. It should be noted here that Panda et al.[121] synthesized the first mixed-metal CdZn-ZIF-8 by ball milling but no detailed structural analysis was provided.

## **3.2 Experimental**

### **3.2.1 Chemicals**

Cadmium nitrate tetrahydrate (purum p.a., 99+%, Sigma-Aldrich), cadmium acetate dehydrate (purum p.a., 98+%, Sigma-Aldrich), zinc nitrate hexahydrate (98%, Sigma-Aldrich), cobalt nitrate hexahydrate (98%, Sigma-Aldrich) and cobalt chloride (purum p.a. anhydrous, 98%, Sigma-Aldrich) were used as the metal source while 2-methylimidazole (99%, Sigma-Aldrich) was used as the organic ligand source and triethylamine (TEA, 99% reagent grade, Fisher Scientific) as the deprotonating agent. Methanol (ACS low acetone 99.8%+, Alfa Aesar) was used for Zn- and Co-ZIF-8 powder synthesis. N-butanol (98+%, Fisher Scientific) and dimethylformamide (DMF, 98+%, Fisher Scientific) were used for the synthesis of Cd- and Co-ZIF-8 single crystals, respectively. All these chemicals were used without further purifications.

### 3.2.2 Synthesis of Cd-ZIF-8

The molar ratio of Cd:mIm:TEA:methanol in the synthesis precursor solution was 1:x:y:500 where x and y varied from 2 to 8. Reaction times and temperatures were varied from 6 hours to 7 days and from 60 °C to 110 °C, respectively. In a typical synthesis, 0.761 g of cadmium nitrate hexahydrate was dissolved in 19.76 g of methanol under stirring to prepare the metal solution. 2 g of TEA and 1.622 g mIm were dissolved into 19.76 g of methanol for the ligand solution. The metal solution was then poured into the ligand solution under stirring and continually stirred for 1 h. The molar ratio of the resulting precursor mixture was Cd:mIm:TEA:methanol = 1:8:8:500. The solution was then transferred into a Teflon-lined autoclave. The autoclave was placed in a convection oven at 60 °C for 48 h. After the reaction was done, the powder was collected, washed with fresh methanol, and dried under vacuum at room temperature.

### 3.2.3 Synthesis of Zn-ZIF-8 and Co-ZIF-8

Zn-ZIF-8 powder was synthesized following the recipe reported by Zhang et al.[122] In short, 0.588 g of zinc nitrate hexahydrate was dissolved in 40 ml of methanol. 0.324 g of mIm and 0.538 g of sodium formate were dissolved in 40 ml of methanol. The two solutions were mixed and reacted at 90 °C for 24 h. The sample was washed twice with fresh methanol and dried in vacuum. Co-ZIF-8 powder was synthesized following a recipe modified from the one by Tang et al.[123] 0.519 g of cobalt chloride was dissolved in 40 ml of methanol while 0.6 g of polyvinylpyrrolidone (PVP) and 2.63 g of mIm were dissolved into another 40 ml of

methanol under stirring. The two solutions were mixed and the mixture was then kept at 100 °C for 12 h. The sample was then washed with fresh methanol twice and dried in vacuum.

#### **3.2.4 Synthesis of mixed-metal Cd-Zn-ZIF-8**

Mixed-metal CdZn-ZIF-8 samples were synthesized based on the Cd-ZIF-8 synthesis protocol described above with slight modifications. The molar ratio of Cd/Zn in the synthesis solution was varied from 9 to 1. After mixing the metal solution containing both zinc salt and cadmium salt with the ligand solution, the solution was continued stirring for 1 min and then transferred into a Teflon-line autoclave. The reaction was conducted at 60 °C for 6 h. Gel-like products were collected after centrifuging with 8000 rpm for 20 min, followed by extensive washing in methanol.

#### **3.2.5 Single crystal synthesis of Zn-ZIF-8, Co-ZIF-8, and Cd-ZIF-8**

Zn-ZIF-8 and Co-ZIF-8 single crystals were synthesized according to the recipe reported by Kwon et al.[55] For Zn-ZIF-8 single crystals, 1.764 g of zinc nitrate hexahydrate was dissolved in 20 ml of methanol while 0.973 g of 2-methylimidazole and 0.404 g of sodium formate were dissolved in another 20 ml of methanol. The two solutions were mixed and the resulting mixture was poured into a 45-ml autoclave containing a glass slide and placed in a convection oven at 90 °C for 6 h. For Co-ZIF-8 single crystals, 1.05 g of cobalt nitrate hexahydrate and 0.27 g of 2-methylimidazole were dissolved in 108 ml of dimethylformamide (DMF) with 6 drops of 1M HNO<sub>3</sub>. The two solutions were mixed and the resulting mixture was

placed in a convection oven at 130 °C for 72 h. For Cd-ZIF-8 single crystals, the reported recipe by Tian et al.[36] was slightly modified. 0.267 g of cadmium acetate dihydrate was dissolved in 20 ml of n-butanol and 0.410 g of 2-methylimidazole was dissolved in 15 mL of n-butanol. The latter solution was poured into the former solution. The mixture was put in an autoclave, which was placed in a convection oven at 120 °C for 24 hours.

### **3.2.6 Single-crystal X-ray structures**

Diffraction data were collected for these three crystals using synchrotron X-radiation. Their temperatures were maintained at 100(1) K by a flow of cold nitrogen gas. Preliminary cell constants and an orientation matrix were determined from 72 sets of frames collected at scan intervals of 5° with an exposure time of 1 s per frame. The basic scale file was prepared using the HKL3000 program.[124] The reflections were successfully indexed by the automated indexing routine of the DENZO program.[124] The diffraction data were harvested by collecting 72 sets of frames with 5° scans with an exposure time of 1 s per frame. These highly redundant data sets were corrected for Lorentz and polarization effects, and a very small correction for crystal decay was applied. The space group  $I\bar{4}3m$  was determined by the XPREP program.[125] Full-matrix least-squares refinement (SHELXL2014)[126] was done on  $F^2$  using all data for the three crystals.

### **3.2.7 Characterizations**

Powder X-ray diffraction (PXRD) patterns were collected from Rigaku Miniflex II powder X-ray diffractometer with Cu-K $\alpha$  radiation ( $\lambda = 1.5406 \text{ \AA}$ ). Field

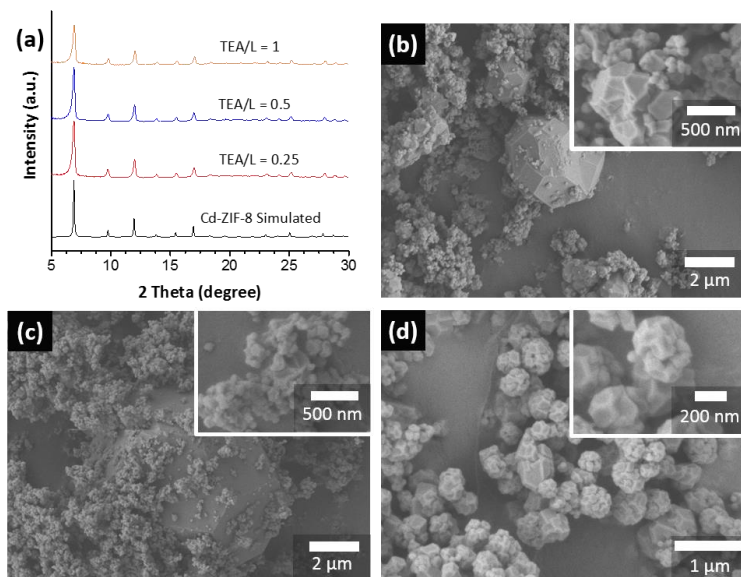
emission scanning electron micrographs were acquired from a JEOL JSM-7500F system operated at an acceleration voltage of 2 keV and a working distance of 15 mm. N<sub>2</sub> adsorption measurements were conducted using a Micrometrics ASAP 2010 system at 77K. Fourier transform infrared spectra (FT-IR) were collected using a Nicolet 100 FTIR system and potassium bromide was used to form sample mirrors. Thermal gravimetric analysis (TGA) was conducted using a Shimadzu TGA-50 system in the temperate range from room temperature to 600 °C with a ramp rate of 5 °C/min under nitrogen environment. Elemental analysis was performed on an energy dispersive X-ray fluorescence spectrometer (Shimadzu EDX-7000) with a measured range of <sup>11</sup>Na to <sup>92</sup>U, a 3 mm collimator with a silicon drift detector (SDD). Each sample was analyzed under air with the non-destructive quantitative approach. The quantitation method was carried out with an NAVI ® software. The Rh X-ray tube was operated at an excitation voltage and current of 50 kV and 1000 A, respectively. A spectrum collection time of 1000 s was used per sample.

### **3.3 Results and discussion**

Fig. 3-1 shows the PXRD patterns and SEM images of Cd-ZIF-8 crystals with various TEA/Ligand (hereafter, TEA/L) ratios synthesized at 60 °C for 6 h. The PXRD patterns of Cd-ZIF-8 match well with its simulated pattern, indicating the powder samples are phase-pure Cd-ZIF-8. The presence of TEA as a deprotonator in the synthesis solution was found essential to synthesize highly crystalline Cd-ZIF-8 powders in methanol. It should be mentioned that when water was used as a solvent, only hydroxides of cadmium were formed regardless of the TEA/L ratios.

The use of an organic base to promote the synthesis of MOFs, in particular, ZIFs, has been well-studied. For example, Gross et al.[117] reported that Zn-ZIF-8 and Co-ZIF-8 crystals could be synthesized even at room temperature in water in the presence of TEA, while Schejn et al.[127, 128] reported the synthesis of ZIF-8 crystals in methanol with TEA. It is noted that even with an excess amount of mIm (mIm to metal molar ratio of as high as 96 in methanol), there were no precipitates formed without TEA. Furthermore, our attempts to use an inorganic deprotonator such as sodium formate ( $pK_a = 7.0 - 8.5$ ) failed to produce Cd-ZIF-8 crystals. These observations suggest that TEA plays a key role in the formation of Cd-ZIF-8 crystals.

The critical role of TEA is likely due to its relatively strong basicity ( $pK_a = 10.75$ ). Gross et al.[117] showed that the desired values of TEA/L ratios were 1 and 0.5 in water and in methanol, respectively. In our case, no crystal was formed with the TEA/L ratio less than 0.25 in methanol. Unlike  $Zn^{2+}$  ions,  $Cd^{2+}$  ions prefer octahedral coordination in the presence of water.[129]  $Cd^{2+}$  ions, however, need to be tetrahedrally coordinated to form Cd-ZIF-8 structure. To reduce the coordination number of  $Cd^{2+}$  ions to form Cd-ZIF-8 structure, the reconfiguration of the surrounding solvent molecules is required, resulting in an energy barrier.[130] This possibly explains why the synthesis window for Cd-ZIF-8 is much narrower as compared to Zn- and Co-ZIF-8, even requiring a stronger base to increase the number of deprotonated ligands



**Figure 3-1 Cd-ZIF-8 powder samples with different TEA ratios after reactions at 60 °C for 6 hrs: (a) PXRD patterns and SEM images of Cd-ZIF-8 samples with TEA/L = (b) 1, (c) 0.5 and (d) 0.25**

Figs. 3-1b to 3-1d show the morphologies of Cd-ZIF-8 crystals prepared with various TEA/L ratios. As can be seen in the SEM images, high TEA/L ratios ( $> 0.5$ ) appear promoting the formation of crystals with a relatively wider size distribution including micron-sized Cd-ZIF-8 crystals. On the contrary, with the TEA/L of 0.25, crystals are relatively uniform in size of less than 500 nm and no micron-sized crystals can be detected. The majority of the individual Cd-ZIF-8 crystals are nano-sized and they look somewhat different from typical ZIF-8 crystals of similar size. As can be seen in the inset of Fig. 3-1d, individual crystals seem to be inter-grown to each other, forming agglomerates of similar size. Li et al.[131] observed that many of nano-sized Zn-ZIF-8 and Co-ZIF-8 formed agglomerates when synthesized in the

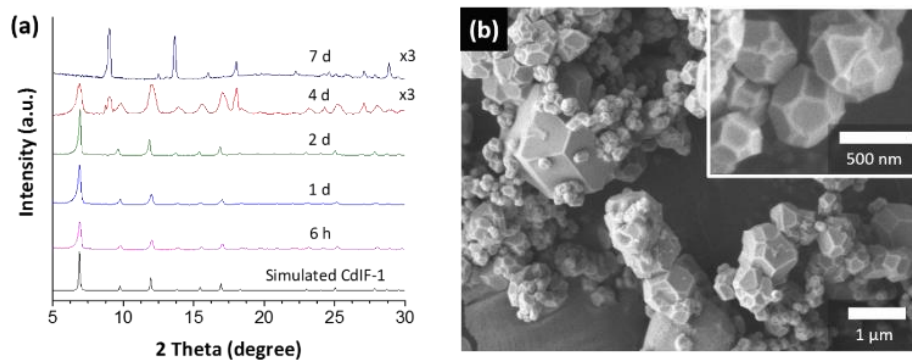
presence of TEA. They attributed this to the high nucleation rates resulting from the presence of TEA, thereby leading to the formation of small crystals.

The time-dependent formation of Cd-ZIF-8 was studied by varying the synthesis time from 6 h to 7 days. Fig. 3-2a shows the PXRD patterns of the resulting samples. Cd-ZIF-8 was found to be meta-stable, which is not like Zn- and Co-ZIF-8. As presented in Figs. 3-2a and 3-3, the increase in the reaction time led to the improvement in the crystallinity of Cd-ZIF-8 crystals until 2 days. Fig. 3-2b shows the SEM image of Cd-ZIF-8 crystals synthesized for 2 days, exhibiting much improved morphology as compared to those for 6 h. Further characterizations were carried out with Cd-ZIF-8 crystals synthesized for 2 days. When the reaction time was extended to 4 days, however, there was an unknown phase formed along with Cd-ZIF-8. Furthermore, the crystallinity and morphology of the Cd-ZIF-8 phase synthesized for 4 days were found greatly compromised as shown in Figs. 3-2a and 3-3b. Upon 7 days of reaction, an unidentified crystalline impurity phase (hereafter, UIP-1) was observed. This phase change upon elongated reaction time strongly suggests that Cd-ZIF-8 is not as stable as Zn-ZIF-8 and Co-ZIF-8.

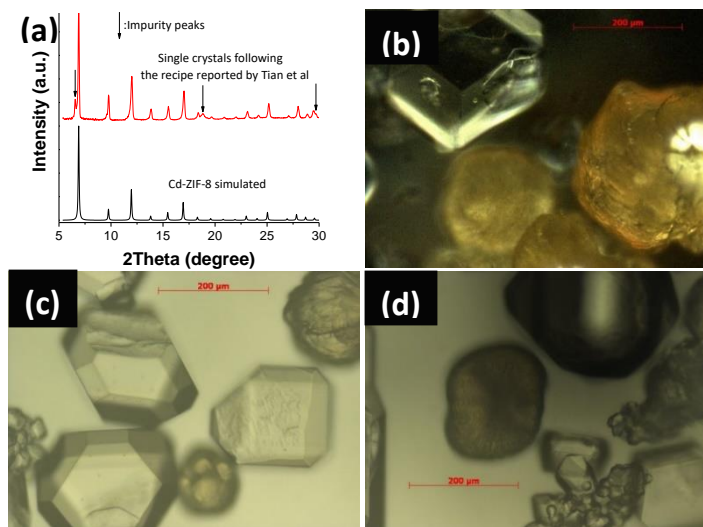
To further test the meta-stable nature of Cd-ZIF-8, the reaction temperature was varied from 60 °C to 130 °C for 2 days with the Cd:mIm:TEA:MeOH of 1:8:8:500. When the reaction temperature was increased to 75 °C, an unidentified crystalline impurity phase different from UIP-1 (hereafter, UIP-2) was formed as shown in Figs. 3-4 and 3-6b. At 90 °C, only pure UIP-2 was formed with Cd-ZIF-8 phase. Phase changes upon elevated reaction temperature as well as upon elongated



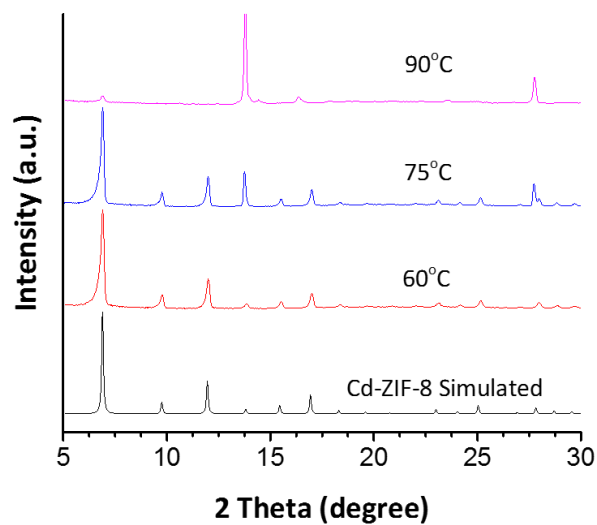
reaction time strongly indicate that Cd-ZIF-8 is not as stable, thereby relatively easily transforming to two unknown phases (UIP-1 and UIP-2).



**Figure 3-2 (a) PXRD patterns for Cd-ZIF-8 with different reaction times and (b) SEM image of powder sample with a reaction time of 2 days. The samples prepared with a molar ratio of Cd:mIm:TEA:MeOH = 1:8:8:500 at 60 °C.**



**Figure 3-3 (a) PXRD patterns and (b-d) optical microscopy images of the product of Cd-ZIF-8 single-crystal recipe reported by Tian et al.[36]**



**Figure 3-4 PXRD patterns of Cd-ZIF powder samples synthesized at different reaction temperatures**

The effect of TEA on the stabilization of Cd-ZIF-8 (i.e., resistance to the phase transformation) was determined by extending the synthesis time (i.e., 2 days) with various TEA/L ratios. As shown in Fig. 3-5a, with the TEA/L ratio of 0.25, CdIF-3 phase[36] was formed, while with the TEA/L ratio of 0.5, Cd-ZIF-8 formed along with CdIF-3 (see Fig. 3-5b). When the amount of TEA was further increased (TEA/L = 1), however, phase-pure Cd-ZIF-8 crystals were obtained. This strongly suggests that TEA not only promotes the formation of Cd-ZIF-8 but also stabilizes Cd-ZIF-8 (i.e., prohibiting Cd-ZIF-8 from transforming into CdIF-3).

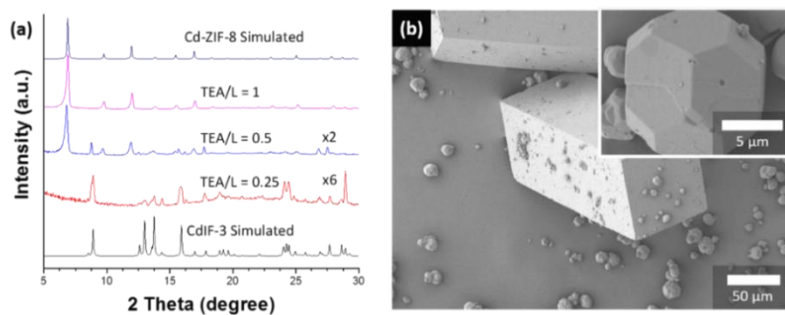
As described above, Cd-ZIF-8 appears to readily undergo phase transformations into three different phases depending on conditions as summarized in Fig. 3-6. Such transformations indicate these three crystalline phases are

thermodynamically more favorable than Cd-ZIF-8, possibly explaining why Tian et al.[36] was unable to obtain phase-pure Cd-ZIF-8 single crystals.

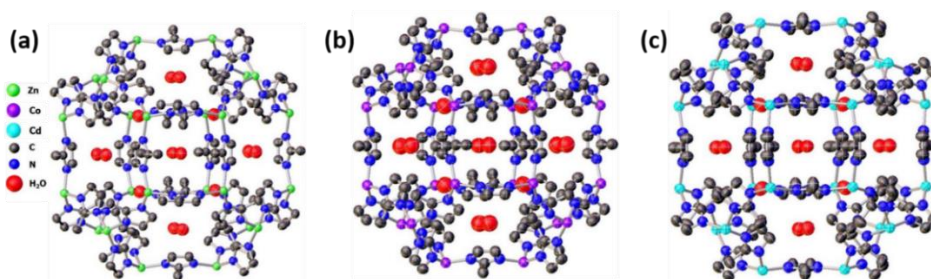
Figs. 3-7 and 3-8 present the N<sub>2</sub> isotherms of Cd-ZIF-8 in comparison with Zn-ZIF-8 and Co-ZIF-8. The isotherms of Zn-ZIF-8 and Co-ZIF-8 exhibit a typical two-step adsorption resulting from the flexibility of the ligands.[46, 69] On the contrary, the isotherm of Cd-ZIF-8 is distinctively different in two ways: 1) only single sharp step around  $P/P_0 \sim 0.00001$  and 2) subsequent gradual increase of adsorption without no obvious plateau (i.e., no saturation). This indicates that the flexibility of linkers in Cd-ZIF-8 has less effect on the N<sub>2</sub> adsorption as compared to Zn- and Co-ZIF-8 and a relatively larger non-porous surface area for Cd-ZIF-8 is present possibly due to the unique morphology of Cd-ZIF-8. As shown in Table 3-1, Cd-ZIF-8 has much larger external surface area as compared to Zn-ZIF-8 and Co-ZIF-8. It is noted that the Langmuir surface area of Cd-ZIF-8 is slightly lower than that reported by Tian et al.[36] (1985 m<sup>2</sup>/g vs. 2400 m<sup>2</sup>/g). The use of TEA in aqueous synthesis often leads to ZIF-8 powders with the BET surface area of  $\sim 1,000$  m<sup>2</sup>/g, [117, 128] significantly less than that of ZIF-8 ( $\sim 1,500$  m<sup>2</sup>/g)[31] prepared in the absence of TEA. This slight decrease in the surface area might be attributed to defects resulting from TEA.

Metal-nitrogen (hereafter, M-N) distances and metal-mIm-metal (hereafter, M-mIm-M) bond angles are important factors for determining crystallographically-defined aperture sizes. The structure of Cd-ZIF-8 was compared with those of Zn-ZIF-8 and Co-ZIF-8. Since structures solved at different temperatures might lead to

differences in bond distances and angles, the single crystal structures of all three ZIF-8 iso-structures were determined under the same conditions at 100K (see Tables 3-3 to 3-5 and Fig. 3-9). Table 3-2 compared the M-mIm-M bond angles, the M-N bond lengths, and unit cell parameters of three ZIF-8 structures at 100 K (see Fig. 3-9). While Co-ZIF-8 and Zn-ZIF-8 shares similar bond angles, bond distances, and unit cell parameters, Cd-ZIF-8 shows the longer M-N bond length, the smaller M-mIm-M angle, and the larger cell parameter, thereby exhibiting the largest crystallographically-defined aperture size of 3.6 Å.



**Figure 3-5 Cd-ZIF-8 powder samples synthesized with various TEA/L ratios at 60 °C for 2 days: (a) PXRD patterns and (b) SEM image of the sample with TEA/L = 0.5. Large crystals in rhombic prism shapes are CdIF-3. The inset image shows Cd-ZIF-8 crystals.**



**Figure 3-6 SEM images of (a) CdIF-3, (b) UIP-2, and (c) UIP-1.**

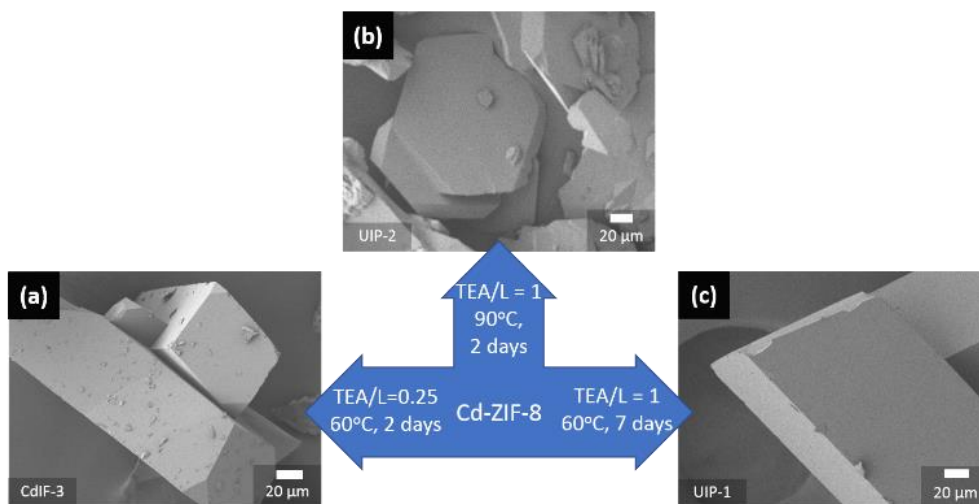


Figure 3-7 Nitrogen isotherms of Zn-ZIF-8, Co-ZIF-8 and Cd-ZIF-8 at 77 K.

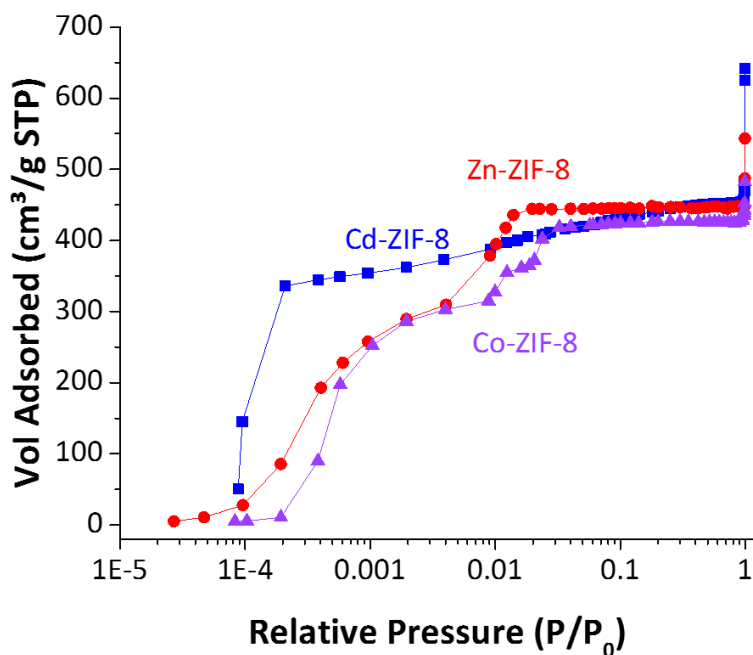
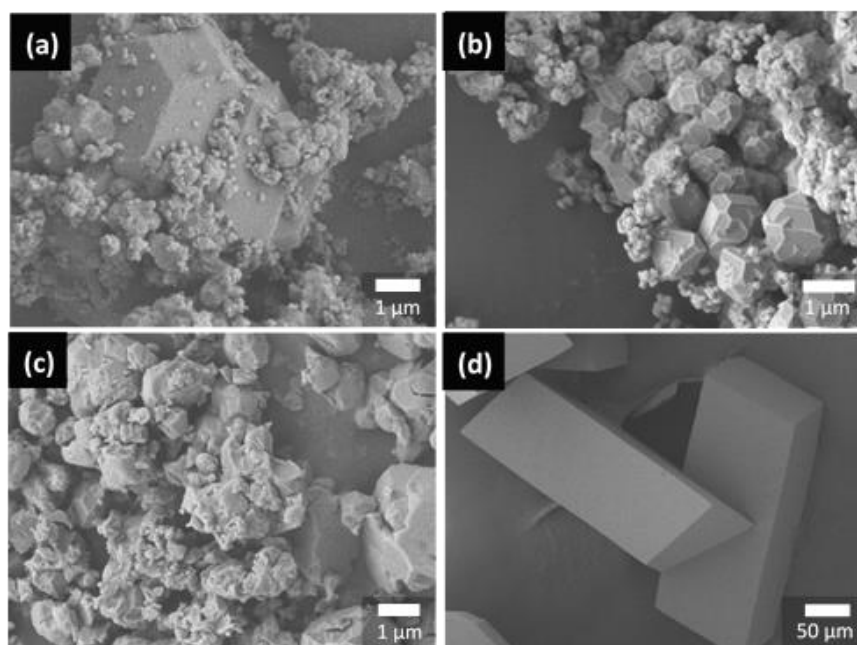


Figure 3-8 SEM images of Cd-ZIF-8 with a reaction time of (a) 6 h, (b) 1 d, (c) 4 d, and (d) 7 d with the molar ratio of Cd:mIm:TEA:methanol = 1:8:8:500.



**Figure 3-9** ORTEP diagram of (a) Zn-ZIF-8, (b) Co-ZIF-8 and (c) Cd-ZIF-8 guest molecules, in which hydrogen atoms have been removed for clarity.

**Table 3-1** Surface areas and pore volumes of Cd-ZIF-8, Zn-ZIF-8 and Co-ZIF-8.

	BET surface area m <sup>2</sup> /g	Langmuir surface area m <sup>2</sup> /g	Pore volume cm <sup>3</sup> /g	External surface area m <sup>2</sup> /g
Cd-ZIF-8	1746 ± 11	1985 ± 2	0.5913	218
Zn-ZIF-8	1434 ± 4	1941 ± 4	0.6791	28
Co-ZIF-8	1616 ± 32	1861 ± 2	0.6390	46

**Table 3-2** Topologies, metal-to-nitrogen bond distances and unit cell parameters of Zn-ZIF-8, Co-ZIF-8 and Cd-ZIF-8, solved from single crystal analysis at 100K.

	Bond angle M-(mIm)-M /degree	M-N distance/Å	Cell parameter/Å
Zn-ZIF-8	143.714	1.980(2)	16.985(2)
Co-ZIF-8	144.542	1.994(3)	17.003(2)
Cd-ZIF-8	138.502	2.182(4)	17.902(2)

In addition to the crystallographically-defined aperture size, the effective aperture size is determined by the mechanical strength of the M-N bonds. Fig. 3-10 shows the FT-IR spectra of Zn-ZIF-8, Co-ZIF-8, and Cd-ZIF-8. As compared to the  $\nu_{\text{Zn-N}}$ , the  $\nu_{\text{Co-N}}$  shows a clear blue shift as reported,[96] while the  $\nu_{\text{Cd-N}}$  exhibits a redshift. Kwon et al.[96] attributed the blue shift to the fact that the Co-N bond is mechanically more rigid than the Zn-N bond, leading to the smaller effective aperture in Co-ZIF-8. Similarly, the redshift can be caused by the fact that the Cd-N bond is mechanically less rigid than Zn-N bond in Zn-ZIF-8. In combination with the fact that the crystallographically-defined aperture size of Cd-ZIF-8 is  $\sim 3.6 \text{ \AA}$ , the fact that Cd-N bond is stiffer than the Zn-N and Co-N bonds strongly suggests that its effective aperture is likely much larger than Zn-ZIF-8, possibly enabling Cd-ZIF-8 to separate molecules bulkier than propylene and propane.

Fig. 3-11 shows the TGA curves for activated Zn-ZIF-8, Co-ZIF-8, and Cd-ZIF-8. It appears that Zn-ZIF-8 and Cd-ZIF-8 are thermally most and least stable, respectively, indicating that Zn-N and Cd-N bonds are likely to be the strongest and the weakest, respectively.

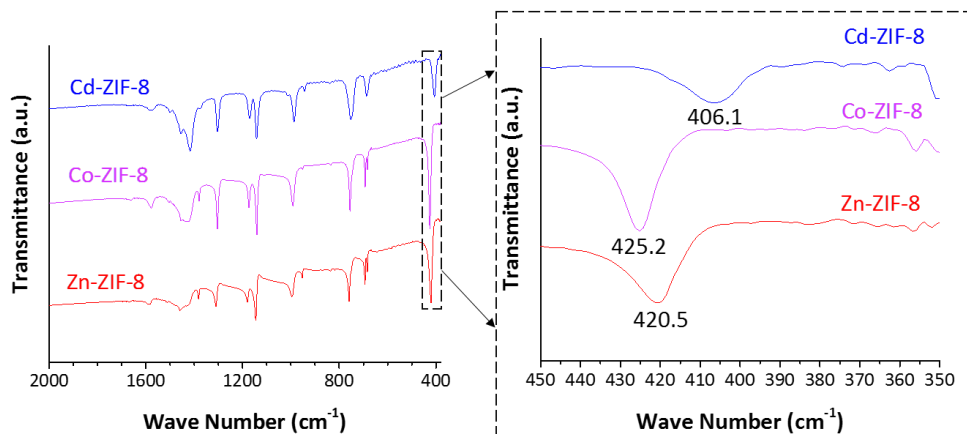


Figure 3-10 FT-IR spectra and enlarged spectra (right) of Zn-ZIF-8, Co-ZIF-8, and Cd-ZIF-8.

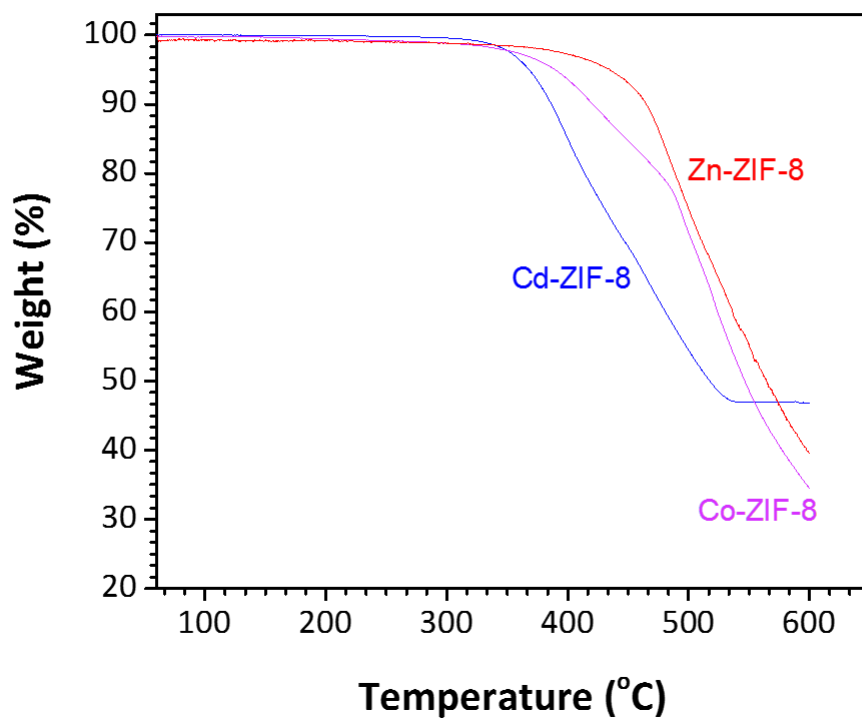
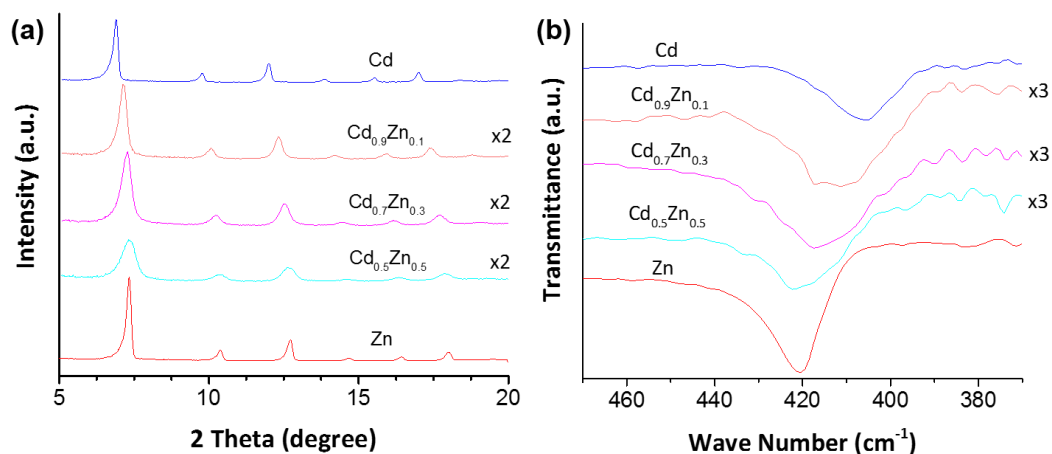


Figure 3-11 TGA curves of Zn-ZIF-8, Co-ZIF-8 and Cd-ZIF-8 in N<sub>2</sub>.





**Figure 3-12** PXRD patterns (a) and FTIR spectra (b) of CdZn-ZIF-8 with various Cd/Zn ratios in comparison with Cd-ZIF-8 and Zn-ZIF-8. Cd and Zn represent Cd-ZIF-8 and Zn-ZIF-8 while  $Cd_xZn_{1-x}$  represents ZIF-8 with  $x$  fraction of Cd and  $(1-x)$  fraction of Zn in the synthesis solution.

Finally, ZIF-8 with mixed metal centers (Zn and Cd, hereafter CdZn-ZIF-8) was synthesized to demonstrate the possibility of tuning the effective aperture size of Zn-ZIF-8 by systematically incorporating Cd centers. As Cd/Zn ratio increases, there were systematic down-shifts in the PXRD peaks (see Fig. 3-12a) and systematic red-shifts in the M-N stretching bands (see Fig. 3-12b). Given the fact that the 110 peaks of Cd-ZIF-8 and Zn-ZIF-8 are noticeably separated (by  $\sim 0.48$  degree in 2 theta) in combination with the presence of single 110 peaks in CdZn-ZIF-8 samples, it is likely that Cd centers were incorporated into the ZIF-8 frameworks, rather than a simple physical mixture of two structures. Judging from the intensity of the PXRD patterns, our CdZn-ZIF-8 samples are not as crystalline as single-metal ZIF-8. Further synthetic optimization is necessary to improve the crystallinity of CdZn-ZIF-8.

Elemental analysis revealed the composition of Cd and Zn in CdZn-ZIF-8 samples as summarized in Table 3-6. The Zn contents in CdZn-ZIF-8 samples are much higher than those in the synthesis solution. This indicates that the smaller Zn ions can be more readily incorporated into the framework as compared to the larger Cd ions.

**Table 3-3 Summary of experimental and crystallographic data**

	Zn-ZIF-8	Co-ZIF-8	Cd-ZIF-8
Empirical formula	C24 H60 N12 O5 Zn12	C24 H60 N12 O5 Co12	C24 H60 N12 O5 Cd12
Crystal cross-section (mm)	0.18	0.21	0.20
Crystal color	Colorless	Purple	Ivory white ?
Data collection T (K)	100(1)	100(1)	100(1)
Space group, Z	$I\bar{4}3m$ , 2	$I\bar{4}3m$ , 2	$I\bar{4}3m$ , 2
X-ray source	PLS <sup>a</sup> Beamline 2D SMC		
Wavelength (Å)	0.70000	0.70000	0.70000
Detector to crystal distance (mm)	63	63	63
Unit cell constant, a (Å)	16.9779(3)	17.0035(4)	17.8757(3)
2θ range in data collection (deg)	66.85	66.84	66.97
Total reflections harvested	55,366	55,811	54,777
No. of unique reflections, <i>m</i>	1,786	1,774	1,849
No. of reflections with $F_o > 4\sigma(F_o)$	1,702	1,423	1,778
No. of variables, <i>s</i>	41	41	41
Data/parameter ratio, <i>m/s</i>	43.6	43.3	45.1
Weighting parameters, <i>a/b</i>	0.132/0.1	0.128/0	0.113/0
$R_{\text{int}}^b$	0.0070	0.0075	0.0155
$R_{\text{sigma}}^c$	0.0099	0.0139	0.0179
Final error indices			
$R_1/wR_2 (F_o > 4\sigma(F_o))^d$	0.0718/0.1678	0.0618/0.1658	0.0656/0.1483
$R_1/wR_2$ (all intensities) <sup>e</sup>	0.0741/0.1732	0.0708/0.1899	0.0672/0.1519
Goodness-of-fit <sup>f</sup>	1.180	1.074	1.241

<sup>a</sup>Pohang Light Source, Korea. <sup>b</sup> $R_{\text{int}} = \Sigma|F_o^2 - F_c^2|(\text{mean})/\Sigma[F_o^2]$ ;  $R_{\text{int}}$  is calculated from the merging of equivalent data for internal agreement for all reflections. <sup>c</sup> $R_{\text{sigma}} = \Sigma[\sigma(F_o^2)]/\Sigma[F_o^2]$  <sup>d</sup> $R_1 = \Sigma|F_o - |F_c||/\Sigma F_o$  and  $wR_2 = [\Sigma w(F_o^2 - F_c^2)^2/\Sigma w(F_o^2)^2]^{1/2}$ ;  $R_1$  and  $wR_2$  are calculated using only the reflections for which  $F_o > 4\sigma(F_o)$ . <sup>e</sup> $R_1$  and  $wR_2$  are calculated using all unique reflections measured. <sup>f</sup>Goodness-of-fit =  $[\Sigma w(F_o^2 - F_c^2)^2/(m-s)]^{1/2}$ , where *m* is the number of unique reflections and *s* is the number of variables, respectively.

**Table 3-4 Positional, thermal, and occupancy parameters**

atom	Wyckoff position	x	y	z	$U_{11}^b$ or $U_{iso}$	$U_{22}$	$U_{33}$	$U_{23}$	$U_{13}$	$U_{12}$	Occupancy <sup>c</sup>
Zn-ZIF											
Zn1	12( <i>d</i> )	0	5000	7500	478(3)	478(3)	469(3)	0	0	0	12
N1	48( <i>h</i> )	4105(1)	-330(1)	6826(1)	520(9)	521(9)	528(9)	-2(7)	-20(7)	-23(7)	48
C1	24( <i>g</i> )	3773(1)	57(4)	6227(1)	517(7)	533(17)	517(7)	2(10)	-8(9)	-2(10)	24
C2	48( <i>h</i> )	3698(2)	-1032(2)	6869(2)	611(12)	524(10)	588(10)	54(9)	-43(9)	-44(8)	48
H2a	48( <i>h</i> )	4055	-1471	6788	689						
H2b	48( <i>h</i> )	3458	-1088	7385	689						
C3	24( <i>g</i> )	4052(2)	852(2)	5949(2)	635(12)	525(14)	635(12)	69(10)	-59(14)	-69(10)	24
H3a	24( <i>g</i> )	4487	1021	6267	897						
H3b	24( <i>g</i> )	3629	1225	5992	897						
H3c	24( <i>g</i> )	4126	8155	5409	897						
O1	12( <i>e</i> )	5000	2503(5)	5000	1028(45)	1116(61)	1028(45)	0	-83(78)	0	12
O2	8( <i>c</i> )	2512(7)	-2512(7)	7489(7)	1082(45)	1082(45)	1082(45)	-85(25)	85(25)	85(25)	8
Co-ZIF											
Co1	12( <i>d</i> )	0	5000	7500	715(3)	715(3)	707(4)	0	0	0	12
N1	48( <i>h</i> )	902(1)	5322(1)	8177(1)	774(10)	749(9)	770(10)	3(7)	-20(7)	-23(7)	48
C1	24( <i>g</i> )	1226(1)	4938(3)	8774(1)	767(8)	762(17)	767(8)	-8(10)	8(9)	8(10)	24
C2	48( <i>h</i> )	1313(2)	6016(1)	8127(2)	860(13)	761(11)	824(12)	66(9)	-47(10)	-49(8)	48
H2a	48( <i>h</i> )	1552	6065	7611	978						
H2b	48( <i>h</i> )	960	4148	8204	978						
C3	24( <i>g</i> )	938(2)	4148(2)	9062(2)	855(12)	789(15)	855(12)	86(10)	-83(14)	-86(10)	24

**Table 3-4 Positional, thermal, and occupancy parameters<sup>a</sup> continued**

atom	Wyckoff position	x	y	z	$U_{11}^b$ or $U_{iso}$	$U_{22}$	$U_{33}$	$U_{23}$	$U_{13}$	$U_{12}$	Occupancy <sup>c</sup>
H3a	24(g)	506	3977	8742	1250						
H3b	24(g)	769	4193	9599	1250						
H3c	24(g)	1357	3771	9028	1250						
O1	12(e)	0	2529(7)	10000	1599(62)	1843(90)	1599(62)	0	-138(88)	0	12
O2	8(c)	2493(9)	7507(9)	7507(9)	1787(67)	1787(67)	1787(67)	-19(46)	19(46)	19(46)	8
Cd-ZIF											
Cd1	12(d)	0	-2500	5000	729(3)	709(3)	729(3)	0	0	0	12
N1	48(h)	893(2)	-1774(2)	5417(2)	806(14)	815(14)	724(13)	37(10)	10(10)	-42(11)	48
C1	24(g)	1284(2)	-1284(2)	5051(9)	777(10)	777(10)	668(35)	-1(17)	1(17)	-62(12)	24
C2	48(h)	1136(3)	-1684(3)	6141(2)	980(23)	973(25)	718(16)	20(15)	2(15)	-202(20)	48
H2a	48(h)	1338	-2151	6330	1068						
H2b	48(h)	722	-1535	6459	1068						
C3	24(g)	1165(6)	-1165(2)	4186(5)	1210(38)	1210(38)	762(28)	165(27)	-165(27)	-341(45)	24
H3a	24(g)	1498	-782	4011	1591						
H3b	24(g)	657	-1016	4094	1591						
H3c	24(g)	1267	-1624	3927	1591						
O1	12(e)	0	0	2537(9)	1112(51)	1112(51)	1653(129)	0	0	-100(162)	12
O2	8(c)	2490(26)	-2490(26)	7510(26)	1267(62)	1267(62)	1267(62)	35(39)	-35(39)	-35(39)	8

<sup>a</sup>Positional and thermal parameters  $\times 104$  are given. Numbers in parentheses are the esds in the units of the least significant figure given for the corresponding parameter. <sup>b</sup>The anisotropic temperature factor is  $\exp[-2\pi^2a^{-2}(U_{11}h_1^2 + U_{22}k_2^2 + U_{33}l_2^2 + 2U_{23}k_1l_2 + 2U_{13}h_1l_2 + 2U_{12}h_1k_2)]$ . <sup>c</sup>The Occupancy factor is given as the number of atoms.

**Table 3-5 Selected interatomic distances (Å) and angles (deg)<sup>a</sup>**

	Zn-ZIF	Co-ZIF	Cd-ZIF
Zn1-N1	1.9831(20)	-	-
Co1-N1	-	1.9935(19)	-
Cd1-N1	-	-	2.188(4)
N1-C1	1.336(4)	1.328(3)	1.298(8)
N1-C2	1.380(3)	1.374(3)	1.375(6)
C1-C3	1.506(7)	1.511(6)	1.574(17)
C2-H2a	0.97	0.97	0.97
C2-H2b	0.97	0.97	0.97
C3-H3a	0.96	0.96	0.96
C3-H3b	0.96	0.96	0.96
C3-H3c	0.96	0.96	0.96
H2a···O2	3.377	2.933	3.010
H2b···O2	2.907	3.374	4.054
H3a···O1	3.423	3.375	4.009
H3b···O1	3.600	3.191	3.525
H3c···O1	3.234	3.538	4.441
N1-Zn1-N1	109.44(6)	-	-
	109.53(13)	-	-
N1-Co1-N1	-	109.45(6)	-
	-	109.52(12)	-
N1-Cd1-N1	-	-	107.27(18)
	-	-	110.58(9)
Zn1-N1-C1	128.55(24)	-	-
Zn1-N1-C2	126.72(18)	-	-
Co1-N1-C1	-	128.875(21)	-
Co1-N1-C2	-	126.23(16)	-
Cd1-N1-C1	-	-	128.4(6)
Cd1-N1-C2	-	-	128.35(24)
N1-C1-C3	123.22(22)	123.41(19)	120.9(6)
N1-C1-N1	113.6(4)	113.2(4)	118.2(12)
N1-C2-C2	108.49(14)	108.40(13)	107.27(18)
N1-C2-H2a	110	110.02	110.14
N1-C2-H2b	110	110.02	110.14
C1-N1-C2	104.7(3)	105.00(24)	103.0(7)
C2-C2-H2a	110	110.01	110.14
C2-C2-H2b	110	110.02	110.14
C1-C3-H3a	109.47	109.47	109.47
C1-C3-H3b	109.47	109.47	109.47
C1-C3-H3c	109.47	109.47	109.47
C2-H2a···O2	82.30	110.79	132.27
C2-H2b···O2	111.59	83.32	64.03
C3-H3a···O1	93.55	93.23	92.79
C3-H3b···O1	83.05	104.77	126.38
C3-H3c···O1	105.53	83.45	67.37

<sup>a</sup>The numbers in parentheses are the estimated standard deviations in the units of the least significant digit given for the corresponding parameter.

**Table 3-6 Elemental analysis of CdZn-ZIF-8**

	<b>Mol% Zn in synthesis solution</b>	<b>Mol% Zn incorporated into framework*</b>
Cd <sub>0.9</sub> Zn <sub>0.1</sub> -ZIF-8	10 mol%	25.2 mol%
Cd <sub>0.7</sub> Zn <sub>0.3</sub> -ZIF-8	30 mol%	49.5 mol%
Cd <sub>0.5</sub> Zn <sub>0.5</sub> -ZIF-8	50 mol%	99.2 mol%

\*with respect to the total metal

### 3.4 Conclusion

Phase-pure Cd-ZIF-8 powders were successfully synthesized using methanol as a solvent. The presence of TEA was found critical for the synthesis of Cd-ZIF-8. Cd-ZIF-8 was found not as stable as Zn- and Co-ZIF-8 during synthesis, easily undergoing phase transformation into either unknown crystalline phases or CdIF-3. It was found that TEA improves the resistance of Cd-ZIF-8 phase transformation. Single crystal structure analysis showed that Cd-ZIF-8 possessed the larger unit cell with the longer M-N bonds as compared to both Zn- and Co-ZIF-8, thereby the largest crystallographically-defined aperture (~ 3.6 Å). Furthermore, the Cd-N vibration was red-shifted relative to both Zn-N and Co-N vibration, suggesting the Cd-N bond is the stiffest. The largest crystallographically-defined aperture in combination of the stiffest Cd-N bond in Cd-ZIF-8 strongly indicates that the effective aperture size of Cd-ZIF-8 is likely the largest among three ZIF-8 phases. Finally, the first mixed metal CdZn-ZIF-8 crystals with various Cd/Zn ratios were solvothermally synthesized and shown to exhibit the systematic down-shifts in the XRD peaks as well as the systematic red-shifts in the M-N vibrations. While the

systematic down-shifts in the XRD peaks correlate with the systematic increase in the unit cell dimension, the systematic down-shift in the M-N vibration has to do with the systematic control in the mechanical strength of the M-N bonds. This ability to systematically control both the unit cell dimension and the M-N bond stiffness by varying the framework Cd/Zn ratio would provide an important means to fine-tune the effective aperture sizes of ZIF-8 iso-structures.



## 4. PROPYLENE-SELECTIVE THIN ZEOLITIC IMIDAZOLATE FRAMEWORK MEMBRANES ON CERAMIC TUBES BY MICROWAVE SEEDING AND SOLVOTHERMAL SECONDARY GROWTH\*

### 4.1 Introduction

As mentioned in Chapter 1, following the well-acclaimed pioneering work by Bux et al.[47] and Pan and Lai et al.,[9] several groups reported polycrystalline ZIF-8 membranes supported on alumina disks exhibiting propylene/propane separation factors as high as ~200,[54, 56, 84, 96] Polycrystalline ZIF membranes with high separation performances have been supported mostly by planar ceramic (alumina) substrates.[39, 43, 47, 52, 54, 56-62, 84, 96]

For their practical applications, however, it is of critical importance to be able to package ZIF membranes into modules with large surface-area-to-volume ratios.[132-135] With a packing density of 30–500 m<sup>2</sup>/m<sup>3</sup> (only ~5–20 m<sup>2</sup> membrane area per module), clearly current planar substrates are not scalable.[136] Scalable supports investigated so far include ceramic tubes,[49, 63-69, 137] ceramic hollow fibers,[69-71] and polymeric hollow fibers.[72-78].

Nair group was the first to report polycrystalline ZIF-8 membranes on polymer hollow fibers via an interfacial fluidic method.[73, 135] Similar strategies also were used by other groups to grow ZIF-8 membranes on polymeric hollow

---

\*Reprinted with permission from "Propylene-Selective Thin Zeolitic Imidazolate Framework Membranes on Ceramic Tubes by Microwave Seeding and Solvothermal Secondary Growth" by Sun, Jingze, et al, 2018. Crystals, 8.10, 373, Copyright [2018] by MDPI.

fibers.[138-140] Chen et al.[77] and Li et al.[78] reported preparation of ultra-thin ZIF-8 membranes on TiO<sub>2</sub>-modified and ZnO-modified polymer hollow fibers, respectively. Jeong and co-workers have recently reported propylene-selective ZIF-8 membranes on polymer hollow fibers using the microwave seeding and secondary growth method.[76] Despite their early success and great potential, only a few of the ZIF-8 membranes supported on polymer hollow fibers either tested or showed decent propylene/propane separation performances. Furthermore, it is expected to be quite challenging for ZIF-8 membranes on polymer hollow fibers to break into the market in a foreseeable future, given the fact that there are no commercial polycrystalline membranes (e.g., zeolite membranes) supported on polymer hollow fibers. Most commercial polymeric hollow fibers are not as thermally, mechanically, and chemically stable as ceramic supports, limiting their applications under mild conditions. There are even fewer reports on the use of ceramic hollow fibers as supports for ZIF-8 membranes.[141] It is not likely that fragile ceramic hollow fibers can be used for commercial applications.

Ceramic tubes are practical and promising supports for ZIF-8 membranes for large-scale gas separation membrane applications because they are not only chemically and thermally stable but also mechanically robust while offering significantly-improved packing density compared with planar supports.[142] To the best of our knowledge, ceramic tubes are the only substrate used for commercial polycrystalline molecular-sieve membranes for pervaporation applications (e.g., ZEBREX<sup>TM</sup> of Mitsubishi Chemical, Tokyo, Japan).[143]

Carreon et al.[144] first synthesized polycrystalline ZIF-8 membrane on the internal surface of alumina tubes via the manual rubbing seeding method, showing CO<sub>2</sub>/CH<sub>4</sub> separation performance. Yamaguchi et al.[49] prepared ZIF-8 on ceramic tubes with counter-diffusion methods, exhibiting a propylene/propane separation factor of 59 with relatively low propylene permeance of 7.5 GPUs (gas permeation unit, 1 GPU = 3.35 × 10<sup>-10</sup> mol s<sup>-1</sup> Pa<sup>-1</sup> m<sup>-2</sup>). With interfacial control via two immiscible solvents, they were able to obtain higher propylene permeance of 36 GPUs, but a lower propylene/propane separation factor of 12.[63] Tanaka et al.[64, 145] prepared *in situ* ZIF-8 membranes on ceramic tubes via surface modification. The resulting membranes with the thickness of ~1 μm exhibited a propylene/propane separation factor of 36 and corresponding propylene permeance of 27 GPUs (permeability of ~6 Barrer, see Table 2-7). This barely met the minimum propylene permeability of 1 Barrer and minimum propylene/propane separation factor of 35 by Colling et al.[146] in order for membranes to be commercially-viable based on three-stage membrane processes to obtain 99.6% propylene purity with 40.5% of energy reduction. In general, secondary (or seeded) growth results in polycrystalline membranes with improved microstructures (i.e., better grain boundary and lower thickness) as compared with *in situ* growth, thereby showing better separation performances.

Here, we report the facile preparation of thin ZIF-8 membranes on scalable ceramic tubes using microwave seeding and secondary growth. High-quality ZIF-8 seed layers were readily formed on ceramic tubes. Furthermore, the unique counter-

diffusion and microwave heating enabled us to control the location of seed layers, that is, either on the bore side or on the shell side, consequently the location of the membrane. After secondary growth, the resulting tubular ZIF-8 membranes on the bore side of the tubes showed the average propylene/propane separation factor of ~80, indicating improved grain boundary structure. Furthermore, the membranes are one of the thinnest ZIF-8 membranes prepared on ceramic tubes, thereby showing propylene permeance of more than 60 GPU.

**Table 4-1. Typical ZIF-8 tubular membranes targeting propylene/propane separation**

Year	PI	Permeance of propylene ( $\times 10^{-10} \text{mol s}^{-1} \text{Pa}^{-1} \text{m}^{-2}$ )	Permeability Barrer	SF	Thickness $\mu\text{m}$	Membrane Position	Method	Ref.
2014	Sankar Nair	135	355	12	8.8	Internal	Interfacial fluidic processing	[72]
2015		220	460	65	7	Internal	Interfacial fluidic processing	[73]
2015		150	355	180	8	Internal	Interfacial fluidic	[74]
2014	Takeo Yamaguchi	25	597	59	80	External	Counter-diffusion	[49]
2014		220	2628	10	40	External	Counter-diffusion with interface control by two immisible solvents	[137]
2014		120	1075	7.2	30	External	Counter-diffusion with interface control by two immisible solvents	[63]
2017	Shunsuke Tanaka	100	30	36	1	Internal	Surface Modification with APTES	[64]

## **4.2 Materials and methods**

### **4.2.1 Chemicals**

Zinc nitrate hexahydrate (98%, Sigma-Aldrich, Saint Louis, MO, USA) was used as a metal source while 2-methylimidazole (99%, Sigma-Aldrich, Saint Louis, MO, USA) was used as an organic ligand source. Sodium formate (American Chemical Society, ACS reagents,  $\geq 99\%$ , Sigma-Aldrich, Saint Louis, MO, USA) was used as a modulator for microwave seeding process. Methanol (ACS, absolute, low acetone, 99.8+%, Alfa Aesar, Haverhill, MA, USA) was used as the solvent.

### **4.2.2 Tubular supports**

Symmetrical ceramic tubes (named NS-1 by the vendor) were purchased from Noritake Co. (Nagoya, Japan), with no further treatment. The inner diameter of the support is 10 mm. The estimated packing density is around  $700 \text{ m}^2/\text{m}^3$ . According to the manufacturer, these supports were made of high purity alpha-alumina, with a mean pore diameter of  $0.15 \text{ }\mu\text{m}$  and a mean porosity of 35–40%. The  $\text{N}_2$  permeance of the bare tube is  $9.5 \times 10^{-7} \text{ mol pa}^{-1} \text{ m}^{-2} \text{ s}^{-1}$ . The maximum load is 246 N and the radial crushing strength is higher than 40 MPa.

### **4.2.3 Microwave (MW) seeding procedures**

The microwave seeding and secondary growth procedures were adopted from a previously published paper [39] from our group with slight modifications. The ceramic tubes were wrapped with Teflon tapes on the shell side to limit the reaction to only the bore side. The ceramic tubes were then immersed in the zinc solution for 1 h. The zinc solution was prepared by dissolving 2.43 g of zinc nitrate hexahydrate into 40 mL of methanol. For each tube, 2.59 g 2-mIm and

0.125 g sodium formate were dissolved into 30 mL of methanol. After the soaking, soaked ceramic tubes were transferred into microwave-inert reaction chambers with the ligand solution in them. A 100-W microwave was immediately introduced for 90 s after the transferring. After cooling down for 30 min, the ceramic tubes were washed with 40 mL of fresh methanol for 1 day inside a beaker on a Big Bill Thermolyne shaker (M49125, produced by Thermal Fisher Scientific, MA, USA ). A similar seeding procedure was adopted to prepare seed layers on the shell sides of tubes. To limit the formation of seed layers on the shell side, both ends of tubes were sealed with epoxy resin.

#### **4.2.4 Secondary growth procedures**

The secondary growth solution was prepared following the recipe by Pan et al. [9] by dissolving 0.11 g of zinc nitrate hexahydrate and 2.27 g 2-mIm into 40 mL of D.I water. The tube was wrapped again with Teflon tapes and immersed into a Teflon-lined autoclave with the secondary growth solution in it. The secondary growth was carried out for 5 d inside a convective oven at 30 °C. After the secondary growth, with Teflon tapes removed, the tube was washed with fresh methanol for 60 h, followed by drying at 60 °C before permeation tests. The washing procedure is similar to the one previously mentioned. Similarly, the seed layers on the shell sides of tubes were secondarily grown into membranes by sealing both ends of the seeded tubes with epoxy resin.

#### **4.2.5 Acid treatment and the reuse of tubes**

Our tubular supports were reused repeatedly by immersing the tubes in 1 mol/L hydrochloride acids for 1 min under ultra-sonication and four more minutes without ultra-sonication, followed by extensive washing. The surface of

the tubes was then regenerated by thermal treatment at 1100 °C for 4 h. The tubes were further sonicated in methanol and washed with fresh methanol, and then dried completely before using again.

#### **4.2.6 Characterizations and permeation tests**

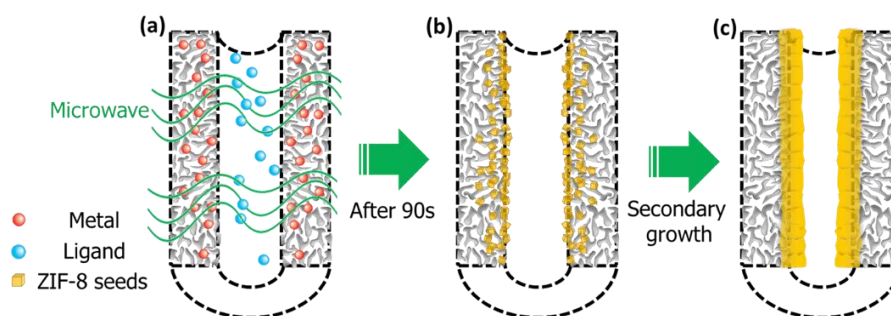
Powder X-ray diffraction (PXRD) patterns were collected using a Rigaku Miniflex II powder X-ray diffractometer (Rigaku Corporation, USA) with Cu-K $\alpha$  radiation ( $\lambda = 1.5406 \text{ \AA}$ ) with a step size of 0.020 degrees. Scanning electron micrographs (SEM) were collected using a JEOL (Tokyo, Japan) JSM-7500F operating at 2 keV acceleration voltage and working distances of 15 mm. The gas separation performances of ZIF-8 tubular membranes were tested using a home-made Wicke–Kallenbach setup [147] under atmospheric pressure. The 50:50 mixture of propylene and propane was supplied to a feed side, while the permeate side was swept by argon. The total flow rates of both sides were maintained at 100 mL/min. The gas compositions of the permeate side were analyzed using an Agilent (CA, USA) GC 7890A gas chromatography (equipped with HP-PLOT/Q column).

#### **4.3 Results and discussion**

Figure 4-1 displays a schematic illustration for our microwave seeding and secondary growth technique following the previously reported procedure.[39] To confine formation of seed layers on the bore sides of tubes, the shell sides of tubes were sealed using Teflon tape only during both the seeding and during later secondary growth. An alumina tube soaked with a zinc solution was immersed in a ligand solution, followed by microwave heating (Figure 4-1a). ZIF-8 crystals were then formed rapidly on the bore side surface (Figure 4-1b). Subsequent

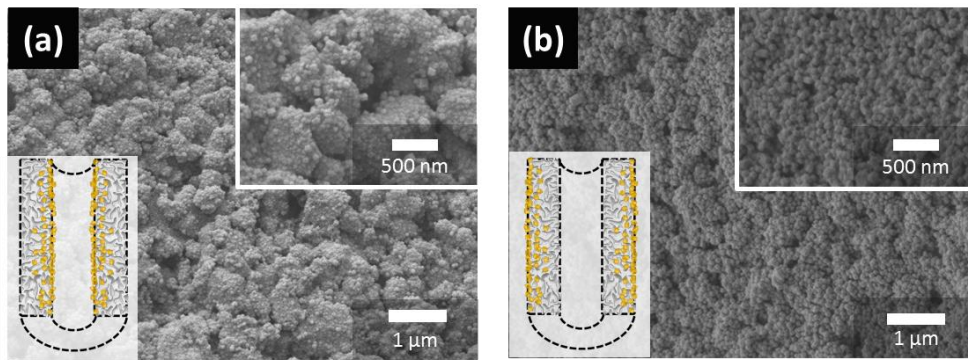


secondary growth of the seeded support led to the formation of polycrystalline ZIF-8 membranes (Figure 4-1c).

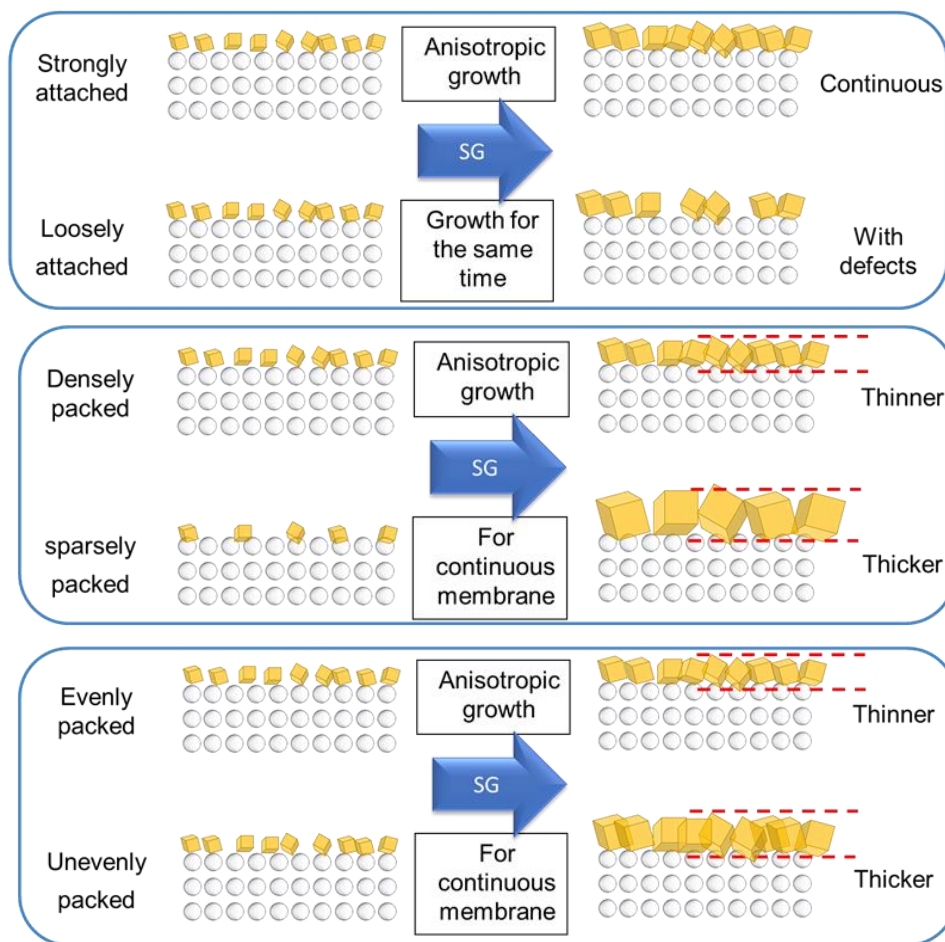


**Figure 4-1 A schematic illustration of (a) microwave seeding, (b) seeded tube, and (c) polycrystalline membrane after secondary growth.**

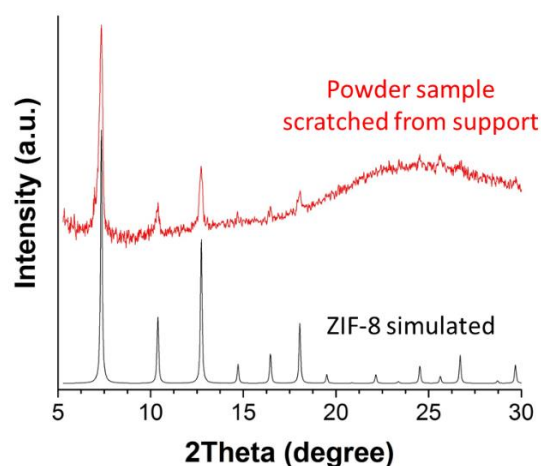
Figure 4-2 shows ZIF-8 seed layers formed on either the bore side or the shell side of alumina tubes. The surface of the support was covered by densely-packed ZIF-8 nanocrystals with an average size of ~50 nm (see Figure 4-2). These nanocrystals of ZIF-8 exhibit clear facets as well as narrow size distribution. As demonstrated in our earlier report,[39] the seed crystals appear to be strongly attached on the support surfaces. The seed layers with high packing density and uniform nanocrystals that are strongly attached to supports are expected to lead the formation of thin ZIF-8 membranes after secondary growth, as illustrated in Figure 4-3. It is worth mentioning here that the unique microwave heating in combination of counter-diffusion of zinc ions and ligands enables rapid formation of nanocrystals not only on the external surface but also inside porous supports (that is, inter-particle pores of supports) [39]. The seed crystals inside supports are expected to grow into grains interlocked between alumina grains, thereby increasing the mechanical strength of membranes after secondary growth.



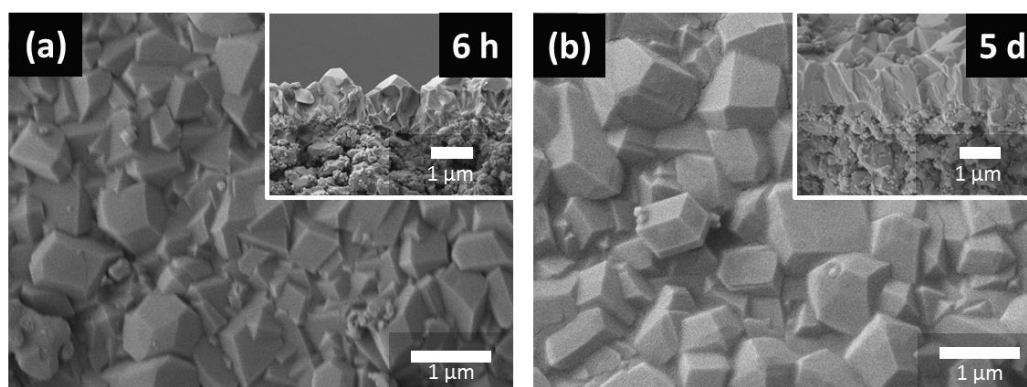
**Figure 4-2** Scanning electron micrographs (SEMs) of ZIF-8 seed layers on the (a) bore side and (b) shell side of alumina tubes after microwave seeding.



**Figure 4-3.** Schematic illustrations on common reasons for a low-quality seeding layer



**Figure 4-4. PXRD pattern of powder sample scratched from the inner surface of the tubular membrane and the simulated pattern.**



**Figure 4-5 SEMs of ZIF-8 membranes grown on the bore side of alumina tubes at secondary-growth times of 6 h (a) and 5 days (b). Cross-sectional images are shown as insets.**

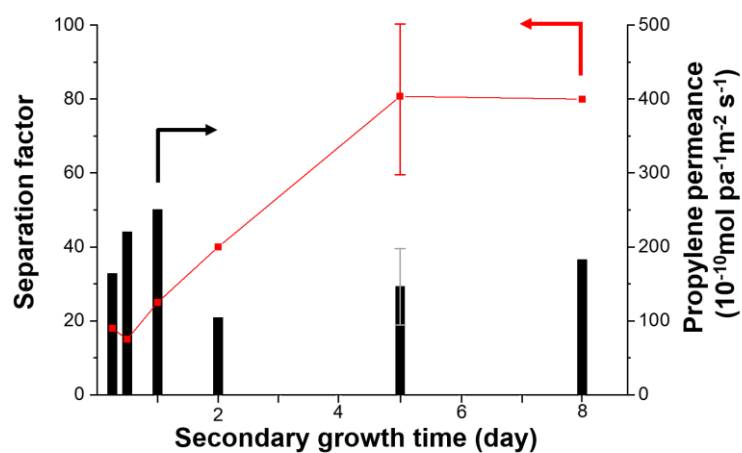
As shown in Figure 4-5a, ZIF-8 seed layers were grown into continuous, well-intergrown membranes after being subjected to the secondary growth in an aqueous solution at 30°C for 6 h. Because of the difficulty of taking X-ray diffraction on ZIF-8 membranes grown on the shell sides of tubes, the phase and crystallinity of the membranes were indirectly confirmed using the powder X-ray diffraction of powders scratched from the inner surface of the support (see Figure 4-4). The average thickness of the membranes was estimated to be ~1.2 μm (see the inset of Figure 4-5), which is among the thinnest ZIF-8 membranes grown on

either ceramic tubes/hollow fibers or polymer hollow fibers. Interestingly (see Table 4-1), many of the seeds deposited deeply inside the support did not grow further, likely because of the self-limiting nature of the growth. The propylene/propane separation performance of the membranes was tested in a Wicke–Kallenbach setup (Figure 4-8) with equal-molar propylene/propane mixture as a feed. The average propylene/propane separation factor of the membranes was ~20, which is much lower than those (~30–200) of our previous ZIF-8 membranes prepared similarly on alumina disks.[39, 56] This was attributed to the fact that with a tubular geometry and the ligand solution present in the inner cylinder space, mass transfer limitation might be generated. In other words, with planar supports, the concentration of ligand in the vicinity of support is maintained at a relatively high level because of the more effective convective mass transfer, which is not the case for tubular supports. After a series of experiments, we discovered that increasing the secondary growth time is most effective in improving tubular ZIF-8 membranes. Surprisingly, the thickness of the membranes remained unchanged even after extending the secondary growth time to 5 d (see Figure 4-5b). This can be explained based on the mass transfer limitation in the cylindrical geometry as described above, under which grains do not grow further, yet grain boundary structure may improve.

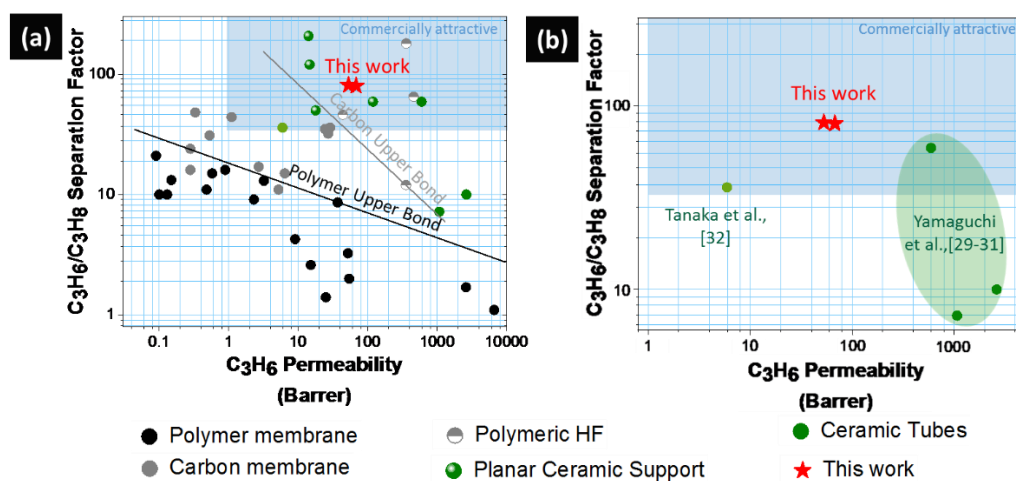
Figure 4-6 presents the propylene/propane binary separation performances of tubular ZIF-8 membranes as a function of the secondary growth time. As can be seen, the separation factor increased as the secondary growth time increased, while the propylene permeance underwent relatively little change. The secondary growth time of five days resulted in the separation factor of ~80, which is the

highest reported for tubular ZIF-8 membranes (see Table 3-1). A further extension of the secondary time to eight days was found to lead to no significant increase in the separation factor.

The propylene/propane separation performance of our ZIF-8 tubular membranes is compared with representative ZIF-8 polycrystalline membranes on various supports, as well as other membranes (see Figure 4-7a). Figure 4-7b compares our ZIF-8 membranes with propylene-selective ZIF-8 membranes on ceramic tubes. Table 4-2 summarizes and compares ZIF-8 membranes reported on scalable supports. As can be observed, our tubular membranes are significantly more propylene-selective as compared with previously reported tubular membranes, which can be attributed to the high-quality seed layers by microwave seeding, as well as to the better control over grain boundary structure by elongated secondary growth. A similar improvement can also be found for permeance (see Figure 4-9).



**Figure 4-6** Binary propylene/propane separation factors and propylene permeances of ZIF-8 tubular membranes with increasing secondary growth time. Additional samples (five membranes from three batches) were synthesized to generate the standard error bar.



**Figure 4-7.** Propylene/propane separation performance of our ZIF-8 tubular ZIF-8 membranes in comparison with (a) all other membranes and (b) other ZIF-8 membranes supported on ceramic tubes. HF—hollow fiber.

**Table 4-2. Propylene-selective zeolitic imidazolate framework (ZIF-8) membranes on polymeric hollow fibers and ceramic tubes. SF—separation factor.**

	Year	Group	Permeance ( $\times 10^{-10} \text{ mol s}^{-1} \text{ Pa}^{-1} \text{ m}^{-2}$ )	Permeability Barrer	SF	Thickness ( $\mu\text{m}$ )	Membrane Position	Method	Refer.
Polymeric hollow fibers	2014	Nair	135	355	12	8.8	Internal	Interfacial fluidic processing	[39]
	2015		220	460	65	7	Internal	Interfacial fluidic processing	[40]
	2015		150	355	180	8	Internal	Interfacial fluidic	[41]
	2017	Li & Zhang	215400	109	70	0.017	External	Gel-vapor deposition	[78]
	2018	Jeong	185	44	46	0.8	Internal	Microwave seeding and secondary growth	[76]
Ceramic capillary tubes	2014	Yamaguchi	25	597	59	80	External	Counter-diffusion	[29]
	2015		220	2628	10	40	External	Counter-diffusion with interface control by two immiscible solvents	[31]
	2015		120	1075	7.2	30	External	Counter-diffusion with interface control by two immiscible solvents	[30]
Ceramic tubes	2017	Tanaka	100	30	36	1	Internal	Surface modification with APTES	[32]

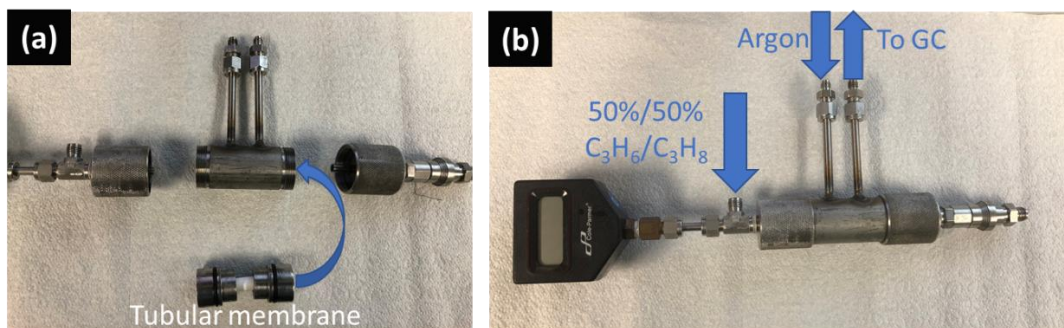


Figure 4-8 Optical images of (a) loading tubular membranes into the test module and (b) a schematic illustration of its gas connections (b).

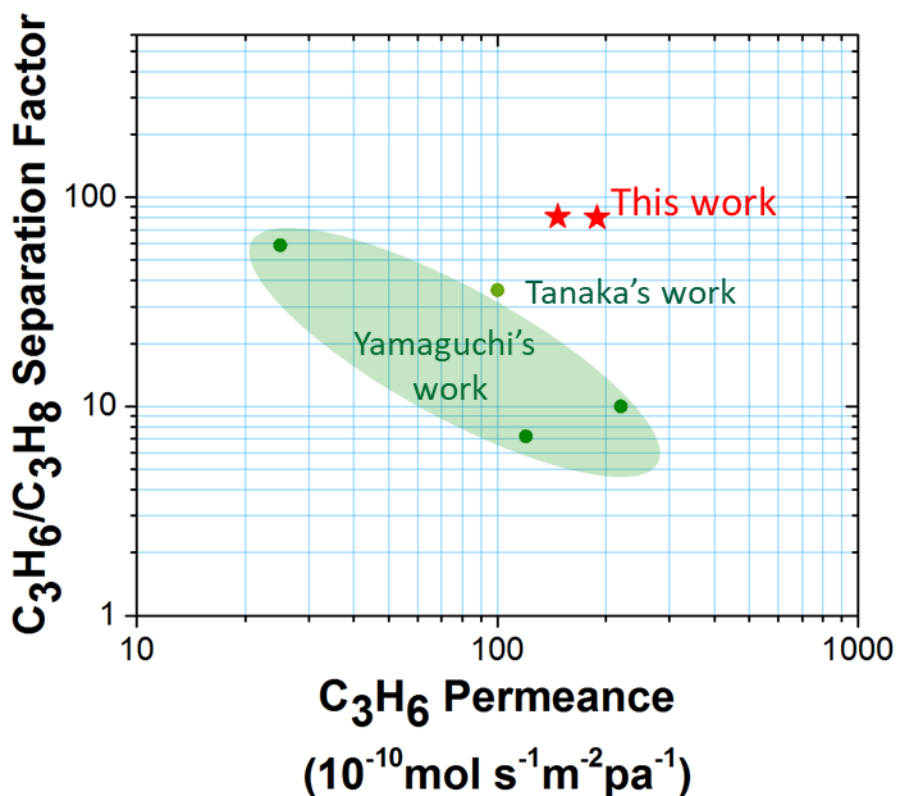


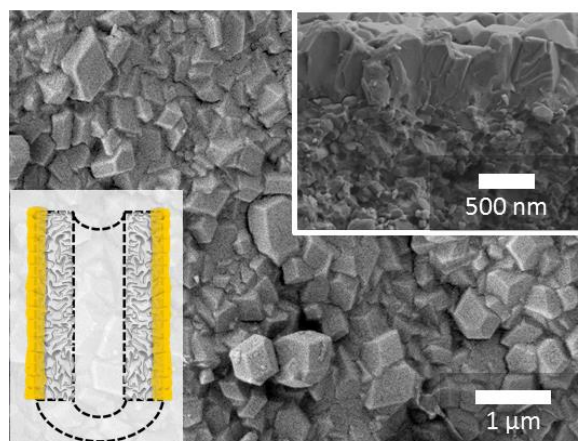
Figure 4-9. Permeance and separation factors of propylene/propane separation for ZIF-8 membrane on ceramic tubular supports.

As alumina tubes are relatively expensive, we attempted to find out whether or not tubes can be reused. ZIF-8 films on tubular supports were dissolved in a diluted hydrochloric acid solution. After extended washing in Deionized (DI) water,



the tubes were thermally treated at 1100°C for 4 h. The regenerated tubes were used to grow ZIF-8 membranes. In this way, tubular supports were regenerated several times. The performance of the resulting ZIF-8 membranes showed similar/better separation performances like those of the membranes on fresh tubes. All the separation data in Fig. 4-4 and 5 were generated by membranes on reused supports.

To further prove the versatility of our microwave seeding and secondary growth technique, membranes were prepared on the shell sides of supports. Although the membranes show similar morphology, they are quite a lot thicker (~1.8  $\mu\text{m}$ ) than the bore-side membranes (see Fig. 4-10). As opposed to growing on the bore side, growing on the shell side of a tube is similar to growing on a planar support in terms of mass transfer, consequently leading to thicker membranes.



**Figure 4-10. Top-view and cross-section (inserted) SEM micrographs of ZIF-8 membranes on the shell side of tubular supports. The secondary growth was performed at 30°C for 6 h.**

#### 4.4 Conclusions

Here, we synthesized high-quality ZIF-8 polycrystalline membranes on ceramic tubular supports with a thickness of  $\sim 1.2 \mu\text{m}$  using the microwave seeding and secondary growth technique. Compared with the currently-reported tubular ZIF-8 membranes, our tubular ZIF-8 membranes showed excellent propylene/propane separation factors of  $\sim 80$  and propylene permeance as high as 56 GPU. This improved separation performance of our membranes is likely caused by the fact that (1) the unique nature of microwave seeding led to rapid formation of high-quality seed layers which are strongly attached to supports; (2) the extended secondary growth time in a cylindrical support geometry enabled improvement in the grain boundary structure without further growing grains. The versatility of the current technique enabled the formation of ZIF-8 membranes on the shell-side of tubular supports. High-performance tubular ZIF membranes are expected to be a major step towards their practical application because of the high packing density of tubular configuration, along with the high chemical and mechanical stabilities of ceramic supports.

## 5. SYNTHESSES OF ULTRA-THIN ZEOLITIC IMIDAZOLATE FRAMEWORK (ZIF) MEMBRANE EXHIBITING HIGH EXCEPTIONAL PROPYLENE/PROPANE SEPARATION PERFORMANCES USING THE COMBINED SEEDING METHOD

### 5.1 Introduction

Due to their similarities in molecular sizes and chemical properties, propylene/propane separation is considered one of the most challenging tasks.[148] Among the ZIF family, ZIF-8[31] and ZIF-67,[32] formed by zinc/cobalt ions and 2-methylimidazoles showing SOD topology have shown propylene/propane separation performances well above traditional polymer upper bound,[9, 39, 84, 149] because of their effective aperture size of 4.0–4.2 Å[40]/3.8-4.0,[150, 151] respectively. However, just as Micheal Tsapatsis pointed out for zeolite membranes,[79] high membrane manufacturing cost hinders the further development and implementations of MOF/ZIF membranes.[152] The productivity of current MOF/ZIF membranes has to be significantly improved to overcome the prohibitively long payback times.

According to the equation  $Q_i = -\phi_i \cdot (\Delta p_i) \cdot A \cdot l^{-1}$ , reducing membrane thicknesses can greatly increase productivity, where  $\phi_i$ ,  $\Delta p_i$ ,  $l$  and  $A$  are the permeability of gas  $i$ , the partial pressure difference of gas  $i$  between feed and permeate sides, membrane thickness, and membrane area, respectively. Various cutting-edge methods have been employed for reducing the thickness of polycrystalline membranes. Reported by Zhang et al.,[153] an ultrathin ZIF-8 membrane of 550 nm was fabricated via a spatially confined contra-diffusion

process. He et al.[154, 155] demonstrated the syntheses of ultrathin highly intergrown ZIF-8 membranes (500 nm) on various supports using electrophoretic deposition methods. Hou et al.[77] used a facile immersion technique to synthesize ultrathin ZIF-8 membrane (400 nm). Hu et al.[156] prepared a defect-free ZIF-8/graphene oxide (GO) membrane (100 nm) using two-dimensional (2D) ZIF-8/GO hybrid nanosheets as seeds. Li et al.[78] successfully synthesized nanometer-thick ZIF-8 membrane (17 nm) through gel-vapor deposition. Nevertheless, current synthesis methods of ultrathin membranes still cannot be considered as mission accomplished, due to compromised selectivities ( $<50, C_3=/C_3$ ), the use of pricy chemicals/materials (e.g. polydopamine, (3-Aminopropyl)triethoxysilane, anodized-alumina supports (AAO)), or unconventional synthesis methods. As a result, a more universal, scalable synthesis method of well-intergrown ultrathin membrane is highly desired. It should be noted that as we are preparing our manuscript, we learned about the paralyzed membrane on AAO supports prepared by Caro et al.,[157] showing both promising propylene-propane selectivity as well as permeance.

These aforementioned membrane synthesis methods can be assorted into two categories, in-situ methods, and seeded methods. Benefiting from the decoupling of nucleation and growth, seeded growth generally offers better control of the microstructure of the membrane and stronger anchored on porous supports over the in-situ method. Among seeding methods, traditional microwave seeding method [39, 47, 107, 158, 159] can provide seeding crystals not only strongly attached but also densely and evenly distributed. However, it results in seeds of 70-120 nm in size, and

therefore membranes as thick as 1.5  $\mu\text{m}$ ,[39] which can be solved by denser and smaller seeds and therefore significantly decreased membrane thickness.[160] And introducing amines(e.g. triethylamine, hereafter TEA)[161-163] into the system can greatly reduce the size of ZIF crystals by promoting the deprotonating process of organic linkers. With the help of TEA, sub-micron ZIF-90,[164] nanosized ZIF-67 particles,[160] have been successfully synthesized. TEA has also been proved effective in controlling facet growth and crystal morphology.[153, 160, 164-166]

The formation of densely-packed seeding nanoparticles also provides an unprecedented opportunity for phase-pure ZIF-67 synthesis. ZIF-67 has been proved to possess smaller effective aperture sizes predicted both experimentally,[32, 96] and simulatively,[150, 151] therefore potentially better selectivity than ZIF-8, yet never confirmed by membrane separation. Syntheses of phase-pure ZIF-67 membranes have always been problematic, especially on alumina-based supports. Kwon et al.[96] has successfully grown the first ZIF-67 membrane heteroepitaxially over ZIF-8 on  $\alpha\text{-Al}_2\text{O}_3$  supports and shown remarkable propylene/propane selectivity factor of  $\sim 200$  and the highest permeance of  $\sim 110$  GPU. Despite this, they failed to grow phase-pure ZIF-67 membrane on substrate, because of unknown disk-shape impurities.[96] On the other hand, phase-pure ZIF-67 membrane has been synthesized by various methods,[112, 167-172] but none have reported any propylene/propane selectivities.

Here, we report an ultrathin phase pure ZIF-67 membrane synthesized on utilitarian porous  $\alpha\text{-Al}_2\text{O}_3$  support via a novel facile seeding method by combining

microwave seeding (using TEA) with electrophoresis deposition (ENACT), which could reduce the size of seeding crystals to ~ 20 nm while smoothing the surface of the support as well as providing surface anchoring. After solvothermal secondary growth, our membrane showed a selectivity of 67 and propylene permeance of ~90 GPUs with a thickness of only 300-500 nm, which is the first phase-pure ZIF-67 with propylene/propane selectivities. In addition, the selectivity could be further enhanced to ~290 by tertiary growth. This combined seeding method was also proved to be successful in synthesizing ultrathin ZIF-8 membranes.

## **5.2 Materials and methods**

### **5.2.1 Chemicals**

To prepare disk-shaped alumina substrate,  $\alpha$ -Al<sub>2</sub>O<sub>3</sub> powder (CR6, Baikowski) was pressed with polyvinyl alcohol (PVA 500, Duksan) solution as a binder. Cobalt nitrate hexahydrate (Co(NO<sub>3</sub>)<sub>2</sub> • 6H<sub>2</sub>O, 98%, Sigma-Aldrich) and 2-methylimidazole (2-mIm, hereafter) (C<sub>4</sub>H<sub>6</sub>N<sub>2</sub>, 99%, Sigma-Aldrich) were used as metal source and organic ligand, respectively and triethylamine (C<sub>6</sub>H<sub>15</sub>N, 99%, Fisher Chemical) as a deprotonating agent. The deionized water or methanol (CH<sub>3</sub>OH, >99%, Alfa Aesar) were used as solvents. For further PSLE experiments, 2-imidazolecarboxaldehyde (C<sub>4</sub>H<sub>4</sub>N<sub>2</sub>O, 97%, Alfa Aesar, hereafter ICA) was used as organic ligand. All chemicals were used as received without any further purification.

### **5.2.2 Preparation of $\alpha$ -Al<sub>2</sub>O<sub>3</sub> substrate**

Disk-shaped alumina substrates (porosity = ~ 46 %, diameter = 22 mm, and thickness = 2 mm) with an average pore diameter of 200 nm were prepared by previously reported method.[96] 10 g  $\alpha$ -Al<sub>2</sub>O<sub>3</sub> powder was mixed with 1 ml of PVA binder solution followed by continuous grinding until aggregated powder was completely shattered. 2.1 g grounded powder was molded into a disk shape by exerting 17 MPa of pressure for 1 min then sintered at 1100 °C for 2 h. The sintered disks were polished on one side using a sandpaper (grid #1200) to reduce the surface roughness of the substrates, followed by sonication for 1 min in methanol to remove debris. Subsequently the supports were dried in an oven at 120 °C for 1 h before usage.

### **5.2.3 Preparation of ZIF-67 seed layer using microwave-assisted seeding**

Solutions for ZIF-67 microwave seeds were prepared following previously reported methods.[160] Briefly, the metal solution was prepared by dissolving 472 mg cobalt nitrate hexahydrate in 40 ml methanol and 532 mg of 2-mIm in 40 ml methanol with 48  $\mu$ l TEA as a ligand solution.  $\alpha$ -Al<sub>2</sub>O<sub>3</sub> substrate made previously was immersed in metal solution held vertically using a self-made Teflon holder, after 1 h of soaking, the saturated substrate was quickly moved into ligand solution in a microwave-transparent tube and tube was immediately insert into microwave oven for 1.5 min under 100 W power capacity, followed by 30 min cooling down in room temperature. The support was then washed in 40 ml methanol under gentle rocking

for 12 h then dried in a convection oven at 60 °C for another 4 h before further experiments.

#### **5.2.4 ENACT seeding process upon microwave-seeded substrate**

The ENACT seeding was conducted following previously reported methods with few modifications.[155] The solution for ENACT process was prepared by dissolving 0.44 g cobalt nitrate hexahydrate and 11.08 g 2-mIm in a mixture of 5 ml of methanol and 35 ml of D.I. water. Briefly, the microwave-seeded  $\alpha$ -Al<sub>2</sub>O<sub>3</sub> substrate was attached to a copper electrode (the cathode) while another copper electrode as the anode. Both electrodes were connected to an exterior power source which can provide stable direct current. After pouring the metal solution into the ligand solution and continue mixing for 30 s under continuous stirring, electrodes and the seeded substrate were soaked into the mixed solution followed by a 3-min aging process. A constant voltage of 1 V was then applied between the electrodes for another 4 min with the distance between electrode equal to 1 cm. After the ENACT process, the support was washed in 40 ml of methanol for 12 h to remove unwanted residue then dried in a convection oven at 60 °C for 4 h before the secondary growth.

#### **5.2.5 Secondary growth (SG, hereafter)**

The secondary growth solution was prepared by dissolving 2.27 g of 2-mIm and 0.11 g of cobalt nitrate hexahydrate into a mixture of 5 ml methanol and 35 ml D.I. water. Previously prepared alumina substrate was held vertically using Teflon holder then put in a Teflon-lined autoclave with the secondary growth solution in it. The reaction was carried out in a convection oven with temperature programming



functions. After the start of the secondary growth, the autoclave was first preheated to 40 °C for 10 min then the oven was gradually heated up to 70 °C in 1.5 h and maintained constant for 24 h. After the secondary growth, the autoclave was cooled down to room temperature. And then the membrane was washed in 40 ml methanol for 1 day and dried in convection oven at 60 °C for 4 h before further characterizations and permeation tests.

### **5.2.6 Tertiary growth (TG, hereafter)**

First, the ZIF-67 membrane after SG was treated in the ligand solution (prepare by dissolving 4.54 g 2-mIm into 5 ml of methanol and 35 ml of D.I. water) at 120 °C for 4 h. Then the treated membrane was washed in methanol overnight and dried in 60 °C for 4 h before tertiary growth. The procedure for tertiary growth was the same as secondary growth. As-prepared TG ZIF-67 was washed and dried the same way as mentioned above.

### **5.2.7 Characterizations and permeation tests**

Scanning electron micrographs were collected using a JEOL JSM-7500F system operated with an acceleration voltage of 2 keV and a working distance of 15 mm. Samples were coated by platinum with a thickness of 5 nm prior to SEM. Powder X-ray diffraction (PXRD) patterns were collected using a Rigaku Miniflex II powder diffractometer with Cu-K $\alpha$  radiation ( $\lambda = 1.5406 \text{ \AA}$ ). The permeation test was carried out on a home-built Wicke-Kallenbach setup with an argon flow of 100 ml/min as sweep gas on the permeate side and 100 ml/min 50:50 propylene/propane gas mixture on the feed side. The feed side composition was characterized using an

Agilent GC 7890A gas chromatography (equipped with HP-PLOT/Q column). NICOLET IR100 FT-IR spectrometer was used for characterizing PSLE experiments.

### 5.3 Results and discussion

The crystallographically-defined aperture size of ZIF-8 is 3.4 Å.[31] However, a significant diffusion of propylene (4.0 Å) and (4.2 Å) has been observed inside ZIF-8.[40] Such a phenomenon was caused by the flexibility of its framework. Forming only two coordination bonds with nearby zinc ions, the linkers of ZIF-8 are gematrically flexible and constantly in a thermal-driven flapping motion which is commonly analogized as “saloon doors”. [173] Comparing to Zn-N coordination bonds in ZIF-8, Co-N bonds are mechanically stronger, therefore ZIF-67 been predicted to possess more rigid structure with a smaller oscillation of the gate-opening thereby smaller aperture size and higher selectivities as membranes.[150] Therefore, ZIF-67 is potentially very promising as membrane material for propylene/propane separations, however, not yet proven by membrane separations.

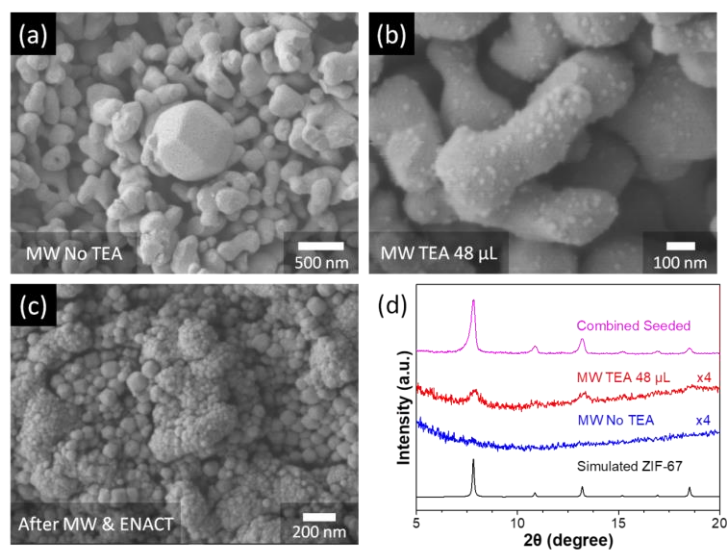
Kwon et al.[96] had to grow ZIF-67 membrane heteroepitaxially over ZIF-8 seed layers on  $\alpha$ -Al<sub>2</sub>O<sub>3</sub>, because the unsuccessful direct syntheses of ZIF-67 membrane led to disk-shaped impurities, which was later identified as layered double hydroxides (LDH, hereafter).[172] As summarized in Table S1, multiple methods have been exploited for synthesizing ZIF-67 membranes. Wang et al.[170] synthesized pure ZIF-67 membrane by introducing Co(OH)<sub>2</sub> precursor by electrodeposition, but no propylene/propane separation was reported. Jiang et

al.[167] provided another option by synthesizing nanoporous ZIF-67 embedded polymers on Teflon plates via solution evaporation method. By using an APTES-treated tubular  $\alpha$ -Al<sub>2</sub>O<sub>3</sub> support, Zhang et al.[168] coated the support with Co-NWAs, upon which phase-pure ZIF-67 membrane was synthesized. Furthermore, the membrane performance was improved by heteroepitaxially growing ZIF-67 membrane on top of ZnO nanorods on a tubular  $\alpha$ -Al<sub>2</sub>O<sub>3</sub> support.[168] Pan et al.[112] has successfully synthesized zinc/cobalt mixed-metal membranes which are capable of separating propylene/propane with selectivity of 50.5 when 90% of cobalt been substituted by zinc. However, to the best of our knowledge, no phase-pure ZIF-67 membrane with any propylene/propane selectivity have been reported, and because of its great potential, ZIF-67 was selected as a demonstration for our combined seeding and solvothermal secondary growth method.

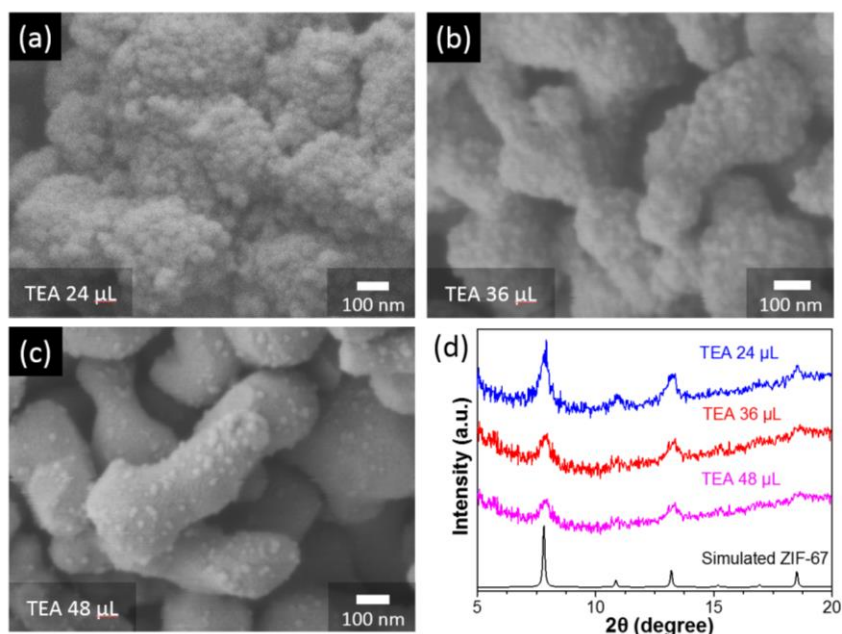
As discussed previously, TEA is a strong proton receiver can promote the deprotonation of linkers. Inspired by previous works, TEA was used during microwave seeding to promote the deprotonation of the 2-mIm and accelerate the nucleation rate of ZIF-67, therefore reducing the size of seeding crystals previous work related to TEA. Zhang et al.[160] has studied the effect of TEA on ZIF-67 crystal size in detail and they found that the particle size decreased from 900 nm to 20 nm when increased the use of TEA from 2  $\mu$ L to 12  $\mu$ L. Liguori et al.[164] also reported sub-micron ZIF-90 in methanol solution with the presence of TEA. Wang et al.[165] controlled facet growth of MOF-5 and tuned its size and shape during its

crystallization with TEA as an additional base. Yang et al.[112] investigated the effect of TEA on morphology and size of SUMOF-3 microcrystals.

As shown in Fig.5-1(a-b), the size of seeding crystals was significantly reduced from ~600 nm to ~20 nm with the presence of TEA and seeding density was drastically increased as well as XRD intensities (further optimization of microwave seeding process optimization is included in Fig 5-2). However, these seed crystals naturally grow on the alumina substrate and they have to further grow across the voids between support particles to form a continuous membrane, which may conversely increase membrane thickness. Therefore, additional seeding crystals are demanded to fill these voids.



**Figure 5-1. Microwave seeded support with (a) and without (b) TEA. After microwave seeding (with TEA) and ENACT seeding process (c) and their corresponding XRD patterns (d).**

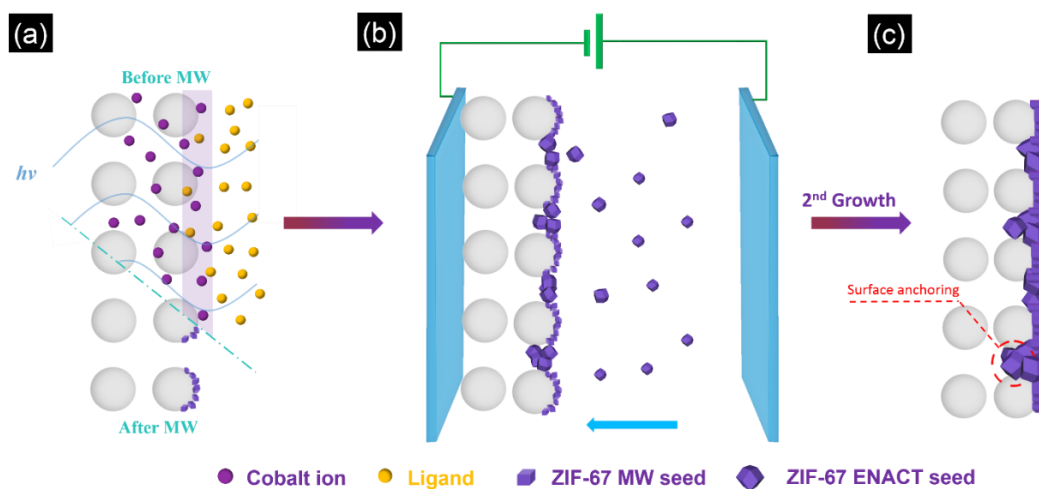


**Figure 5-2. Optimization of TEA content during microwave seeding. Top-view SEM images of microwave seeded support with different TEA content (a-c) and their corresponding XRD patterns (d).**

Reported by Kumar et al.,[154, 155] ENACT can provide precise control over the crystal sizes for surface deposition on various supports, by varying the aging time. Induced by electrophoresis of nuclei which is caused by the interaction between the surface charges (characterized by zeta potential) as well as the external electrical field, a layer of crystals with size of 70~80 nm will be deposited on seeded support. Except for changing the aging time after mixing the ligand and metal solution, electricity voltage and deposition time also need to be controlled to make sure that proper amount of seeds with desired size are deposited.

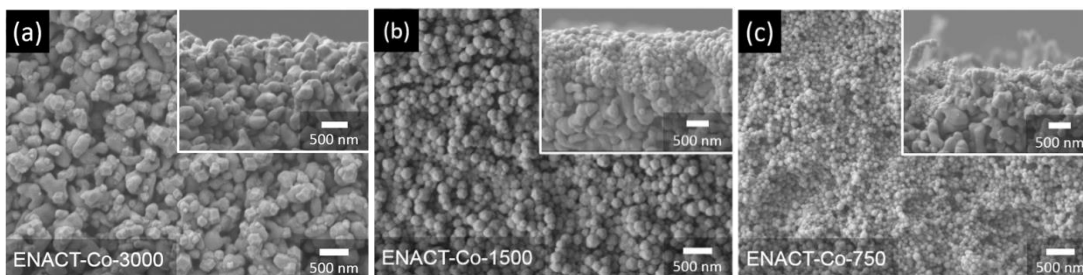
As can be seen in Fig. 5-1c, a bimodal distribution of crystals was generated after ENACT seeding. It is very likely that smaller crystals with a size of ~30 nm grew from MW seeded during ENACT while the larger crystals are from the

homogeneously nucleated crystals from the ENACT solution and deposited onto the support because of the static electrical field induced externally. As such, not only the surface of the support would be smoothed by crystals induced by ENACT, each crystal will also be able to grow a short extension and therefore reduce the thickness of the membrane. The optimization process of ENACT can be found in Fig. 5-4.

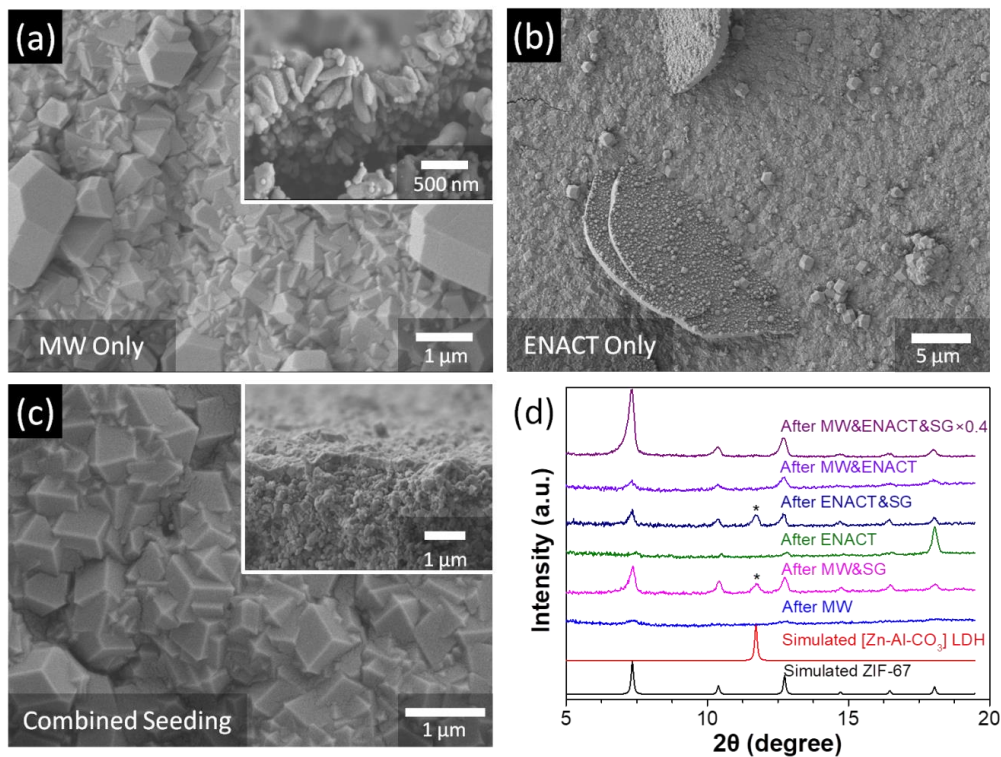


**Figure 5-3. Schematic illustration of combined seeding process: (a) microwave-assisted seeding step, (b) ENACT seeding step, and (c) secondary growth.**

A schematic demonstration for such a combined seeding process is presented in Fig. 5-3. To form densely-packed and evenly-distributed seed layers smoothing the surface of  $\alpha$ -Al<sub>2</sub>O<sub>3</sub> support, nanosize ZIF-67 seeds were first deposited on the outer surface of the support with the presence of TEA as shown in Fig. 5-3a. While to further fill the gaps between  $\alpha$ -Al<sub>2</sub>O<sub>3</sub> particles, larger ZIF-67 particle introduced by ENACT seeding was deposited between the microwave seeds. In Fig. 5-3c, after secondary growth process, a well-intergrown ZIF-67 membrane with desired thickness was synthesized on top of the smoothed surface.



**Figure 5-4. Optimization of ENACT content during microwave seeding. Top-view SEM images of microwave seeded support with different metal and ligand concentration (a-c).**



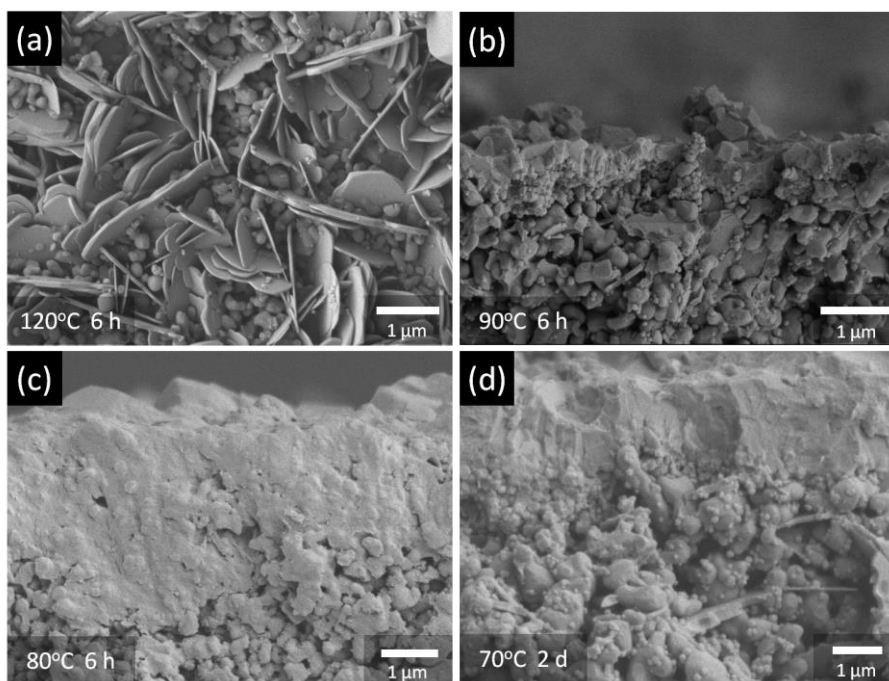
**Figure 5-5. Comparison of SEM images for ZIF-67 membranes after secondary growth with different seeding methods: (a) only microwave seeding, (b) only ENACT seeding, (c) combined seeding, and (d) their corresponding XRD patterns. MW stands for microwave seeding here.**

The necessity of combined seeding was further demonstrated in Fig. 5-5.

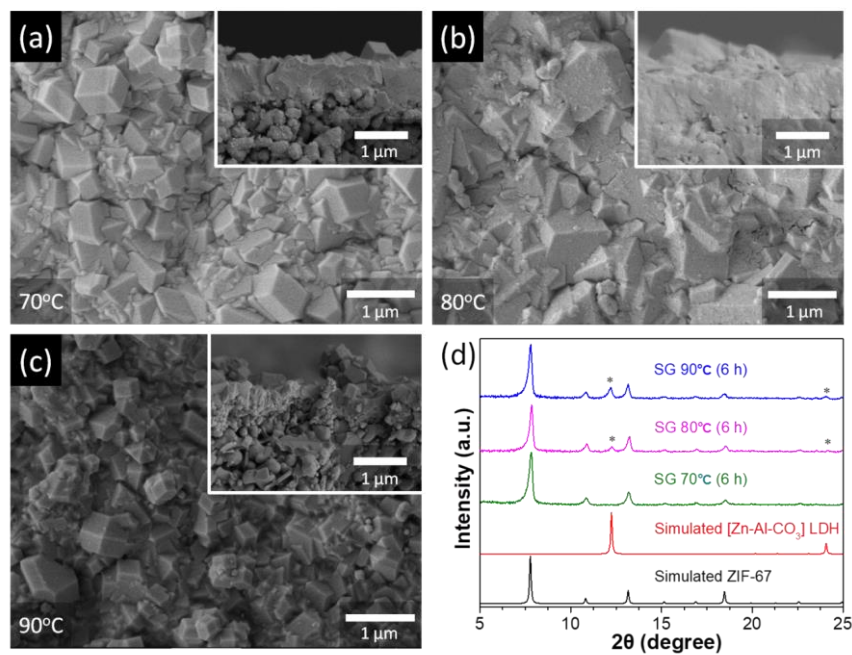
Secondary growth was conducted for supports undergoing different seeding

procedures (only microwave, only ENACT, and combined seeding). As shown in Fig. 5-5a, a continuous layer of ZIF-67 was formed for support seeded only by microwave while exfoliations between the ZIF-67 crystals and the support can also be observed, possibly due to the fact that microwave seeds are concentrated on the very surface of the support particles and therefore lack surface anchoring to counter the stress induced by crystal growth. For support seeded only by ENACT, however, disk-shaped impurity was observed, which was very similar to previously reported ones, possibly due to the fact that the surface of support was not fully covered.[96] Therefore,  $\text{Al}^{3+}$  ions from the alumina support will probably partially substitute  $\text{Co}^{2+}$  ions in the  $\text{Co}(\text{OH})_2$  structure which exists in the secondary growth solution and form double layer hydroxides structure (LDHs),[172] with the presence of dissolved  $\text{CO}_2$  in the solution, the LDHs could further crystallize with carbonate ions.[172, 174] Since [Zn-Al] LDHs has been investigated by many researchers, considering the structure similarity of  $\text{Zn}(\text{OH})_x$  and  $\text{Co}(\text{OH})_x$ , the forming of LDHs structure was confirmed by PXRD pattern in Fig. 5-5d. However, such impurity was not observed in Fig. 5-5c. Since this impurity requires alumina source and seems to root from the support particles (see Fig. 5-5c inserted, more details in Fig. 5-6), microwave seed together with ENACT seed layer provided a complete coverage over the top layer of the support particles, which in turn, prevent the formation of [Co-Al] LDH impurities.





**Figure 5-6. Impurity under different secondary growth conditions: (a) 120°C for 6 h (top view), (b) 90°C for 6 h, (c) 80°C for 6 h, and (d) 70°C for 2 d.**

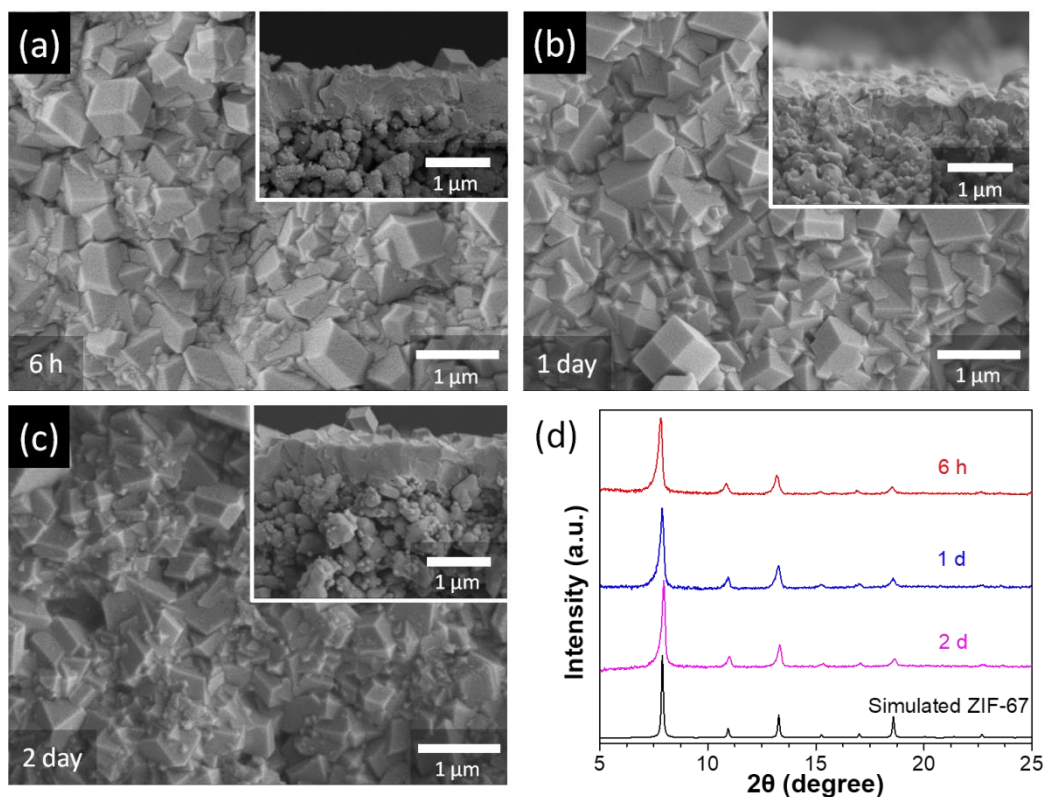


**Figure 5-7. SEM images of ZIF-67 membrane going through same secondary growth procedure at (a) 90°C, (b) 80°C and (c) 70°C and their corresponding XRD patterns (d).**

**Table 5-1. Summary of separation performances for different secondary growth time and temperature**

Temperature, Secondary Growth time	Propylene Permeance (GPU)	Selectivity Factor
90°C, 6 h	79.74	21
80°C, 6 h	47.24	55
70°C, 6 h	72.62	7
70°C, 1 d	73.54	51
70°C, 2 d	81.48	67

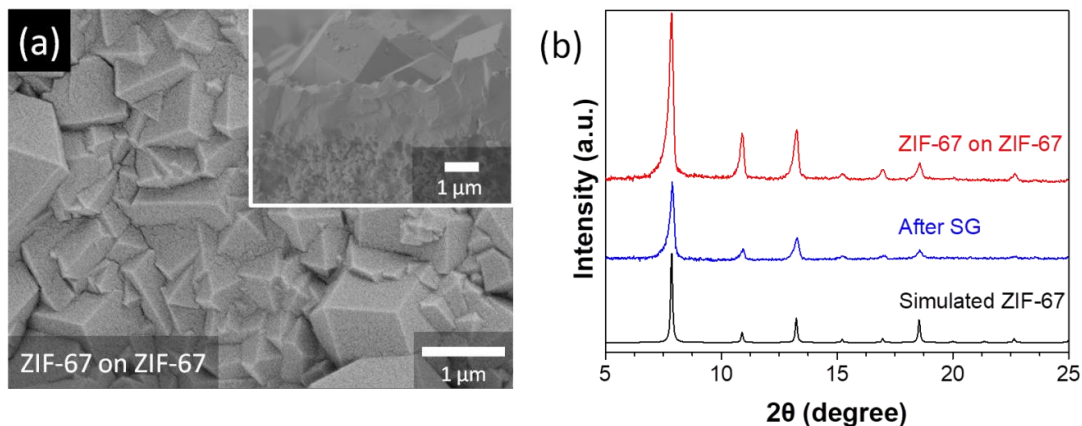
All the secondary growth was carried out at 120°C for samples mentioned above. However, additional repeated experiments often lead to the formation of [Co-Al] LDH impurities, possible due to the difference of seeding qualities, which can simply be solved by reducing the secondary growth temperature. As shown in Fig. 5-7d, as the second growth temperature decreases from 90°C to 70°C, the impurity peak completely disappeared. On the other hand, as shown in Table 4-1, the C3=/C3 selectivity decreased dramatically to only 7 after secondary growth at 70°C, which might be attributed to the fact that the growth of ZIF-67 generally requires a high temperature for overcoming the activation energy barrier, comparing to ZIF-8 which can be readily formed at room temperature.



**Figure 5-8. SEM images for ZIF-67 membranes after secondary growth at 70°C with time of (a) 6 h, (b) 1 day, and (c) 2 days as well as (d) their corresponding XRD patterns.**

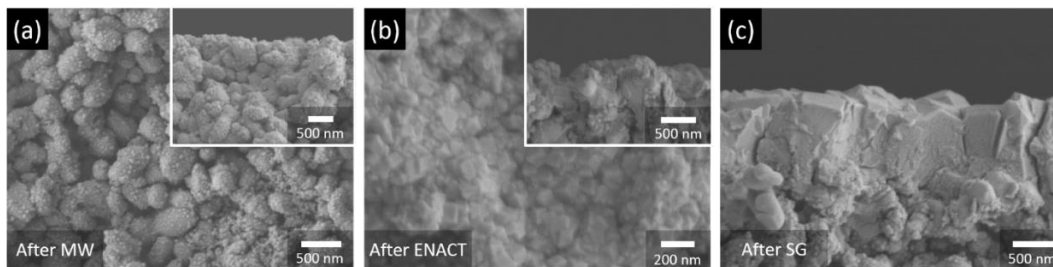
By further extending the reaction time, the morphology of our ZIF-67 membranes can be improved as well as their selectivity towards propylene and propane, as shown in Fig. 5-8 and Table 5-1. With a thickness of only 500 nm, our two-day membrane showed a selectivity of 67 as well as permeance of 273 mol/(m<sup>2</sup> pa s). This has been one of the thinnest ZIF membrane reported on scalable supports like our porous alumina support. It is also the first phase-pure ZIF-67 membrane with propylene/propane selectivity. The selectivity of the membrane can be further increased by going through the secondary growth again (named tertiary growth, TG

hereafter). As the thickness of the membrane was increased to about 2  $\mu\text{m}$ , the selectivity of the membrane was also enhanced to 297, for our 1-day sample going through a tertiary growth of another 1 day, as presented in Fig. 5-9.



**Figure 5-9. SEM images(a) and XRD(b) pattern of the ZIF-67 membrane after tertiary growth.**

Such a combined seeding and secondary growth process can also be used in the synthesis of other ZIFs. We applied the same technique by adding TEA during the microwave seeding followed by ENACT seeding and then secondary growth. In Fig. 5-10, as can be seen, ZIF-8 showed similar results as ZIF-67 described above. It also showed improved permeance comparing to previously reported result, partially due to its reduced thickness of  $\sim 700$  nm.



**Figure 5-10. SEM images of ZIF-8 after microwave seeding (a), ENACT (b) and secondary growth (c)**

## 6. ADDITIONAL WORKS: CONTINUOUS SYNTHESIS OF HIGH-QUALITY METAL-ORGANIC FRAMEWORK HKUST-1 CRYSTALS AND COMPOSITES VIA AEROSOL-ASSISTED SYNTHESIS\*

### 6.1 Introduction

Currently, MOFs are synthesized predominantly by batch processes which suffer from inherently low efficiencies, substantial chemical wastes, high costs, and difficulties in scaling up.[175] Furthermore, advanced and/or practical applications of this emerging class of nanoporous framework materials often require cost-effective construction of materials with complex hierarchical microstructures and multi-functions, some of which cannot be easily obtained with conventional batch crystallization processes. Continuous processes reported so far for MOF synthesis include continuous flow,[176] microfluidic,[177] microwave-assisted continuous flow,[178] droplet reactor,[179] jet-mixing[180] and others.[181] In particular, spray-drying [182-185] is of particular practical interest since the technique is not only well-studied for materials synthesis [186, 187] but also used to readily create composites primarily due to its unique continuous and confined synthesis environment.[188]

Maspoch et al.[188] reported the first spray-drying synthesis of HKUST-1 (also known as  $\text{Cu}_3(\text{BTC})_2$ ,  $[\text{Cu}_3(\text{TMA})_2(\text{H}_2\text{O})_3]_n$ )[189] and other MOFs. They observed the formation of HKUST-1 hollow spheres assembled of nanocrystals.

---

\*Reprinted with permission from “Continuous synthesis of high quality metal–organic framework HKUST-1 crystals and composites via aerosol-assisted synthesis” by Sun, Jingze, et al, 2018. Polyhedron, 153, 226-233, Copyright [2018] by Elsevier

Unfortunately, they also observed the formation of amorphous phase in their product. Furthermore, due to the extremely rapid crystallization, however, quality of spray-dried HKUST-1 nanoparticles was not comparable to those by conventional batch processes (that is, no clear crystal facets).[190] As pointed out by MasPOCH et al. Garzón-Tovar, Cano-Sarabia [191] spray-drying possesses inherently rapid reaction kinetics and fast solvent evaporation, which lead to formation of HKUST-1 nanoparticles and their assemblies into hollow spheres.

On the other hand, though similar, aerosol-assisted synthesis (AAS) offers several advantages over spray-drying such as better control over residence time, solvent evaporation, and temperature, potentially enabling the formation of better-quality MOF crystals and their composites. Boissiere et al.[190] first reported a continuous synthesis of HKUST-1 using AAS and observed similar hollow spherical structure. Recently, Kubo et al.[175] performed systematic investigation in the effects of copper salts and process conditions on the aerosol-assisted synthesis of HKUST-1. They found copper acetate yielded HKUST-1 nanoparticles with highest BET surface area possibly due to its modulating effect.[192] Unfortunately, they also observed similar hollow spheres of HKUST-1 nanoparticles and formation of amorphous phase. It is noted that spray-drying/AAS led to a 20 % ~ 50 % loss of specific surface areas of MOFs including HKUST-1 as compared to batch synthesis, strongly indicating relatively poor crystallinities and possible presence of amorphous phase. Other factors that could potentially lower specific surface areas include

incomplete washing/activation and potential loss in the crystallinities upon activation.

Here, we report high-quality microcrystals of HKUST-1 and its unique microstructures using an aerosol-assisted synthesis. In order to produce HKUST-1 crystals with well-developed facets and high specific surface areas, it was of critical importance to stabilize precursor solutions prior to subjecting to AAS and to increase residence time of droplets by decreasing solvent evaporation rate. A systematic study was performed to examine the effect of various common solvents on the stability of precursor solutions. With the optimized solvent, we found optimal furnace temperature at which highly crystalline HKUST-1 crystals. Furthermore, unique microstructures of HKUST-1 were prepared by *in-situ* introducing either inorganic alumina nanoparticles or organic polyethersulfone (PES), resulting in a significant increase in external surface areas.

## **6.2 Materials and methods**

### **6.2.1 Chemicals**

Copper(II) nitrate semi(pentahydrate) (Aldrich,  $\geq 99.99\%$ , trace metals basis, CuN hereafter) and 1,3,5-benzenetricarboxylic acid (Alfa Aesar, 98%, BTC hereafter) were used as metal and linker sources, respectively. DI water, methanol (Alfa Aesar, ACS, absolute low acetone, 99.8+%), ethanol (Alfa Aesar, alcohol reagent anhydrous denatured, ACS, 94-96%), dimethyl sulfoxide (Sigma-Aldrich, ACS reagent  $\geq 99.9\%$ ), and N,N-dimethylformamide (DMF, Sigma-Aldrich, ACS 99.8+%) were tested and used as solvents. Aluminum oxide nanoparticles (Alfa

Aesar, 20% in H<sub>2</sub>O, 0.05-micron particles) and polyethersulfone (PES, Veradel 300p) were used to create unique microstructures.

### **6.2.2 Aerosol-assisted synthesis setup**

The AAS setup consists of mainly three parts: a nebulizer, a tube furnace, and a gas washing bottle as a collection device (see Fig. 6-1). A commercially available humidifier was used as a nebulizer, the diaphragm of which was in direct contact with a glass tube containing a precursor solution. Aerosols of the precursor solution were carried to a glass tube (I.D. = 22.5 mm, Length = 40 cm) inside a tube furnace (Thermo Lindburg/Blue M) using an argon carrier gas at 300 cc/min. Finally, powder samples were collected and washed with DMF.

### **6.2.3 Aerosol-assisted Synthesis of HKUST-1**

In a typical synthesis, 0.525 g (2.26 mmol) of copper(II) nitrate semi(pentahydrate) and 0.25 g (1.19 mmol) of 1,3,5-benzenetricarboxylic (H<sub>3</sub>BTC) acid were dissolved in 30 ml of solvent under stirring. The stirring was continued for 10 min after complete dissolution. The precursor solution was then transferred in the ultrasonic nebulization chamber and subjected to nebulization upon which aerosol droplets were generated (see Fig. 6-1). The size of nebulized droplets is estimated to be ~ 5 μm. The argon carrier gas carried aerosol droplets into the tube furnace set at a specified temperature. Products were collected in a gas washing bottle containing 400 ml of fresh DMF. When bulkier solvents such as DMF or DMSO were used, solvent molecules trapped in the crystals were exchanged with ethanol as reported.[36] The newly collected HKUST-1 crystals (hereafter, AAS-HKUST-1)



were immersed in fresh ethanol overnight at room temperature. The powder was then centrifuged and dried at reduced pressure for 24 h in a vacuum oven before analysis.

#### **6.2.4 Solvothermal Synthesis of HKUST-1**

The same precursor solution was used as above but with both pure DMF and 50/50 DMF/DMSO mixture. After mixing, the solution was transferred into a Teflon-lined autoclave and reacted at 110 °C for 1 d in a convection oven. The resulting HKUST-1 crystals (hereafter, ST-HKUST-1) underwent solvent exchange and drying steps as above.

#### **6.2.5 Synthesis of Al<sub>2</sub>O<sub>3</sub>/HKUST-1 composite**

Al<sub>2</sub>O<sub>3</sub> nanoparticles were collected from 15 g of an aqueous suspension by centrifuging at 8000 rpm for 10 min and washed twice with equal-molar DMF/DMSO mixture. These alumina particles were then primed by dispersing in 30 ml of equal-molar DMF/DMSO solution containing 0.25 g of BTC and subsequently subjecting to thermal treatment at 120 °C for 20 min. After cooled down, 0.525 g of copper(II) nitrate semi(pentahydrate) was added and then subsequently followed by the aforementioned AAS procedure.

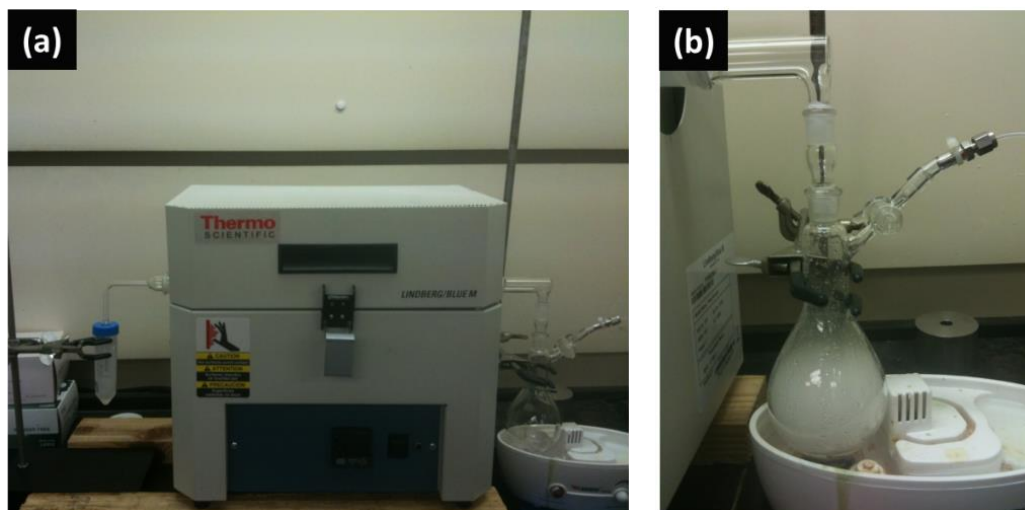
#### **6.2.6 Synthesis of PES/HKUST-1 composite**

0.1g of PES was dissolved in an equal-molar DMF/DMSO solution, followed by addition of CuN and BTC. The mixture solution was subsequently subjected to the aforementioned AAS procedure. It is noted that the synthesis was conducted at 140 °C instead of 110 °C and ethanol was used for sample collection and washing instead of DMF to avoid the dissolution of PES from the composite particles.

### 6.2.7 Characterizations

Powder X-ray diffraction (PXRD) patterns were collected from Rigaku Miniflex II powder X-ray diffractometer with Cu-K $\alpha$  radiation ( $\lambda = 1.5406 \text{ \AA}$ ). Field emission scanning electron micrographs were acquired from a JEOL JSM-7500F system operated at an acceleration voltage of 2 keV and a working distance of 15 mm. N<sub>2</sub> adsorption measurements were conducted using a Micrometrics ASAP 2010 system at 77K. The sample was fully activated at 160 °C under high vacuum before N<sub>2</sub> adsorption analysis and turned purple from its original blue color. Fourier transform infrared spectra (FT-IR) were collected using a Thermo iS5 FTIR system with potassium bromide as the mirror material accumulating a total of 64 scans from 400 to 4000 cm<sup>-1</sup> with a resolution of 0.241 cm<sup>-1</sup>.

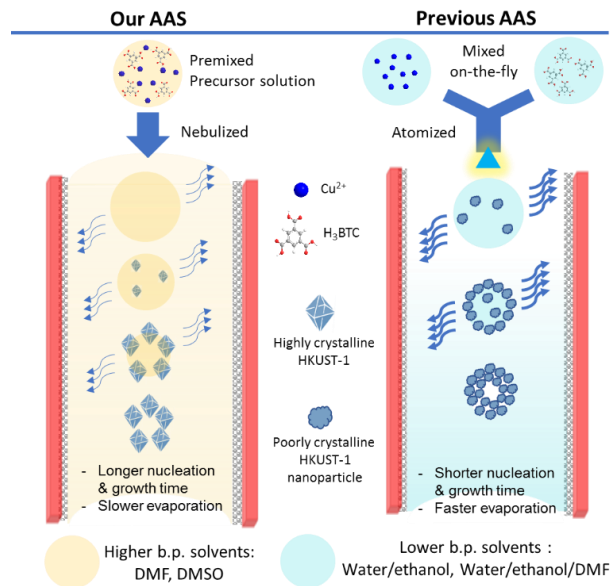
### 6.3 Results and discussion



**Figure 6-1. Pictures of the AAS setup (a) and the nebulization part (b).**

Typical residence times in spray-drying or AAS processes are less than one second [190, 193] or a few seconds respectively.[175] Since the reaction time must be shorter than the residence time, water and ethanol that are less Lewis-basic (thereby less competition over metal centers with ligands) than DMSO or DMF were commonly used in spray-drying and AAS processes[175, 188, 190] (see Table S1). Because of the short reaction time, extra care is required to prevent the crystallization reactions prior to the processes. Otherwise, it is difficult to discern particles formed before from those upon the processes. In most of the previously reported processes, metal and ligand solutions were mixed just before nebulization (i.e., AAS)[175] or introduced simultaneously into spray-dryer. [190] Furthermore, high vapor pressure solvents such as methanol and ethanol can evaporate rapidly during the processes (that is, short residence time). Due to this fast crystallization and short residence time, resulting MOF crystals tend to be underdeveloped (i.e.,

nanocrystals with less crystallinity, lower surface area, and poorly-defined crystal facets) and even amorphous phase can form.



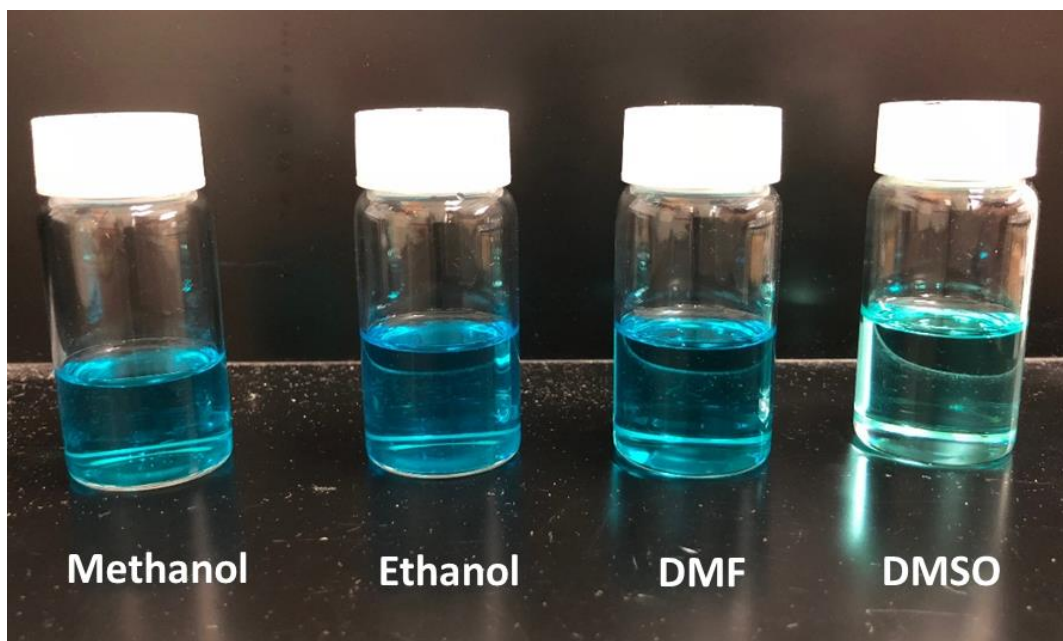
**Figure 6-2. Schematic illustration for comparing our AAS process with previously reported AAS or spray-drying processes.**

To achieve high-quality MOF crystals by AAS, it was hypothesized to be critical 1) to stabilize precursor solution (i.e., slow crystallization), thereby preventing crystallization prior to the process and 2) to reduce the solvent evaporation rate, and hence increasing time for crystal growth. In fact, Boissiere et al.[33] obtained HKUST-1 nanocrystals exhibiting relatively high surface area by substantially lowering precursor concentration, thereby decreasing crystallization rate. Fig. 6-2 illustrates our AAS process and compares with previously reported AAS processes.[175, 190]

Solvents play critical roles not only in stabilizing precursor solutions but also in reducing solvent evaporation rates. It is reminded that most solvents of the



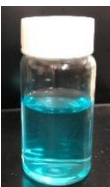

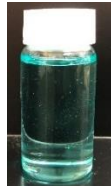



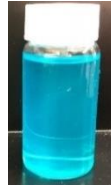






previously reported spray-drying/AAS contains either water or ethanol, [175, 188, 190] leading to the relatively fast crystallization and/or rapid solvent evaporation. It was presumed that solvents with greater donor numbers are more effective in reducing precipitation rates, thereby stabilizing precursor solutions. This is due to the fact that the greater the donor number, the stronger Lewis base the solvent, thereby more effective in competing with ligands.[194]

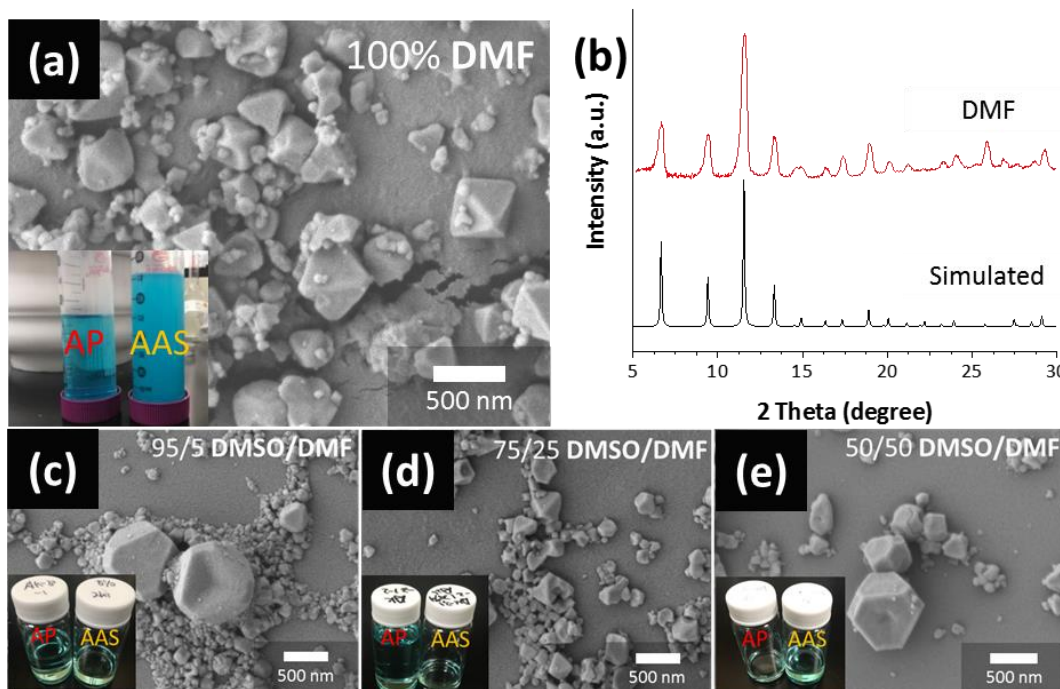
Table 6-1 presents pictures of precursor solutions with various common solvents for MOF synthesis as-mixed and after stirring for 5 and 30 min along with their donor numbers and boiling points.[195] Solutions with methanol and ethanol led precipitation after a few minutes of stirring (not shown in the table) while the one with DMF showed less precipitation. On the contrary, the solution with DMSO remained clear, indicating no appreciable precipitation of HKUST-1. As argued above, DMSO with stronger Lewis basicity is capable of coordinating with transition metal centers including copper (i.e., a modulator),[196, 197] further stabilizing the precursor solution. As can be seen in Fig. 6-3, with the same molar ratio, copper nitrate dissolved in DMSO shows a lighter blue color verses the comparing samples, possible indicating difference in coordination environments. For copper complexes such as  $[\text{Cu}[\text{Au}(\text{CN})_2]_2(\text{DMSO})_2]$ , [198]  $[\text{CuCl}_2(\text{DMSO})_2]$  [199] and  $\text{Cu}(\text{NO}_3)_2(\text{DMSO})_3$  [200] with DMSO, Cu centers are in a typical trigonal bipyramid geometry (coordination number, CN = 5) while they are in the paddlewheel SBU of HKUST-1 (CN = 6). Such a geometrical transformation might help to further hinder HKUST-1 precipitation.



**Figure 6-3. Pictures of as-mixed metal solutions with methanol, ethanol, DMF, and DMSO. The molar ratio of metal: solvent = 1: 177.**

**Table 6-1. Donor numbers and boiling points of various solvents and the stability of corresponding precursor solutions upon stirring.**

	Methanol	Ethanol	Water*	DMF	DMSO
Donor number	19.0	20.0	N/A	26.6	29.8
Boiling point /°C	64.7	78.4	100	153	189
As mixed					
After 5 min					
After 30 min					

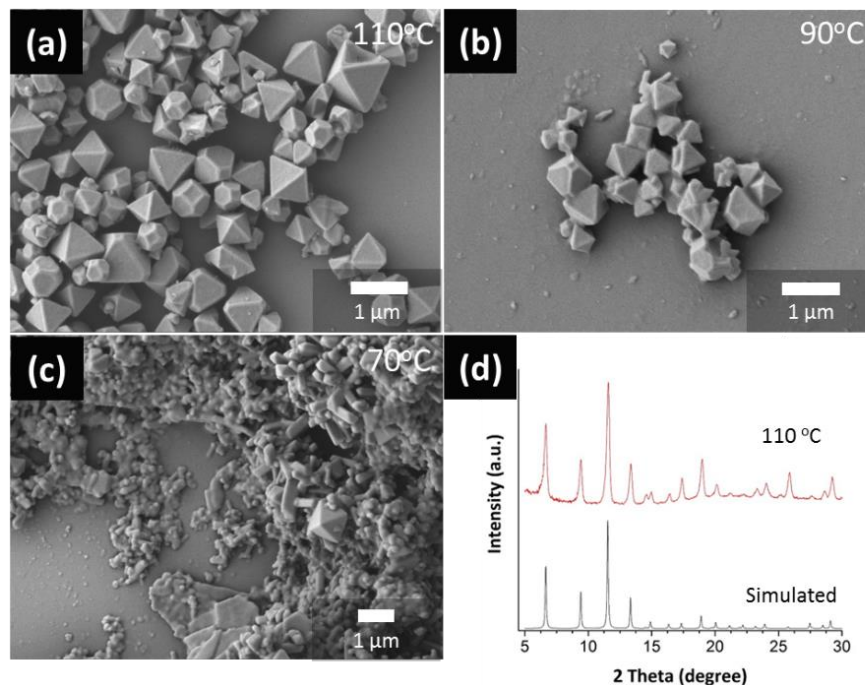


**Figure 6-4.** SEM images of AAS-HKUST-1 synthesized in DMF (a) and mixed solvents with 95% (c), 75% (d), and 50% (e) of DMSO with DMF at 180 °C and PXRD (b) of sample (a). Optical images of their as-prepared (AP) solutions and residual solutions (AAS).

Based on the observation made above, DMF and DMSO were chosen for AAS process. Fig. 6-4 presents the SEM images of HKUST-1 particles synthesized using DMF and DMSO/DMF mixed solvents at 180 oC and the X-ray diffraction pattern of particles synthesized in pure DMF. As can be seen in Fig. 6-4a, DMF led to the formation of typical octahedral HKUST-1 crystals with well-defined facets. It was, however, observed noticeable precipitation developed in the precursor solution during the AAS process (see inset optical micrographs in Fig. 6-3a). Consequently, the resulting product showed the presence of nanoparticles and microparticles with a somewhat bimodal distribution in size. The PXRD in Fig. 6-4b confirmed the presence of a substantial number of nanoparticles evidenced by the peak broadening. Since it was not possible to produce appreciable number of particles with pure DMSO, we then attempted to introduce DMSO into DMF to enhance the stability of the precursor solution. Though the solutions remained clear after introducing DMSO,



resulting crystals synthesized are quite small in numbers for 95/5, 75/25, and 50/50 DMSO/DMF mixtures. Nevertheless, 50/50 DMSO/DMF seems better to obtain quality crystals with relatively narrow size distribution, thereby chosen for further studies.



**Figure 6-5. SEM images of AAS HKUST-1 synthesized using 50/50 DMSO/DMF at different oven temperatures: 110°C (a), 90°C (b), and 70°C (c) and the PXRD pattern of the sample at 110°C (d).**

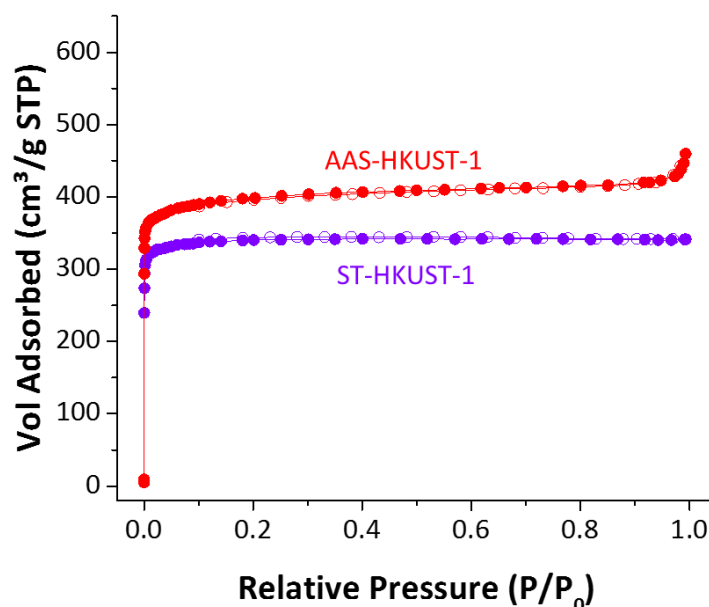
Given solvents, furnace temperature determines the evaporation rate, thereby the residence time. Fig. 6-5 presents the SEM images and powder X-ray diffraction pattern of HKUST-1 crystals synthesized using a 50/50 DMSO/DMF at different temperatures. Narrowly-dispersed HKUST-1 sub-micron crystals (average size:  $0.72 \pm 0.27 \mu\text{m}$ ) with mostly typical octahedral or truncated-octahedral geometry and well-defined facets were formed with a 50/50 DMSO/DMF when the oven

temperature was reduced to 110 °C from 180 °C (see Fig. 6-2c). It is noted that the morphology and size of the HKUST-1 crystals are distinctly different from previously reported particles by either spray-drying [188] or AAS.[175] These high-quality HKUST-1 crystals were formed likely due to the extended time for crystal growth made possible by both the modulating effect and the high boiling point of DMSO. When the oven temperature was decreased to 90 °C, a small number of rod-shaped crystals can be observed. As the oven temperature was further lowered to 70 °C, however, the majority of the products was unknown phase. Fig. 6-6 presents the N<sub>2</sub>-adsorption isotherm of the AAS-HKUST-1 sample synthesized at 110°C as well as our ST-HKUST-1 sample. Both of them showed a typical Type-I isotherm, similar to that of the ST-HKUST-1 previously reported.[201] consequently, the sample exhibited relatively high BET (~1600 m<sup>2</sup>/g) and Langmuir surface area (~1800 m<sup>2</sup>/g), which are considerably higher than those reported (see Table 6-2). This observation clearly indicates that the quality of the AAS-HKUST-1 is comparable to those by solvothermal batch processes.

**Table 6-2. Surface areas and pore volumes of AAS-HKUST-1 in comparison with those reported earlier. ST and SD represent solvothermal and spray-drying, respectively.**

	<b>BET surface area m<sup>2</sup>/g</b>	<b>Langmuir surface area m<sup>2</sup>/g</b>	<b>Pore volume cm<sup>3</sup>/g</b>	<b>External surface area m<sup>2</sup>/g</b>
AAS-HKUST-1 (this work)	1586 ± 3.4	1793.7 ± 3.9	0.62	23.4
ST-HKUST-1 [201]	1482	N/A	0.753	N/A
SD-HKUST-1 [188]	1260	N/A	N/A	N/A
AAS-HKUST-1* [175]	649 - 1270	N/A	0.18 - 0.39	N/A

\* Synthesized with copper nitrate salts. Marquez et al.[190] reported AAS-HKUST-1 with higher quality. However, due to the fact that their precursor solutions were highly diluted, it's not included in this table.



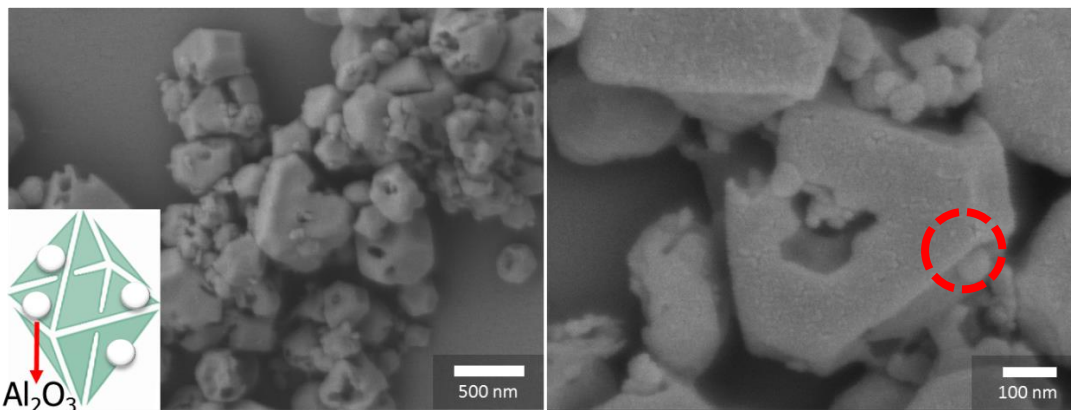
**Figure 6-6. N<sub>2</sub> adsorption/desorption isotherms of AAS-HKUST-1 and ST-HKUST-1.**

It is reminded that the majority of the reported HKUST-1 particles synthesized via spray-drying [188] or AAS [175] exhibit self-assembled hollow spheres of nanoparticles. This is likely due to the fact that the fast evaporation and reaction lead to formation of many nuclei, thereby nanocrystals in a droplet. Upon rapid evaporation of solvent in the droplet results in the self-assembly of nanoparticles that are pinned at the evaporating front of the droplet (see Fig. 6-2).[175] On the contrary, high-quality HKUST-1 crystals were obtained in our AAS process. As hypothesized and illustrated in Fig. 6-2, this was ascribed to the increased time for crystal growth resulting from slow evaporation rates due to 1) relatively low furnace temperature and 2) low vapor pressure of solvents. Table 6-3 compares reported spray-drying and AAS processes with our AAS process.

Effective ways to impart new or enhanced functionalities to MOFs include: 1) forming composites with other materials and 2) introducing hierarchical pore structures. Though AAS or spray-drying resulted in various composites and unique microstructures and embedding MOFs with metal nanoparticles,[187] there have been reports neither on the formation of MOF/polymer composites for introducing mesopores and/or macropores. Fig. 6-7 presents the SEM images of well-defined HKUST-1 crystals embedded with alumina nanoparticles (~50 nm) that were introduced in the precursor solution. As can be seen in the figure, cavities with diameters of ~ 100 nm were created. As described in the experimental section, priming alumina particles with BTC was found critical in order to incorporate alumina nanoparticles into HKUST-1 frameworks (see Fig. 6-7). This unique

hierarchically porous MOF composites might be interesting for heterogeneous catalysis, given the fact that HKUST-1 contains open-metal sites and is known to be Lewis acid catalyst.[21, 202, 203]

When polyethersulfone (PES) polymer was introduced into precursor solutions, hollow spherical composite structures (hereafter, PES/HKUST-1) were formed as shown in Fig. 6-9. A couple of observations can be made. First, even though the rest of the conditions was similar to those for HKUST-1 crystals, HKUST-1 nanocrystals were formed when PES was added. This is attributed to the strongly-polar sulfonic groups of the polymer that can serve as nucleation sites, promoting nucleation rates.[204] The enhanced nucleation leads to the formation of more nuclei, thereby more but smaller crystals. In a similar manner as previous reports,[175] the evaporation of the solvent from droplets causes the self-assembly of nanoparticles that are pinned at the evaporating droplet front. However, it appears that our hollow spheres are single-layered (see Fig. 6-9b) while previously reported hollow spheres are multi-layered. Due to the presence of PES confirmed by FTIR (Fig. 6-10) acting as a binder, these hollow spheres appear mechanically more stable since a mechanical force was applied to break the spheres (Fig. 6-9b). It should be noted that our HKUST-1 was formed during the AAS process, different previously reported HKUST-1/polymer composite structures.[184, 205]

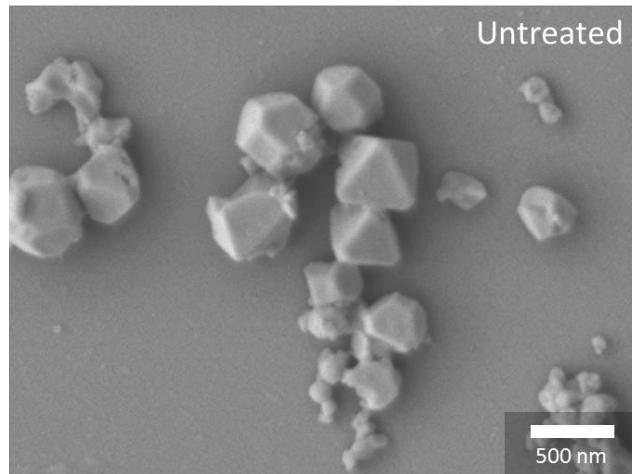


**Figure 6-7. SEM images of Al<sub>2</sub>O<sub>3</sub>/HKUST-1 composite structure (left) and the magnified image. Al<sub>2</sub>O<sub>3</sub> nanoparticles were marked in a red circle.**

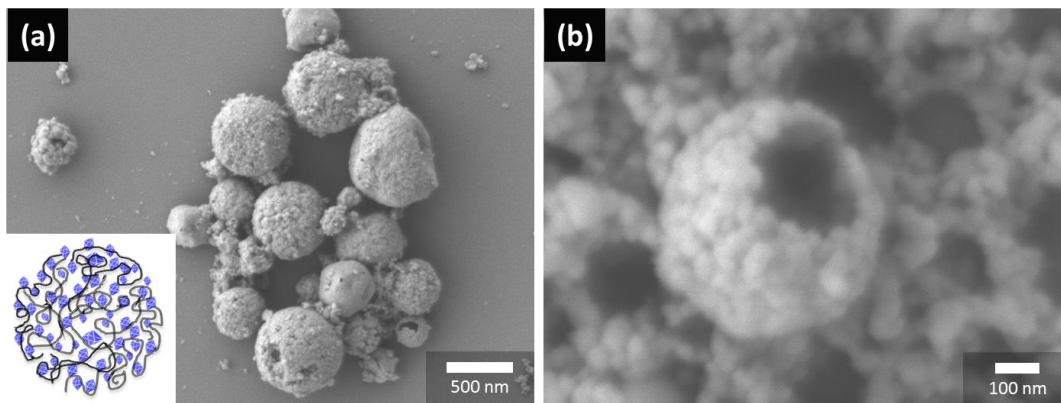
**Table 6-3.** Summary of spray-drying and AAS processes applied for MOF synthesis

	Year	Authors	Material	Properties for MOF powder synthesis			Deprotonator	Typical morphology	Ref.
				Solvents	Precursor composition metal:ligand:solvent	Premixing			
Spray-Drying	2013	MasPOCH et al.	HKUST-1	ethanol, water	1:0.64:72	Yes	No	Hollow spherical assembly of nanoparticles**	[188]
			ZIF-8	water	1:0.1:7	No			
			UiO-66	DMF, water	1:1:175	Yes, with preheating			
			...	...	...	...			
2016	MasPOCH et al.	UiO-66					spherical aggregate*	[191]	
AAS	2013	Boissiere et al.	HKUST-1	ethanol, water	1:0.55:704	No	No	Hollow spherical assembly of nanoparticles	[190]
			ZIF-8	methanol	1:8.5:1045				
	2017	Kubo et al.	HKUST-1	ethanol, water, DMF	1:0.55:152	No	No	Hollow spherical assembly of nanoparticles**	[175]
	2018	Jeong et al.	HKUST-1	DMF, DMF/DMSO	1:0.53:177*	No	No	Octahedral crystals with an average diameter of 720 nm	This work

\*spray-drying combined with a flow method was used. \*\*Products contained amorphous material

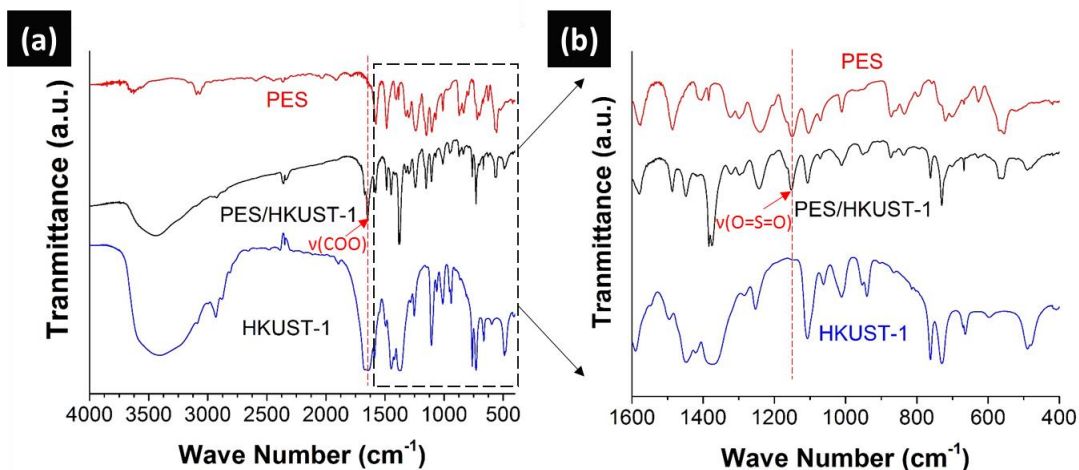


**Figure 6-8. SEM images of Al<sub>2</sub>O<sub>3</sub>/HKUST-1 composite without priming, showing little incorporation of alumina nanoparticles in HKUST-1.**

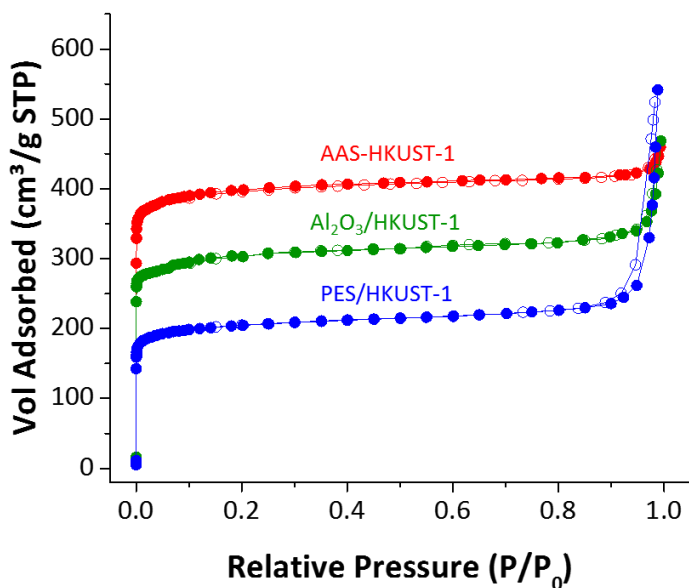


**Figure 6-9. SEM images of PES/HKUST-1 composite structure as-synthesized (a) and as broken mechanically (b).**





**Figure 6-10.** FTIR spectra of PES/HKUST-1 composites in comparison with those of PES and HKUST-1 (a) and the magnified view of the finger-print region (b). The stretching motion of carboxylate groups of HKUST-1 and sulfone group of PES were marked in red arrows



**Figure 6-11.** N<sub>2</sub> adsorption and desorption isotherms at 77K of AAS-HKUST-1, Al<sub>2</sub>O<sub>3</sub>/HKUST-1, and PES/HKUST-1. Solid and hollow circles indicate adsorption branch desorption branch, respectively

Fig. 6-11 compares nitrogen isotherms of Al<sub>2</sub>O<sub>3</sub>/HKUST-1 and PES/HKUST-1 with that of AAS-HKUST-1. It is noted that all three samples were prepared under almost identical conditions. Table 6-4 summarizes the results. Both Al<sub>2</sub>O<sub>3</sub>/HKUST-1 and PES/HKUST-1 samples showed reduced BET and Langmuir surface areas owing to the incorporation of alumina or PES. However, their external surface areas were significantly increased, in particular, in the case of PES/HKUST-1. What's more, hysteresis can be observed for PES/HKUST-1 which indicates the existence of mesopores.

**Table 6-4. Surface areas and pore volumes of AAS-HKUST-1, Al<sub>2</sub>O<sub>3</sub>/HKUST-1 and PES/HKUST-1**

	<b>BET surface area m<sup>2</sup>/g</b>	<b>Langmuir surface area m<sup>2</sup>/g</b>	<b>Pore volume cm<sup>3</sup>/g</b>	<b>External surface area m<sup>2</sup>/g</b>
AAS-HKUST-1	1586 ± 3.4	1793.7 ± 3.9	0.62	23.4
Al <sub>2</sub> O <sub>3</sub> /HKUST-1	1189.9 ± 1.0	1377.7 ± 4.3	0.46	37.2
PES/HKUST-1	666.6 ± 13.3	937.4 ± 3	0.26	529.5

## 6.4 Conclusions

We reported high-quality HKUST crystals with well-defined facets and high specific surface areas and their unique composites with both inorganic and organic materials using a scalable aerosol-assisted synthesis. To obtain high-quality crystals using AAS, we found DMSO in DMF is effective in stabilizing precursor solutions as well as increasing residence time, thereby decreasing nucleation and increasing

crystal growth time likely due to its coordination with metal centers and relatively low vapor pressure. The resulting HKUST-1 crystals were phase-pure, exhibiting a typical octahedral shape and surface area much higher than most of the HKUST-1 particles synthesized by AAS or by spray-drying. Furthermore, alumina nanoparticles and polyethersulfone (PES) polymer were readily incorporated to create unique microstructures. Facile continuous production of high-quality MOF crystals and MOF composites with unique microstructures are expected to be useful for their cost-effective practical applications in catalysis, adsorption, and delivery.

## 7. FUTURE WORK: SYNTHESIS OF HIGH-ASPECT RATIO ZIF-8 CRYSTALS FOR MEMBRANE APPLICATIONS

### 7.1 Introduction

Zeolitic imidazolate frameworks (ZIFs) consists of tetrahedrally-coordinated metal centers interconnected with bidentate imidazole-derived ligands, forming 3-dimensionally-interconnected framework. Among them, zinc ions and 2-methylimidazole can steadily form sodalite (SOD) ZIF-8, with an  $\bar{I}43m$  symmetry. Even though ZIF-8 has been proved as extremely effective for propylene/propane separation, as mentioned in the previous chapters, its high membrane price, as well as cracks formation, hinder ZIF-8 polycrystalline membranes from large-scale industrial applications, for which, 2D-membrane may provide a radical solution.

Stacking nanosheets or high-aspect-ratio crystals on the top of porous support can form a continuous layer as membrane. Unlike traditional polycrystalline membranes, such a stacked membrane can not only much thinner inherently. There will also be a less possibility of forming penetrated crystal boundaries. Traditional polycrystalline membrane usually possesses crystal boundaries perpendicular to the support surface, and a crack of merely several hundred nanometers can greatly reduce the performance of a traditional polycrystalline membrane. However, for stacked membrane, most of its crystal boundaries are horizontal and the mechanical property of the membrane is much more homogenous.

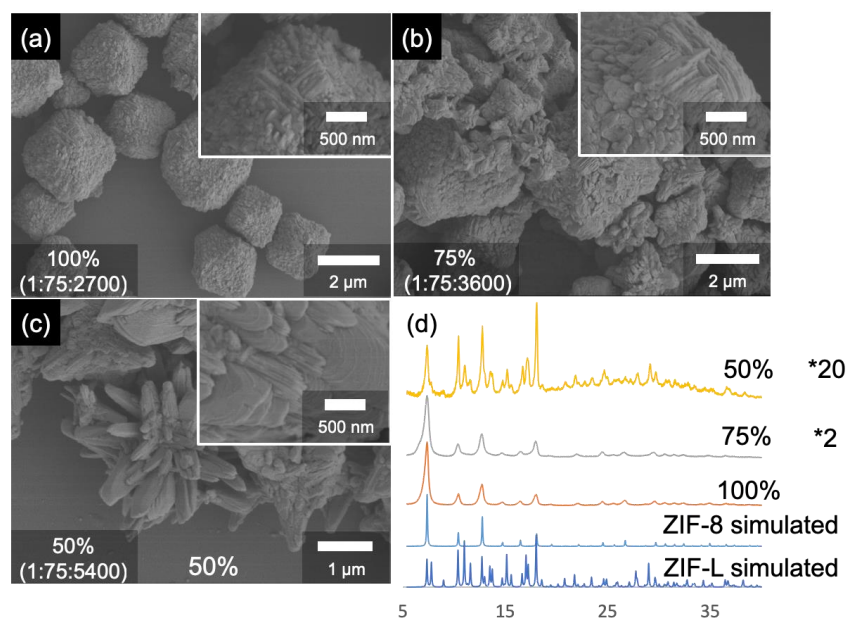
However, because of its high-symmetry, the synthesis of ZIF-8 nanosheets/high-aspect-ratio crystals are challenging both theoretically and

practically. On the other hand, several inspiring works have pointed out the possibility of such a synthesis. Hong et al.[206] used cetrimonium bromide (CTAB) and tris(hydroxymethyl)aminomethane (TRIS) as capping agents and successfully synthesized ZIF-8 crystals with various morphologies. Among which, flakes-like crystals were synthesized and characterized with XRD, showing additional peaks coming from ZIF-L alongside with its major ZIF-8 peaks. The thickness of one flake of these crystals is only 20 nm while in another direction, it can extend to several hundred nanometers. However, these crystals are twinning crystals of several flakes developing in multiple directions. In 2018, Pan et al.[206] demonstrated the synthesis of plate-like ZIF-8 crystals (thickness ~100 nm), as well as several other ZIF-8 crystals (e.g. nanorods) by the use of CTAB and presented a phase-diagram of precursor concentration and CTAB concentrations. These crystals were also incorporated into mixed matrix membranes and tested for propylene/propane separation.

Another important material that worth mentioning is ZIF-L, which shares part of its crystals structure with ZIF-8. Reported by Wang et al.,[207] ZIF-L are typically formed in aqueous solution with relatively low metal to ligand ratio (typically 1:8). Leaf-like crystals with a thickness of 100 nm can be formed and their length can reach 1  $\mu\text{m}$ . As mentioned above, even crystal morphologies are uniform, both ZIF-8 and ZIF-L have been detected under XRD in the case of Hong et al.[206] Similar XRD patterns have been observed even before the discovery of ZIF-L.[208] These facts indicate the possibility of forming a mixed structure of ZIF-L and ZIF-8.

Here, we present the first case of high-aspect-ratio ZIF-8 crystals/nanosheets, synthesized without capping agents and modulators, but only aqueous heterogeneous growth under reduced temperature. Several crystals with different morphology were synthesized while the best one shows a thickness of only 20nm and a length of several micrometers. These crystals showed ZIF-8 patterns with additional peaks from ZIF-L. Their crystals proved to be able to grow on different support (ceramic, polymeric) and exfoliatable from their supports, readily for stacking on support and potential membrane applications.

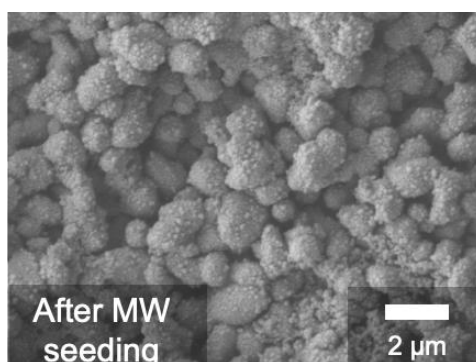
## 7.2 Initial results



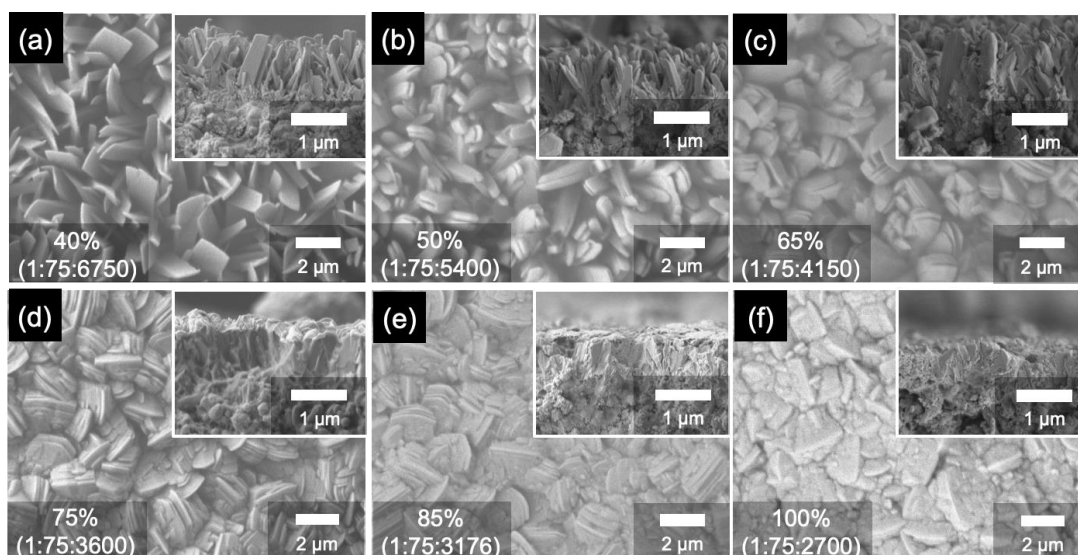
**Figure 7-1. (a-c) SEM images of powder sample synthesized at 4 °C for 2 d with different concentration and (d) their corresponding PXRD pattern**

Powder samples of ZIF-8 were synthesized in an aqueous solution at 4°C for 1 d, showing untypical morphologies. Typical ZIF-8 crystals show dodecahedron, cubic, octahedron or truncated dodecahedron morphologies without the presence of

modulators or capping agents. In our case, flake-like crystals (see Fig.7-1c) was observed when the solution was diluted to 50% (molar ratio, metal:ligand:water=1:75:5400), of which the XRD pattern indicates the coexistence of both ZIF-8 and ZIF-L. Such an observation indicate this sample may have close connection with the flake-like crystals as reported by Hong et al.[206] For our 75% (molar ratio, 1:75:3600) sample, two types of crystals can be seen. Except for flake-like crystals (smaller however than the 50% sample), the other kind of crystals shows a truncated octahedral morphology. Its 6 truncated facets show a stack of flakes perpendicular to each other as shown in the inserted image in Fig. 7-1b, while the other facets are also unsmooth, unlike any reported cases. The PXRD pattern of our 100% sample matches perfectly with the simulated pattern of ZIF-8. Comparing to the 75% sample, no flake-like crystals can be seen under SEM, while the truncated octahedral crystals look exactly like the ones in our 75% samples under SEM.



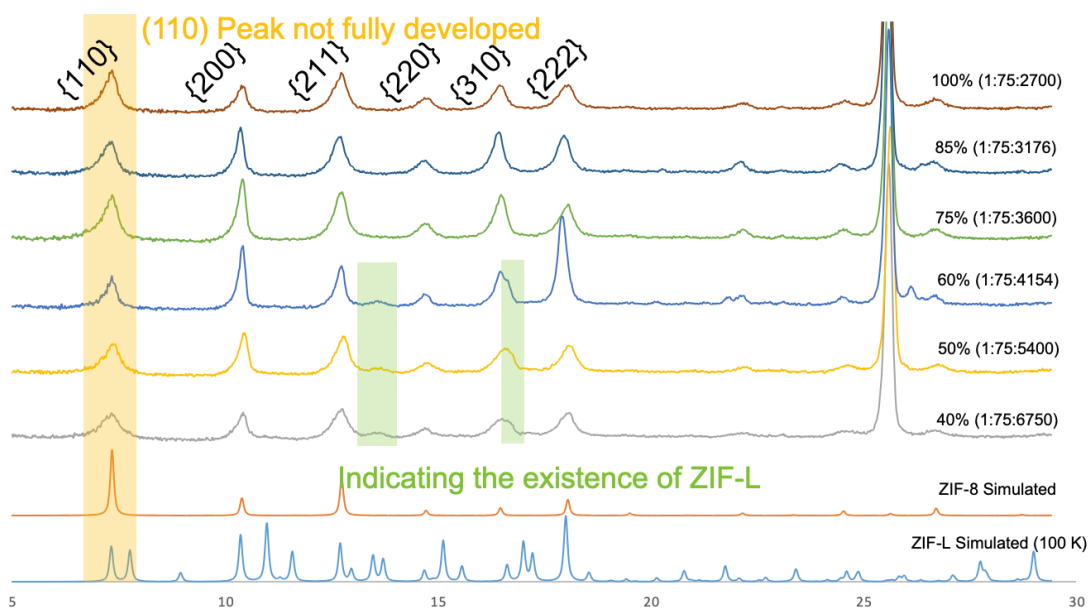
**Figure 7-2. Microwave seeded support covered with nanosized ZIF-8 particles**



**Figure 7-3. Top view of the alumina support after secondary growth of 1 day under different concentrations: (a) 40% concentration (metal:ligand:water=1:75:6750), (b) 50% (1:75:5400), (c) 65% (1:75:4150), (d) 75% (1:75:3600), (e) 85% (1:75:3176) and (f) 100% (1:75:2700).**

A similar strategy was employed for the secondary growth of microwave seeded alumina supports. As seen in Fig. 7-2, the alumina support covered by a layer of densely packed nanocrystals, by using the modified recipe adopted from Kwon et al.[39] After a 1-day secondary growth with the same recipe as our powder sample, these seeded supports show different morphologies according to their concentrations. When the concentration was 100% (see Fig. 7-3f), it shows a typical morphology of common polycrystalline membranes. However, when the secondary growth solution was slightly diluted to 85% (1:75:3176), the top-view SEM images show a stack of crystal flakes. As the concentration was further reduced, the number of flakes stacking together was reduced and the distance between them became bigger. Finally, at 65%, the gap between each flake can be clearly seen. When the concentration is 40%, there existed only one flake.

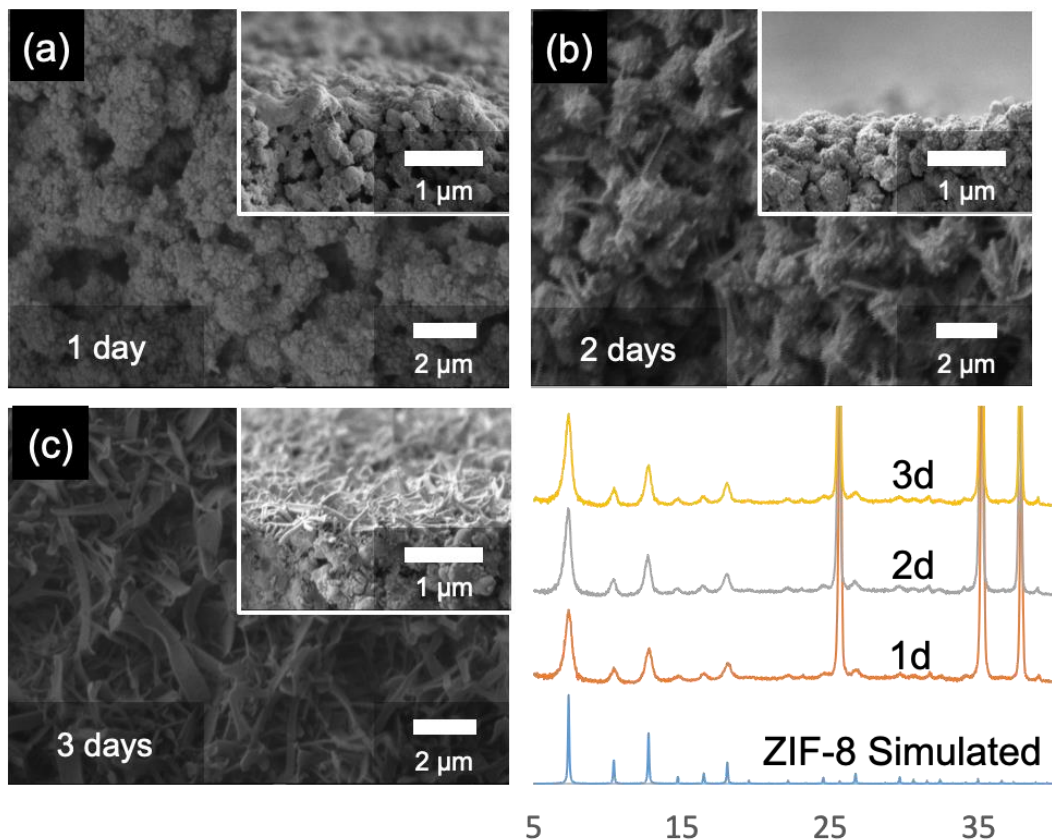




**Figure 7-4. XRD pattern of the alumina supports after secondary growth of 1 day under different concentrations: 40% concentration (metal:ligand:water=1:75:6750), 50% (1:75:5400), 65% (1:75:4150), 75% (1:75:3600), 85% (1:75:3176) and 100% (1:75:2700).**

Fig. 7-4 includes the XRD pattern for all the samples in Fig.7-2. After comparison, the 100% sample shows a similar pattern compared to the simulated pattern, while the 85%, 75%, and 60% sample show a preferred orientation of the (200) peak. The 60% sample has a strong peak close to (222), which might originate from ZIF-L. Also, for our 60%, 50% and 40% sample, there exists additional peak after (211) and (310) peak, which is also comes from ZIF-L, as described by Hong et al.[206] Comparing Fig. 7-2 and Fig. 7-3, homogenous phases show two XRD patterns which indicate the coexistence of both ZIF-8 and ZIF-L in the same crystal. In addition, as the concentration decreases, the peak corresponding to ZIF-L

increases, which also matches with our previous observations for powder sample syntheses.

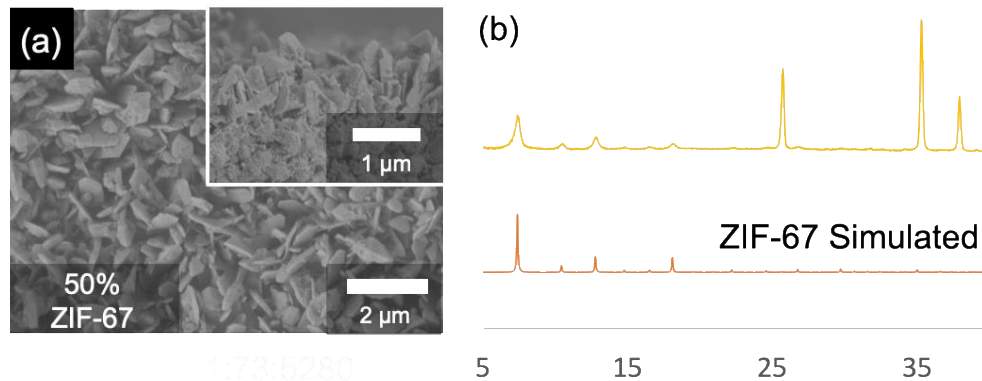


**Figure 7-5. SEM micrographs of alumina supports after secondary growth under 25% concentrations (metal:ligand:water=1:75:10800) of different growth time: (a) 1 day, (b) 2 days, (c) 3 days, and their corresponding XRD patterns.**

As shown in Fig. 7-5, nanobelt-like ZIF-8 crystals can be gradually synthesized with even lower concentration (25%, 1:75:10800), with an extended reaction time of 3 d. For the 1-day sample, no obvious growth can be seen. Upon the growth of 3 d, belt-like crystals with a width of ~200 nm, a thickness of 20 nm-30 nm and a length of several micrometers appeared. The corresponding XRD peak of

all these samples showed no additional peak other than those of ZIF-8 and the intensity increased as the growth time increases.

The same strategy was adopted for ZIF-67 syntheses and it ZIF-67 crystals with similar flake-like morphology was grown on the seeded support, as presented in Fig. 7-6. ZIF-67 shares the same SOD structure as ZIF-8 but consists of cobalt metal ions instead of zinc ions. The secondary growth was conducted on alumina seeded with ZIF-67 nanoseeds and at the same conditions as our ZIF-8 growth.



**Figure 7-6. XRD pattern of the alumina supports after secondary growth under 50% concentrations (metal:ligand:water=1:73:5280) with a growth time of 1 d at 4°C.**

## 7.3 Objectives

### 7.3.1 Task 1, Further characterization of the powder sample

Since all of our crystals were grown on supports seeded with ZIF-8 (or ZIF-67), there exist inherently two kinds of crystals by nature. Therefore, XRD alone may not be able to support the claim that our crystals are predominantly ZIF-8. Further characterization like selected area electron diffraction (SAED) might be

necessary. However, taking SAED under TEM requires powder sample or sample grown on soft supports.

On the other hand, as we have highly suspected, our crystal might contain both ZIF-8 and ZIF-L and if so, chances are likely that these ZIF-L should be concentrated on the surface and serves as a kinetic intermediate which will later transform into ZIF-8. As such, NMR and FTIR is necessary for confirming the existence of ZIF-L

### **7.3.2 Task 2, Exfoliation and the formation of ultrathin membranes**

Our high-aspect-ratio ZIF-8 crystals can provide an unprecedented opportunity for reducing the thickness of ZIF-8 polycrystalline membranes/mixed matrix membranes into the nanometer scale. By stacking such a high-aspect-ratio on top of a porous support and then applying secondary growth, a continuous membrane with thickness with a thickness of around 200 nm (estimated imprecisely) might be formed. In addition, by combining polymeric materials and our high-aspect-ratio crystals, mixed-matrix membranes can be formed with also relatively small thickness. Currently, most mixed matrix membranes use particles larger than 100 nm, therefore also limit the minimums thickness of these membranes.[209]

However, both applications naturally require power form of high-aspect-ratio ZIF-8 as a prerequisite, while might be viable through growing our ZIF-8 on polymeric supports and subsequently dissolving the polymer.

## 8. CONCLUSION

In summary, MOFs and ZIFs are promising membrane materials for paraffin/oliffin separations. However, the pricy membrane cost and crack formation are greatly hindering the scaling-up and wide applications of these membranes. This dissertation tend to explore increase the productivity of soldlite ZIF membranes and reducing the membrane manufacturing cost by 1) enlarging the effective aperture size by doping cadmium metal nodes into ZIF-8 (based on zinc) frameworks; 2) use batter supports (e.g. ceramic tubes) to increase the packing density; 3) greatly reducing the membrane thickness to reduce the gas transport resistance and increase the permeance of the membrane. These explorations shows that despite challenges coming from crystal phase stabilities, understanding of membrane formation mechanism, as well as other aspects, the productivity of ZIF membrane can be greatly increased (even several times).

Additional information regarding synthesizing 2-D ZIF-8 crystals as well as using aerol-assisted synthesis (AAS) for synthesizing high-quality HKUST-1 crystals as well as its composites with other organic/inorganic materials. These work may provide some fundermental understanding regarding the synthesis of MOFs.

## REFERENCES

1. Morgott, D.A., *The Human Exposure Potential from Propylene Releases to the Environment*. International Journal of Environmental Research and Public Health, 2018. **15**(1): p. 66.
2. Laurance, D.R. and G.W. Swift, *Relative volatility of propane-propene system from 100-160. deg. F*. Journal of Chemical and Engineering Data, 1972. **17**(3): p. 333-337.
3. Ma, X., et al., *Highly compatible hydroxyl-functionalized microporous polyimide-ZIF-8 mixed matrix membranes for energy efficient propylene/propane separation*. ACS Applied Nano Materials, 2018. **1**(7): p. 3541-3547.
4. Sholl, D.S. and R.P. Lively, *Seven chemical separations to change the world*. Nature News, 2016. **532**(7600): p. 435.
5. Eldridge, R.B., *Olefin/paraffin separation technology: a review*. Industrial & Engineering Chemistry Research, 1993. **32**(10): p. 2208-2212.
6. Ravanchi, M.T., T. Kaghazchi, and A. Kargari, *Application of membrane separation processes in petrochemical industry: a review*. Desalination, 2009. **235**(1-3): p. 199-244.
7. Pandey, P. and R. Chauhan, *Membranes for gas separation*. Progress in Polymer Science, 2001. **26**(6): p. 853-893.
8. Grande, C.A. and A.E. Rodrigues, *Adsorption equilibria and kinetics of propane and propylene in silica gel*. Industrial & Engineering Chemistry Research, 2001. **40**(7): p. 1686-1693.
9. Pan, Y., et al., *Effective separation of propylene/propane binary mixtures by ZIF-8 membranes*. Journal of Membrane Science, 2012. **390**: p. 93-98.
10. Kang, S.W., et al., *Effect of the polarity of silver nanoparticles induced by ionic liquids on facilitated transport for the separation of propylene/propane mixtures*. Journal of Membrane Science, 2008. **322**(2): p. 281-285.
11. Song, Q., et al., *Zeolitic imidazolate framework (ZIF-8) based polymer nanocomposite membranes for gas separation*. Energy & Environmental Science, 2012. **5**(8): p. 8359-8369.

12. Carne, A., et al., *Nanoscale metal–organic materials*. Chemical Society Reviews, 2011. **40**(1): p. 291-305.
13. Shekhah, O., et al., *MOF thin films: existing and future applications*. Chemical Society Reviews, 2011. **40**(2): p. 1081-1106.
14. Rodenas, T., et al., *Metal–organic framework nanosheets in polymer composite materials for gas separation*. Nature Materials, 2015. **14**(1): p. 48.
15. Qiu, S., M. Xue, and G. Zhu, *Metal–organic framework membranes: from synthesis to separation application*. Chemical Society Reviews, 2014. **43**(16): p. 6116-6140.
16. Li, J.-R., J. Sculley, and H.-C. Zhou, *Metal–organic frameworks for separations*. Chemical Reviews, 2011. **112**(2): p. 869-932.
17. Shah, M., et al., *Current status of metal–organic framework membranes for gas separations: promises and challenges*. Industrial & Engineering Chemistry Research, 2012. **51**(5): p. 2179-2199.
18. Alezi, D., et al., *MOF crystal chemistry paving the way to gas storage needs: aluminum-based soc-MOF for CH<sub>4</sub>, O<sub>2</sub>, and CO<sub>2</sub> storage*. Journal of the American Chemical Society, 2015. **137**(41): p. 13308-13318.
19. Peng, Y., et al., *Methane storage in metal–organic frameworks: current records, surprise findings, and challenges*. Journal of the American Chemical Society, 2013. **135**(32): p. 11887-11894.
20. Gascon, J., et al., *Metal organic framework catalysis: Quo vadis?* Acs Catalysis, 2013. **4**(2): p. 361-378.
21. Lee, J., et al., *Metal–organic framework materials as catalysts*. Chemical Society Reviews, 2009. **38**(5): p. 1450-1459.
22. Horcajada, P., et al., *Porous metal–organic-framework nanoscale carriers as a potential platform for drug delivery and imaging*. Nature Materials, 2010. **9**(2): p. 172.
23. Horcajada, P., et al., *Flexible porous metal-organic frameworks for a controlled drug delivery*. Journal of the American Chemical Society, 2008. **130**(21): p. 6774-6780.

24. Sadakiyo, M., T. Yamada, and H. Kitagawa, *Rational designs for highly proton-conductive metal–organic frameworks*. Journal of the American Chemical Society, 2009. **131**(29): p. 9906-9907.
25. Hao, Z., et al., *One-dimensional channel-structured Eu-MOF for sensing small organic molecules and Cu 2+ ion*. Journal of Materials Chemistry A, 2013. **1**(36): p. 11043-11050.
26. Ramaswamy, P., N.E. Wong, and G.K. Shimizu, *MOFs as proton conductors—challenges and opportunities*. Chemical Society Reviews, 2014. **43**(16): p. 5913-5932.
27. Ma, D., et al., *A dual functional MOF as a luminescent sensor for quantitatively detecting the concentration of nitrobenzene and temperature*. Chemical Communications, 2013. **49**(79): p. 8964-8966.
28. Wang, L., et al., *Metal–organic frameworks for energy storage: Batteries and supercapacitors*. Coordination Chemistry Reviews, 2016. **307**: p. 361-381.
29. Wang, B., et al., *Colossal cages in zeolitic imidazolate frameworks as selective carbon dioxide reservoirs*. Nature, 2008. **453**(7192): p. 207.
30. Morris, W., et al., *Crystals as molecules: postsynthesis covalent functionalization of zeolitic imidazolate frameworks*. Journal of the American Chemical Society, 2008. **130**(38): p. 12626-12627.
31. Park, K.S., et al., *Exceptional chemical and thermal stability of zeolitic imidazolate frameworks*. Proceedings of the National Academy of Sciences, 2006. **103**(27): p. 10186-10191.
32. Banerjee, R., et al., *High-throughput synthesis of zeolitic imidazolate frameworks and application to CO<sub>2</sub> capture*. Science, 2008. **319**(5865): p. 939-943.
33. Tranchemontagne, D.J., J.R. Hunt, and O.M. Yaghi, *Room temperature synthesis of metal-organic frameworks: MOF-5, MOF-74, MOF-177, MOF-199, and IRMOF-0*. Tetrahedron, 2008. **64**(36): p. 8553-8557.
34. Hayashi, H., et al., *Zeolite A imidazolate frameworks*. Nature Materials, 2007. **6**(7): p. 501.



35. Shi, Q., et al., *Synthesis of ZIF - 8 and ZIF - 67 by steam - assisted conversion and an investigation of their tribological behaviors*. *Angewandte Chemie International Edition*, 2011. **50**(3): p. 672-675.
36. Tian, Y.Q., et al., *Cadmium imidazolate frameworks with polymorphism, high thermal stability, and a large surface area*. *Chemistry—A European Journal*, 2010. **16**(4): p. 1137-1141.
37. Karagiari, O., et al., *Synthesis and characterization of isostructural cadmium zeolitic imidazolate frameworks via solvent-assisted linker exchange*. *Chemical Science*, 2012. **3**(11): p. 3256-3260.
38. Mottillo, C. and T. Friščić, *Carbon dioxide sensitivity of zeolitic imidazolate frameworks*. *Angewandte Chemie International Edition*, 2014. **53**(29): p. 7471-7474.
39. Kwon, H.T. and H.-K. Jeong, *Highly propylene-selective supported zeolite-imidazolate framework (ZIF-8) membranes synthesized by rapid microwave-assisted seeding and secondary growth*. *Chemical Communications*, 2013. **49**(37): p. 3854-3856.
40. Zhang, C., et al., *Unexpected molecular sieving properties of zeolitic imidazolate framework-8*. *The Journal of Physical Chemistry Letters*, 2012. **3**(16): p. 2130-2134.
41. Liu, Y., et al., *Synthesis of highly c-oriented ZIF-69 membranes by secondary growth and their gas permeation properties*. *Journal of Membrane Science*, 2011. **379**(1-2): p. 46-51.
42. Pan, Y., et al., *Rapid synthesis of zeolitic imidazolate framework-8 (ZIF-8) nanocrystals in an aqueous system*. *Chemical Communications*, 2011. **47**(7): p. 2071-2073.
43. Pan, Y. and Z. Lai, *Sharp separation of C2/C3 hydrocarbon mixtures by zeolitic imidazolate framework-8 (ZIF-8) membranes synthesized in aqueous solutions*. *Chemical Communications*, 2011. **47**(37): p. 10275-10277.
44. Zhang, K., et al., *Investigating the intrinsic ethanol/water separation capability of ZIF-8: an adsorption and diffusion study*. *The Journal of Physical Chemistry C*, 2013. **117**(14): p. 7214-7225.

45. Huang, H., et al., *Effect of temperature on gas adsorption and separation in ZIF-8: A combined experimental and molecular simulation study*. Chemical Engineering Science, 2011. **66**(23): p. 6297-6305.
46. Fairen-Jimenez, D., et al., *Opening the gate: framework flexibility in ZIF-8 explored by experiments and simulations*. Journal of the American Chemical Society, 2011. **133**(23): p. 8900-8902.
47. Bux, H., et al., *Zeolitic imidazolate framework membrane with molecular sieving properties by microwave-assisted solvothermal synthesis*. Journal of the American Chemical Society, 2009. **131**(44): p. 16000-16001.
48. Bae, T.H., et al., *A high - performance gas - separation membrane containing submicrometer - sized metal-organic framework crystals*. Angewandte Chemie International Edition, 2010. **49**(51): p. 9863-9866.
49. Hara, N., et al., *Diffusive separation of propylene/propane with ZIF-8 membranes*. Journal of Membrane Science, 2014. **450**: p. 215-223.
50. Cravillon, J., et al., *Rapid room-temperature synthesis and characterization of nanocrystals of a prototypical zeolitic imidazolate framework*. Chemistry of Materials, 2009. **21**(8): p. 1410-1412.
51. Zhang, C. and W.J. Koros, *Zeolitic imidazolate framework-enabled membranes: challenges and opportunities*. The Journal of Physical Chemistry letters, 2015. **6**(19): p. 3841-3849.
52. McCarthy, M.C., et al., *Synthesis of zeolitic imidazolate framework films and membranes with controlled microstructures*. Langmuir, 2010. **26**(18): p. 14636-14641.
53. Li, K., et al., *Zeolitic imidazolate frameworks for kinetic separation of propane and propene*. Journal of the American Chemical Society, 2009. **131**(30): p. 10368-10369.
54. Ramu, G., M. Lee, and H.-K. Jeong, *Effects of zinc salts on the microstructure and performance of zeolitic-imidazolate framework ZIF-8 membranes for propylene/propane separation*. Microporous and Mesoporous Materials, 2018. **259**: p. 155-162.
55. Kwon, H.T. and H.-K. Jeong, *Improving propylene/propane separation performance of Zeolitic-Imidazolate framework ZIF-8 Membranes*. Chemical Engineering Science, 2015. **124**: p. 20-26.

56. Lee, M.J., H.T. Kwon, and H.-K. Jeong, *Defect-dependent stability of highly propylene-selective zeolitic-imidazolate framework ZIF-8 membranes*. Journal of Membrane Science, 2017. **529**: p. 105-113.
57. Huang, A., et al., *Bicontinuous zeolitic imidazolate framework ZIF-8@ GO membrane with enhanced hydrogen selectivity*. Journal of the American Chemical Society, 2014. **136**(42): p. 14686-14689.
58. Li, Y.S., et al., *Controllable synthesis of metal-organic frameworks: From MOF nanorods to oriented MOF membranes*. Advanced Materials, 2010. **22**(30): p. 3322-3326.
59. Li, Y.S., et al., *Molecular sieve membrane: supported metal-organic framework with high hydrogen selectivity*. Angewandte Chemie International Edition, 2010. **49**(3): p. 548-551.
60. Shah, M., et al., *One step in situ synthesis of supported zeolitic imidazolate framework ZIF-8 membranes: Role of sodium formate*. Microporous and Mesoporous Materials, 2013. **165**: p. 63-69.
61. Li, L., et al., *Infiltration of precursors into a porous alumina support for ZIF-8 membrane synthesis*. Microporous and Mesoporous Materials, 2013. **168**: p. 15-18.
62. Kwon, H.T., et al., *Defect-induced ripening of zeolitic-imidazolate framework ZIF-8 and its implication to vapor-phase membrane synthesis*. Chemical Communications, 2016. **52**(78): p. 11669-11672.
63. Hara, N., et al., *Zif-8 membranes prepared at miscible and immiscible liquid-liquid interfaces*. Microporous and Mesoporous Materials, 2015. **206**: p. 75-80.
64. Tanaka, S., et al., *Grain size control of ZIF-8 membranes by seeding-free aqueous synthesis and their performances in propylene/propane separation*. Journal of Membrane Science, 2017. **544**: p. 306-311.
65. Wang, N., et al., *Ceramic tubular MOF hybrid membrane fabricated through in situ layer - by - layer self - assembly for nanofiltration*. AIChE Journal, 2016. **62**(2): p. 538-546.
66. Xie, Z., et al., *Deposition of chemically modified  $\alpha$ -Al<sub>2</sub>O<sub>3</sub> particles for high performance ZIF-8 membrane on a macroporous tube*. Chemical Communications, 2012. **48**(48): p. 5977-5979.

67. Zhang, X., et al., *A simple and scalable method for preparing low-defect ZIF-8 tubular membranes*. Journal of Materials Chemistry A, 2013. **1**(36): p. 10635-10638.
68. Zhang, X., et al., *New membrane architecture with high performance: ZIF-8 membrane supported on vertically aligned ZnO nanorods for gas permeation and separation*. Chemistry of Materials, 2014. **26**(5): p. 1975-1981.
69. Sun, Y., et al., *Self-modified fabrication of inner skin ZIF-8 tubular membranes by a counter diffusion assisted secondary growth method*. RSC Advances, 2014. **4**(62): p. 33007-33012.
70. Wang, X., et al., *Formation of continuous and highly permeable ZIF-8 membranes on porous alumina and zinc oxide hollow fibers*. Chemical Communications, 2016. **52**(92): p. 13448-13451.
71. Xu, G., et al., *Preparation of ZIF-8 membranes supported on ceramic hollow fibers from a concentrated synthesis gel*. Journal of Membrane Science, 2011. **385**: p. 187-193.
72. Brown, A.J., et al., *Interfacial microfluidic processing of metal-organic framework hollow fiber membranes*. Science, 2014. **345**(6192): p. 72-75.
73. Eum, K., et al., *Fluidic Processing of High - Performance ZIF - 8 Membranes on Polymeric Hollow Fibers: Mechanistic Insights and Microstructure Control*. Advanced Functional Materials, 2016. **26**(28): p. 5011-5018.
74. Eum, K., et al., *ZIF-8 membranes via interfacial microfluidic processing in polymeric hollow fibers: efficient propylene separation at elevated pressures*. ACS Applied Materials & Interfaces, 2016. **8**(38): p. 25337-25342.
75. Brown, A.J., et al., *Continuous polycrystalline zeolitic imidazolate framework - 90 membranes on polymeric hollow fibers*. Angewandte Chemie International Edition, 2012. **51**(42): p. 10615-10618.
76. Lee, M.J., et al., *Ultrathin zeolitic-imidazolate framework ZIF-8 membranes on polymeric hollow fibers for propylene/propane separation*. Journal of Membrane Science, 2018. **559**: p. 28-34.
77. Hou, J., et al., *Formation of ultrathin, continuous metal-organic framework membranes on flexible polymer substrates*. Angewandte Chemie International Edition, 2016. **55**(12): p. 3947-3951.

78. Li, W., et al., *Ultrathin metal–organic framework membrane production by gel–vapour deposition*. Nature Communications, 2017. **8**(1): p. 406.
79. Tsapatsis, M., *Toward high-throughput zeolite membranes*. Science, 2011. **334**(6057): p. 767-768.
80. Jeon, M.Y., et al., *Ultra-selective high-flux membranes from directly synthesized zeolite nanosheets*. Nature, 2017. **543**(7647): p. 690.
81. Liquids, H.G., *Recent Market Trends and Issues*. Washington, DC: US Energy Information Administration, 2014.
82. 米镇涛, 张香文, 王莅, *化学工艺学*. 北京: 化学工业出版社, 2006.
83. Hocking, M.B., *Handbook of chemical technology and pollution control*. 2016: Elsevier.
84. Kwon, H.T. and H.-K. Jeong, *In situ synthesis of thin zeolitic–imidazolate framework ZIF-8 membranes exhibiting exceptionally high propylene/propane separation*. Journal of the American Chemical Society, 2013. **135**(29): p. 10763-10768.
85. Chokbunpiam, T., et al., *Gate opening effect for carbon dioxide in ZIF-8 by molecular dynamics–Confirmed, but at high CO<sub>2</sub> pressure*. Chemical Physics Letters, 2016. **648**: p. 178-181.
86. Safarik, D.J. and R.B. Eldridge, *Olefin/paraffin separations by reactive absorption: a review*. Industrial & Engineering Chemistry Research, 1998. **37**(7): p. 2571-2581.
87. Schneemann, A., et al., *Flexible metal–organic frameworks*. Chemical Society Reviews, 2014. **43**(16): p. 6062-6096.
88. Fairen-Jimenez, D., et al., *Flexibility and swing effect on the adsorption of energy-related gases on ZIF-8: combined experimental and simulation study*. Dalton Transactions, 2012. **41**(35): p. 10752-10762.
89. Zheng, B., et al., *Force field for molecular dynamics computations in flexible ZIF-8 framework*. The Journal of Physical Chemistry C, 2012. **116**(1): p. 933-938.

90. Zheng, B., et al., *Molecular dynamics simulations on gate opening in ZIF-8: identification of factors for ethane and propane separation*. Langmuir, 2013. **29**(28): p. 8865-8872.
91. Haldoupis, E., et al., *Quantifying Large Effects of Framework Flexibility on Diffusion in MOFs: CH<sub>4</sub> and CO<sub>2</sub> in ZIF - 8*. ChemPhysChem, 2012. **13**(15): p. 3449-3452.
92. Zhang, C., et al., *High performance ZIF-8/6FDA-DAM mixed matrix membrane for propylene/propane separations*. Journal of Membrane Science, 2012. **389**: p. 34-42.
93. Breck, D.W., *Zeolite Molecular Sieves*, John Wiley & Sons, New York. 1974.
94. Gücüyener, C., et al., *Ethane/ethene separation turned on its head: selective ethane adsorption on the metal-organic Framework ZIF-7 through a gate-opening mechanism*. Journal of the American Chemical Society, 2010. **132**(50): p. 17704-17706.
95. Aguado, S., et al., *Guest-induced gate-opening of a zeolite imidazolate framework*. New Journal of Chemistry, 2011. **35**(3): p. 546-550.
96. Kwon, H.T., et al., *Heteroepitaxially grown zeolitic imidazolate framework membranes with unprecedented propylene/propane separation performances*. Journal of the American Chemical Society, 2015. **137**(38): p. 12304-12311.
97. Shah, M.N., et al., *An unconventional rapid synthesis of high performance metal-organic framework membranes*. Langmuir, 2013. **29**(25): p. 7896-7902.
98. Huang, A., et al., *Molecular - sieve membrane with hydrogen permselectivity: ZIF - 22 in LTA topology prepared with 3 - aminopropyltriethoxysilane as covalent linker*. Angewandte Chemie International Edition, 2010. **49**(29): p. 4958-4961.
99. Huang, A., et al., *Organosilica - Functionalized Zeolitic Imidazolate Framework ZIF - 90 Membrane with High Gas - Separation Performance*. Angewandte Chemie International Edition, 2012. **51**(42): p. 10551-10555.
100. Liu, D., et al., *Gas transport properties and propylene/propane separation characteristics of ZIF-8 membranes*. Journal of Membrane Science, 2014. **451**: p. 85-93.

101. Aguado, S., J. Canivet, and D. Farrusseng, *Facile shaping of an imidazolate-based MOF on ceramic beads for adsorption and catalytic applications*. Chemical Communications, 2010. **46**(42): p. 7999-8001.
102. Gadipelli, S., et al., *A thermally derived and optimized structure from ZIF-8 with giant enhancement in CO<sub>2</sub> uptake*. Energy & Environmental Science, 2014. **7**(7): p. 2232-2238.
103. Zhang, C. and W.J. Koros, *Tailoring the transport properties of zeolitic imidazolate frameworks by post-synthetic thermal modification*. ACS Applied Materials & Interfaces, 2015. **7**(42): p. 23407-23411.
104. Thompson, J.A., et al., *Hybrid zeolitic imidazolate frameworks: controlling framework porosity and functionality by mixed-linker synthesis*. Chemistry of Materials, 2012. **24**(10): p. 1930-1936.
105. Liao, Y.-T., et al., *Synthesis of mixed-ligand zeolitic imidazolate framework (ZIF-8-90) for CO<sub>2</sub> adsorption*. Journal of Inorganic and Organometallic Polymers and Materials, 2015. **25**(2): p. 251-258.
106. Eum, K., et al., *Highly tunable molecular sieving and adsorption properties of mixed-linker zeolitic imidazolate frameworks*. Journal of the American Chemical Society, 2015. **137**(12): p. 4191-4197.
107. Hillman, F., et al., *Rapid microwave-assisted synthesis of hybrid zeolitic-imidazolate frameworks with mixed metals and mixed linkers*. Journal of Materials Chemistry A, 2017. **5**(13): p. 6090-6099.
108. Botas, J.A., et al., *Cobalt doping of the MOF-5 framework and its effect on gas-adsorption properties*. Langmuir, 2010. **26**(8): p. 5300-5303.
109. Caskey, S.R., A.G. Wong-Foy, and A.J. Matzger, *Dramatic tuning of carbon dioxide uptake via metal substitution in a coordination polymer with cylindrical pores*. Journal of the American Chemical Society, 2008. **130**(33): p. 10870-10871.
110. Kaur, G., et al., *Room-temperature synthesis of bimetallic Co-Zn based zeolitic imidazolate frameworks in water for enhanced CO<sub>2</sub> and H<sub>2</sub> uptakes*. Journal of Materials Chemistry A, 2016. **4**(39): p. 14932-14938.
111. Schejn, A., et al., *Cu<sup>2+</sup>-doped zeolitic imidazolate frameworks (ZIF-8): efficient and stable catalysts for cycloadditions and condensation reactions*. Catalysis Science & Technology, 2015. **5**(3): p. 1829-1839.

112. Wang, C., et al., *Zinc-substituted ZIF-67 nanocrystals and polycrystalline membranes for propylene/propane separation*. Chemical Communications, 2016. **52**(85): p. 12578-12581.
113. Zhu, X.-W., X.-P. Zhou, and D. Li, *Exceptionally water stable heterometallic gyroidal MOFs: tuning the porosity and hydrophobicity by doping metal ions*. Chemical Communications, 2016. **52**(39): p. 6513-6516.
114. Burrows, A.D., *Mixed-component metal–organic frameworks (MC-MOFs): enhancing functionality through solid solution formation and surface modifications*. CrystEngComm, 2011. **13**(11): p. 3623-3642.
115. Dhakshinamoorthy, A., A.M. Asiri, and H. Garcia, *Mixed-metal or mixed-linker metal organic frameworks as heterogeneous catalysts*. Catalysis Science & Technology, 2016. **6**(14): p. 5238-5261.
116. Qin, J.-S., et al., *Mixed-linker strategy for the construction of multifunctional metal–organic frameworks*. Journal of Materials Chemistry A, 2017. **5**(9): p. 4280-4291.
117. Gross, A.F., E. Sherman, and J.J. Vajo, *Aqueous room temperature synthesis of cobalt and zinc sodalite zeolitic imidizolate frameworks*. Dalton Transactions, 2012. **41**(18): p. 5458-5460.
118. Qin, J.-S., et al., *N-rich zeolite-like metal–organic framework with sodalite topology: high CO<sub>2</sub> uptake, selective gas adsorption and efficient drug delivery*. Chemical Science, 2012. **3**(6): p. 2114-2118.
119. Horike, S., et al., *Synthesis of magnesium ZIF-8 from Mg (BH 4) 2*. Dalton Transactions, 2015. **44**(34): p. 15107-15110.
120. He, M., et al., *Facile synthesis of zeolitic imidazolate framework-8 from a concentrated aqueous solution*. Microporous and Mesoporous Materials, 2014. **184**: p. 55-60.
121. Panda, T., et al., *Mechanical Alloying of Metal–Organic Frameworks*. Angewandte Chemie, 2017. **129**(9): p. 2453-2457.
122. Zhang, C., et al., *Crystal-size-dependent structural transitions in nanoporous crystals: adsorption-induced transitions in ZIF-8*. The Journal of Physical Chemistry C, 2014. **118**(35): p. 20727-20733.



123. Tang, J., et al., *Thermal conversion of core–shell metal–organic frameworks: a new method for selectively functionalized nanoporous hybrid carbon*. Journal of the American Chemical Society, 2015. **137**(4): p. 1572-1580.
124. Minor, W., et al., *HKL-3000: the integration of data reduction and structure solution—from diffraction images to an initial model in minutes*. Acta Crystallographica Section D: Biological Crystallography, 2006. **62**(8): p. 859-866.
125. XPREP, V., 6.12, *Program for Automatic Space Group Determination*. Bruker AXS Inc., Madison, WI, 2001.
126. Sheldrick, G.M., C. Acta Crystallographica Section A: Foundations of Crystallography, 2008. **64**(1): p. 112-122.
127. Schejn, A., et al., *Controlling ZIF-8 nano- and microcrystal formation and reactivity through zinc salt variations*. CrystEngComm, 2014. **16**(21): p. 4493-4500.
128. Nordin, N.A.H.M., et al., *The impact of ZIF-8 particle size and heat treatment on CO<sub>2</sub>/CH<sub>4</sub> separation using asymmetric mixed matrix membrane*. RSC Advances, 2014. **4**(94): p. 52530-52541.
129. Constable, E., *Zinc and cadmium*. Coordination Chemistry Reviews, 1984. **58**: p. 1-51.
130. Birger, J.J., *Cadmium-imidazole complex formation in aqueous solutions, stability constants, changes in standard free energies, enthalpies, entropies, and heat capacities accompanying the complex formation at 5, 15, 25 and 40 C*. Acta Chemica Scandinavica Series A-Physical and Inorganic Chemistry 1975. **29**(2): p. 250-254.
131. Li, Y., et al., *Synthesis of ZIF-8 and ZIF-67 using mixed-base and their dye adsorption*. Microporous and Mesoporous Materials, 2016. **234**: p. 287-292.
132. Bissett, H., J. Zah, and H. Krieg, *Manufacture and optimization of tubular ceramic membrane supports*. Powder Technology, 2008. **181**(1): p. 57-66.
133. Biesheuvel, P.M., et al., *Graded membrane supports produced by centrifugal casting of a slightly polydisperse suspension*. Chemical Engineering Science, 2001. **56**(11): p. 3517-3525.

134. Pina, M., et al., *A semi-continuous method for the synthesis of NaA zeolite membranes on tubular supports*. Journal of Membrane Science, 2004. **244**(1-2): p. 141-150.
135. Baker, R.W. and B.T. Low, *Gas separation membrane materials: a perspective*. Macromolecules, 2014. **47**(20): p. 6999-7013.
136. Harlacher, T. and M. Wessling, *Gas-gas separation by membranes*, in *Progress in Filtration and Separation*. 2015, Elsevier. p. 557-584.
137. Hara, N., et al., *Effect of temperature on synthesis of zif-8 membranes for propylene/propane separation by counter diffusion method*. J. Jpn. Pet. Inst, 2015. **58**: p. 237-244.
138. Cacho-Bailo, F., et al., *Metal-organic framework membranes on the inner-side of a polymeric hollow fiber by microfluidic synthesis*. Journal of Membrane Science, 2015. **476**: p. 277-285.
139. Marti, A.M., et al., *Continuous flow processing of ZIF-8 membranes on polymeric porous hollow fiber supports for CO<sub>2</sub> capture*. ACS Applied Materials & Interfaces, 2017. **9**(7): p. 5678-5682.
140. Biswal, B.P., et al., *Selective interfacial synthesis of metal-organic frameworks on a polybenzimidazole hollow fiber membrane for gas separation*. Nanoscale, 2015. **7**(16): p. 7291-7298.
141. Pan, Y., B. Wang, and Z. Lai, *Synthesis of ceramic hollow fiber supported zeolitic imidazolate framework-8 (ZIF-8) membranes with high hydrogen permeability*. Journal of Membrane Science, 2012. **421**: p. 292-298.
142. Zhou, J., et al., *Elaboration and characterization of tubular macroporous ceramic support for membranes from kaolin and dolomite*. Journal of Porous Materials, 2010. **17**(1): p. 1.
143. Huang, A., W. Dou, and J.r. Caro, *Steam-stable zeolitic imidazolate framework ZIF-90 membrane with hydrogen selectivity through covalent functionalization*. Journal of the American Chemical Society, 2010. **132**(44): p. 15562-15564.
144. Venna, S.R. and M.A. Carreon, *Highly permeable zeolite imidazolate framework-8 membranes for CO<sub>2</sub>/CH<sub>4</sub> separation*. Journal of the American Chemical Society, 2009. **132**(1): p. 76-78.

145. Tanaka, S., et al., *Seeding-free aqueous synthesis of zeolitic imidazolate framework-8 membranes: How to trigger preferential heterogeneous nucleation and membrane growth in aqueous rapid reaction solution*. Journal of Membrane Science, 2014. **472**: p. 29-38.
146. Colling, C.W., G.A. Huff Jr, and J.V. Bartels, *Processes using solid perm-selective membranes in multiple groups for simultaneous recovery of specified products from a fluid mixture*. 2004, US Patent 6,830,691.
147. Soukup, K., P. Schneider, and O. Šolcová, *Comparison of Wicke–Kallenbach and Graham's diffusion cells for obtaining transport characteristics of porous solids*. Chemical Engineering Science, 2008. **63**(4): p. 1003-1011.
148. Jarvelin, H. and J.R. Fair, *Adsorptive separation of propylene-propane mixtures*. Industrial & Engineering Chemistry Research, 1993. **32**(10): p. 2201-2207.
149. Böhme, U., et al., *Ethene/ethane and propene/propane separation via the olefin and paraffin selective metal–organic framework adsorbents CPO-27 and ZIF-8*. Langmuir, 2013. **29**(27): p. 8592-8600.
150. Krokidas, P., M. Castier, and I.G. Economou, *Computational study of ZIF-8 and ZIF-67 performance for separation of gas mixtures*. The Journal of Physical Chemistry C, 2017. **121**(33): p. 17999-18011.
151. Krokidas, P., et al., *ZIF-67 framework: a promising new candidate for propylene/propane separation. Experimental data and molecular simulations*. The Journal of Physical Chemistry C, 2016. **120**(15): p. 8116-8124.
152. Ernst, S., *Advances in nanoporous materials*. Vol. 1. 2009: Elsevier.
153. Zhang, S., et al., *Nanoporous film-mediated growth of ultrathin and continuous metal–organic framework membranes for high-performance hydrogen separation*. Journal of Materials Chemistry A, 2017. **5**(5): p. 1962-1966.
154. He, G., D.J. Babu, and K.V. Agrawal, *Electrophoretic Crystallization of Ultrathin High-performance Metal-organic Framework Membranes*. Journal of Visualized Experiments, 2018(138): p. e58301.
155. He, G., et al., *Electrophoretic Nuclei Assembly for Crystallization of High - Performance Membranes on Unmodified Supports*. Advanced Functional Materials, 2018. **28**(20): p. 1707427.

156. Hu, Y., et al., *Zeolitic imidazolate framework/graphene oxide hybrid nanosheets as seeds for the growth of ultrathin molecular sieving membranes*. *Angewandte Chemie International Edition*, 2016. **55**(6): p. 2048-2052.
157. Zhou, S., et al., *Paralyzed membrane: Current-driven synthesis of a metal-organic framework with sharpened propene/propane separation*. *Science Advances*, 2018. **4**(10): p. eaau1393.
158. Lee, M.J., H.T. Kwon, and H.K. Jeong, *High - Flux Zeolitic Imidazolate Framework Membranes for Propylene/Propane Separation by Postsynthetic Linker Exchange*. *Angewandte Chemie*, 2018. **130**(1): p. 162-167.
159. Yang, L. and H. Lu, *Microwave - assisted ionothermal synthesis and characterization of zeolitic imidazolate framework - 8*. *Chinese Journal of Chemistry*, 2012. **30**(5): p. 1040-1044.
160. Zhang, W., et al., *Spontaneous Weaving of Graphitic Carbon Networks Synthesized by Pyrolysis of ZIF - 67 Crystals*. *Angewandte Chemie International Edition*, 2017. **56**(29): p. 8435-8440.
161. Sun, J., et al., *Facile synthesis of Cd-substituted zeolitic-imidazolate framework Cd-ZIF-8 and mixed-metal CdZn-ZIF-8*. *Microporous and Mesoporous Materials*, 2018. **264**: p. 35-42.
162. Nordin, N., et al., *Aqueous room temperature synthesis of zeolitic imidazole framework 8 (ZIF-8) with various concentrations of triethylamine*. *RSC Advances*, 2014. **4**(63): p. 33292-33300.
163. Xin, Z., et al., *Nanopolyhedrons and mesoporous supra-structures of Zeolitic Imidazolate framework with high adsorption performance*. *Microporous and Mesoporous Materials*, 2013. **169**: p. 218-221.
164. Liguori, P.F., et al., *Synthesis and gas sorption behaviour of ZIF-90 with large pore volume*. *New Journal of Chemistry*, 2017. **41**(22): p. 13235-13239.
165. Wang, S., et al., *Modulated synthesis of monodisperse MOF-5 crystals with tunable sizes and shapes*. *Inorganic Chemistry Communications*, 2018. **93**: p. 56-60.
166. Yang, J.-M., et al., *Effect of additives on morphology and size and gas adsorption of SUMOF-3 microcrystals*. *Microporous and Mesoporous Materials*, 2016. **222**: p. 27-32.

167. Wu, X., et al., *Nanoporous ZIF-67 embedded polymers of intrinsic microporosity membranes with enhanced gas separation performance*. Journal of Membrane Science, 2018. **548**: p. 309-318.
168. Nian, P., et al., *ZnO nanorod-induced heteroepitaxial growth of SOD type Co-based zeolitic imidazolate framework membranes for H<sub>2</sub> separation*. ACS Applied Materials & Interfaces, 2018. **10**(4): p. 4151-4160.
169. Knebel, A., et al., *Hierarchical Nanostructures of Metal - Organic Frameworks Applied in Gas Separating ZIF - 8 - on - ZIF - 67 Membranes*. Chemistry - A European Journal, 2018. **24**(22): p. 5728-5733.
170. Zhou, K., et al., *Characterization and properties of Zn/Co zeolitic imidazolate frameworks vs. ZIF-8 and ZIF-67*. Journal of Materials Chemistry A, 2017. **5**(3): p. 952-957.
171. An, H., et al., *A new superior competitor for exceptional propylene/propane separations: ZIF-67 containing mixed matrix membranes*. Journal of Membrane Science, 2017. **526**: p. 367-376.
172. Marappa, S. and P.V. Kamath, *Structure of the carbonate-intercalated Layered Double Hydroxides: A reappraisal*. Industrial & Engineering Chemistry Research, 2015. **54**(44): p. 11075-11079.
173. Kolokolov, D.I., A.G. Stepanov, and H. Jovic, *Mobility of the 2-methylimidazolate linkers in ZIF-8 probed by 2H NMR: saloon doors for the guests*. The Journal of Physical Chemistry C, 2015. **119**(49): p. 27512-27520.
174. Yang, Y., et al., *Development of zeolitic imidazolate framework-67 functionalized Co-Al LDH for CO<sub>2</sub> adsorption*. Colloids and Surfaces A: Physicochemical and Engineering Aspects, 2018. **552**: p. 16-23.
175. Kubo, M., T. Saito, and M. Shimada, *Evaluation of the parameters utilized for the aerosol-assisted synthesis of HKUST-1*. Microporous and Mesoporous Materials, 2017. **245**: p. 126-132.
176. Gimeno-Fabra, M., et al., *Instant MOFs: continuous synthesis of metal-organic frameworks by rapid solvent mixing*. Chemical Communications, 2012. **48**(86): p. 10642-10644.
177. Faustini, M., et al., *Microfluidic approach toward continuous and ultrafast synthesis of metal-organic framework crystals and hetero structures in*

- confined microdroplets*. Journal of the American Chemical Society, 2013. **135**(39): p. 14619-14626.
178. Taddei, M., et al., *Continuous - Flow Microwave Synthesis of Metal - Organic Frameworks: A Highly Efficient Method for Large - Scale Production*. Chemistry - A European Journal, 2016. **22**(10): p. 3245-3249.
179. Jambovane, S.R., et al., *Continuous, One-pot Synthesis and Post-Synthetic Modification of NanoMOFs Using Droplet Nanoreactors*. Scientific reports, 2016. **6**: p. 36657.
180. Parulkar, A. and N.A. Brunelli, *High-yield synthesis of ZIF-8 nanoparticles using stoichiometric reactants in a jet-mixing reactor*. Industrial & Engineering Chemistry Research, 2017. **56**(37): p. 10384-10392.
181. Choi, H.-S., et al., *Scalable continuous solvo-jet process for ZIF-8 nanoparticles*. Chemical Engineering Journal, 2015. **266**: p. 56-63.
182. Walton, D. and C. Mumford, *The morphology of spray-dried particles: the effect of process variables upon the morphology of spray-dried particles*. Chemical Engineering Research and Design, 1999. **77**(5): p. 442-460.
183. Wang, Z., et al., *Lanthanide - Organic Framework Nanothermometers Prepared by Spray - Drying*. Advanced Functional Materials, 2015. **25**(19): p. 2824-2830.
184. Carné - Sánchez, A., et al., *Protecting Metal - Organic Framework Crystals from Hydrolytic Degradation by Spray - Dry Encapsulating Them into Polystyrene Microspheres*. Advanced Materials, 2015. **27**(5): p. 869-873.
185. Garzón-Tovar, L., et al., *Spray drying for making covalent chemistry: postsynthetic modification of metal-organic frameworks*. Journal of the American Chemical Society, 2017. **139**(2): p. 897-903.
186. Garzón-Tovar, L., et al., *Spray drying for making covalent chemistry II: synthesis of covalent-organic framework superstructures and related composites*. Chemical Communications, 2017. **53**(82): p. 11372-11375.
187. Gholampour, N., et al., *Simultaneous creation of metal nanoparticles in metal organic frameworks via spray drying technique*. Chemical Engineering Journal, 2017. **322**: p. 702-709.

188. Carné-Sánchez, A., et al., *A spray-drying strategy for synthesis of nanoscale metal–organic frameworks and their assembly into hollow superstructures*. *Nature Chemistry*, 2013. **5**(3): p. 203.
189. Chui, S.S.-Y., et al., *A chemically functionalizable nanoporous material [Cu<sub>3</sub>(TMA) 2 (H<sub>2</sub>O) 3] n*. *Science*, 1999. **283**(5405): p. 1148-1150.
190. Marquez, A.G., et al., *Green scalable aerosol synthesis of porous metal–organic frameworks*. *Chemical Communications*, 2013. **49**(37): p. 3848-3850.
191. Garzón-Tovar, L., et al., *A spray-drying continuous-flow method for simultaneous synthesis and shaping of microspherical high nuclearity MOF beads*. *Reaction Chemistry & Engineering*, 2016. **1**(5): p. 533-539.
192. Shekhah, O., et al., *Growth mechanism of metal – organic frameworks: insights into the nucleation by employing a step - by - step route*. *Angewandte Chemie International Edition*, 2009. **48**(27): p. 5038-5041.
193. Okuyama, K. and I.W. Lenggoro, *Preparation of nanoparticles via spray route*. *Chemical Engineering Science*, 2003. **58**(3-6): p. 537-547.
194. Gutmann, V., *Solvent effects on the reactivities of organometallic compounds*. *Coordination Chemistry Reviews*, 1976. **18**(2): p. 225-255.
195. Persson, I., *Solvation and complex formation in strongly solvating solvents*. *Pure and Applied Chemistry*, 1986. **58**(8): p. 1153-1161.
196. Cotton, F. and R. Francis, *Sulfoxides as ligands. I. A preliminary survey of methyl sulfoxide complexes*. *Journal of the American Chemical Society*, 1960. **82**(12): p. 2986-2991.
197. Berney, C.V. and J.H. Weber, *Complexes of sulfoxides. II. Metal-oxygen stretching vibrations in complexes of dimethyl sulfoxide and dimethyl sulfoxide-d<sub>6</sub> and the point group of the cation*. *Inorganic Chemistry*, 1968. **7**(2): p. 283-287.
198. Lefebvre, J., R.J. Batchelor, and D.B. Leznoff, *Cu [Au (CN) 2] 2 (DMSO) 2: Golden polymorphs that exhibit vapochromic behavior*. *Journal of the American Chemical Society*, 2004. **126**(49): p. 16117-16125.
199. Vakulka, A. and E. Goreshnik, *Unknown cis-[(DMSO) 2ClCuII (μ-Cl) 2CuIICl (DMSO) 2] isomer obtained via new [Cu<sub>4</sub>Cl<sub>8</sub> (DMSO) 8 (hmta)] template complex*. *Journal of Coordination Chemistry*, 2017. **70**(3): p. 556-563.

200. Moniz, W., C. Poranski Jr, and D. Venezky, *Dimethyl Sulfoxide Complexes of Chromium (III), Manganese (II), Iron (III), Nickel (II), and Copper (II) Nitrates and Magnesium and Nickel (II) Perchlorates. PART 1. Preparation and Nuclear Magnetic Resonance and Infrared Studies*. 1967, Naval Research Lab Washington DC.
201. Chowdhury, P., et al., *Comparison of adsorption isotherms on Cu-BTC metal organic frameworks synthesized from different routes*. *Microporous and Mesoporous Materials*, 2009. **117**(1-2): p. 406-413.
202. Schlichte, K., T. Kratzke, and S. Kaskel, *Improved synthesis, thermal stability and catalytic properties of the metal-organic framework compound Cu<sub>3</sub> (BTC) 2*. *Microporous and Mesoporous Materials*, 2004. **73**(1-2): p. 81-88.
203. Sachse, A., et al., *In situ synthesis of Cu-BTC (HKUST-1) in macro-/mesoporous silica monoliths for continuous flow catalysis*. *Chemical Communications*, 2012. **48**(39): p. 4749-4751.
204. Tarasevich, B., P. Rieke, and J. Liu, *Nucleation and growth of oriented ceramic films onto organic interfaces*. *Chemistry of Materials*, 1996. **8**(1): p. 292-300.
205. Valizadeh, B., et al., *Porous Metal - Organic Framework@ Polymer Beads for Iodine Capture and Recovery Using a Gas - Sparged Column*. *Advanced Functional Materials*, 2018. **28**(30): p. 1801596.
206. Zheng, G., et al., *Shape control in ZIF-8 nanocrystals and metal nanoparticles@ ZIF-8 heterostructures*. *Nanoscale*, 2017. **9**(43): p. 16645-16651.
207. Chen, R., et al., *A two-dimensional zeolitic imidazolate framework with a cushion-shaped cavity for CO<sub>2</sub> adsorption*. *Chemical Communications*, 2013. **49**(82): p. 9500-9502.
208. Venna, S.R., J.B. Jasinski, and M.A. Carreon, *Structural evolution of zeolitic imidazolate framework-8*. *Journal of the American Chemical Society*, 2010. **132**(51): p. 18030-18033.
209. Hamid, M.R.A. and H.-K. Jeong, *Recent advances on mixed-matrix membranes for gas separation: Opportunities and engineering challenges*. *Korean Journal of Chemical Engineering*, 2018. **35**(8): p. 1577-1600.